Analysis of pseudobrookite metal oxide semiconductor material with possible application for NO gas sensing

Goran Mišković
1228572

A thesis presented for the degree of
Doctor of Technical Sciences

Department of Applied Electronic Materials
Institute of Sensor and Actuator Systems
Technische Universität Wien

Mentors:
Ao.Univ.Prof. Dipl.-Ing. Dr.techn. Johann Nicolics
Prof. Dr. Obrad Aleksić
Prof. Dr. Maria Vesna Nikolić

August 2016, Vienna, Austria

Contents

Acknowledgment

First and foremost I want to thank my advisors Ao.Univ.Prof. Dipl.-Ing. Dr.techn. Johann Nicolics for all his support, patience and for believing in me, to Prof. Dr. Obrad Aleksić for support, passing his enthusiasm for research on me and preparation of wonderful materials and to Prof. Dr. Maria Vesna Nikolić her unconditional support, assistance with the thesis writing and for reviewing the thesis in detail.

I would like to thank to Dr. Goran Radosavljević for giving me opportunity to pursue my Ph.D thesis, for funding my Ph.D work and for his support to improve my personal qualities, travel and extend my knowledge.

Also, I would like to thank to Dr. Pero Krivić for his support and assistance with the simulations, for reviewing the thesis and for his boring motivation talks.

I would like to thank my co-workers:
-Ing. Heinz Homolka for his assistance and support with the establishment of gas testing set-up;
-Dr. Paul Fulmek for providing me impeccable software and for making the translations;
-Dr. Johaness Schalko for lending me the helium leakage tester;
-Thomas Pareihs for making parts for gas testing set-up;
-Thomas Zottl for maintaining the PCs;
-Ronald Glatz making excellent photos, for maintaining the PC and for supporting me on the technical aspects;
-Dipl. Ing. Michael Unger for supporting me, nice talks and great ideas;
-Dipl. Ing. Manuela Franz for supporting and motivating me to write the thesis;
-Dr. Peter Haumer for nice talks and for motivating me to conclude the thesis;
-Dr. Miloljub Lukovic for sample preparations;
-Dr. Nelu Blaž for Impedance measurements;
-Martina Bittner and Sabine Fuchs for helping me with the administrative work, both business and private, for solving my endless traveling problems and for having patience with me.

I am grateful and thankful for being a part of Senseiver project and for the wonderful people which I met. To Saša, Branislava, Katarina, Beata, Monika, Olga, Nenad, Mitar, Aleksandar, Milenko, Srdjan, Akhil, Libu, Jose, Anatoli, Bilal and Iman. As well as to Prof. Stojanović, Prof. Dorota, Krzistof, Prof Jan, Prof Chiobanu, Djordje, Prof. Tavares and Prof Mendosa, thank you for the nice company, great adventures an for the amazing best 3 years.

I would also like to thank to my friends for their endless support and motivation for all this years. To Brka, Melita, Nikola (Bruder), Uroš, Žilić, Žare, Sanja,

Isidora, Dražen, Pero, Weilguni, Dana, Belal, Tanja, Tobi, Linda, Ljubica, Sladja, Ležajić thank you :)

Especially I would like to express my sincere gratitude to Zorana Pavlov (aka Zox) for her support, understanding and company in the previous years.

Last but not the least, I would like to thank my family for all their love, support and encouragement. Especially to my mom, who has sacrificed everything for me, I would like to thank her for the unconditional love, support and for believing in me.

Goran Mišković

August 2016, Vienna, Austria

Abbreviations

- PM_{10} - Particles with an average diameter smaller than 10 μm
- $PM_{2.5}$ - Particles with an average diameter smaller than 2.5 μm
- VOC - Volatile organic compounds
- 3D - Three-dimensional
- A - Anatase
- BAW - Bulk acoustic wave
- BSE - Back scattering
- CFS - Chlorofluorocarbons
- CNTs - Carbon nanotubes
- COPD - Chronic obstructive pulmonary disease
- CPE - Constant phase element
- DC - Direct current
- DIAL - Differential Absorption LIDAR
- DNA - Deoxyribonucleic acid
- DOAS - Differential Optical Absorption Spectroscopy
- EC - Energy of the conduction band
- EDS - Energy-dispersive X-ray Spectroscopy
- EF - Fermi level
- EIS - Electrochemical Impedance Spectroscopy
- EPR - Electron paramagnetic resonance
- EV - Energy of valence band

- FTIR - Fourier Transform Infrared Spectroscopy
- H - Hematite
- HFS - Hydrofluorocarbons
- ICAS - Intra-Cavity Absorption Spectrometry
- ID - Interdigitated
- IR - Infrared
- LIBS - Laser-Induced Breakdown Spectroscopy
- LIDAL - Raman Light Detection and Ranging
- LTCC - Low Temperature Co-Fired Ceramic
- MIPs - Molecular imprinted polymers
- MOS - Metal oxide semiconductor
- MWCNTs - Multi-walled carbon nanotubes
- NAAQS - National Ambient Air Quality Standards
- NTC -Negative temperature coefficient
- NTC - Negative temperature coefficient
- PA - Polyacetylene
- PAH - Polynuclear aromatic hydrocarbons
- PAni - Polyaniline
- PCB - Polychlorinated biphenyls
- PCDD/Fs - Polychlorinated dibenzo-*p*-dioxins and-furans
- PM - Monoclinic pseudobrookite
- PM - Particulate matter
- PO - Orthorhombic pseudobrookite
- POP - Persistent organic pollutants
- PPy - Polypyrrole
- PSB-1 - A nanopowder mixture of hematite and anatase in the molar ratio 1:1

- PSB-1.5 - A nanopowder mixture of hematite and anatase in the molar ratio 1:1.5
- PSB - Pseudobrookite
- PTh - Polythiophene
- QCM - Quartz Crystal Microbalance
- R - Rutile
- RC - Resistor–capacitor
- RNA - Ribonucleic acid
- SAW - Surface Acoustic Wave
- SEM - Scanning Electron Microscopy
- SPH - Small polaron hopping
- SWCNTs - Single-walled carbon nanotubes
- TDLAS - Tunable Diode Laser Absorption Spectroscopy
- TFT - Thin film transistors
- TPD - Temperature programmed desorption
- UFP - Ultra fine particles
- US EPA - United Sates Environment Protection Agency
- UV - Ultraviolet
- WHO - World Health Organization
- XRD - X-ray Powder Diffraction
- sd - standard deviation

Chemical Symbols

- Al_2O_3 - Alumina
- $BaTiO_3$ - Barium titanate
- C_2Cl_4 - Tetrachloroethylene
- C_6H_{14} - N-hexane
- C_6H_6 - Benzene
- C_7H_8 - Toluene
- C_8H_{10} - Xylene
- CH_2Cl_2 - Dichloromethane
- CH_2O - Formaldehyde
- CH_4 - Methane
- CO - Carbon monoxide
- Co_3O_4 - Cobalt(II,III) oxide
- CrO_2 - Chromium dioxide or chromium(IV) oxide
- CuO - Copper(II) oxide or cupric oxide
- Fe_2O_3 - Iron(III) oxide or ferric oxide
- Fe_2TiO_5 - Pseudobrookite
- FeO - Iron(II) oxide or ferrous oxide
- Fe^{3+} - Iron ions
- H_2 - Hydrogen
- In_2O_3 - Indium(III) oxide
- NH_3 - Ammonia

- NO_2 - Nitrogen monoxide
- NO_x - Nitrogen oxides
- NO – Nitrogen oxide
- Na_xWO_3 - Sodium tungsten oxides
- NiO - Nickel(II) oxide
- O_2 - Oxygen
- O_2^- - Singly ionized molecular chemisorbed oxygen specie
- O_3 - Ozone
- O^- - Singly ionized atomic chemisorbed oxygen specie
- O^{2-} - Doubly ionized atomic chemisorbed oxygen specie
- PdAg - Silver Palladium
- Pt - Platinum
- ReO_3 - Rhenium trioxide or rhenium oxide
- RuO_2 - Ruthenium(IV) oxide
- SO_2 - Sulfur dioxide
- SnO_2 - Tin oxide
- $SrTiO_3$ - Strontium titanate
- Ti_2O_3 - Titanium(III) oxide
- TiO_2 - Titanium oxide
- Ti^{4+} - Titanium ions
- V_2O_3 - Vanadium(III) oxide
- V_2O_5 - Vanadium(V) oxide
- WO_3 - Tungsten oxide
- ZnO - Zinc oxide
- ^{131}I - Iodine
- ^{137}Cs - Cesium
- ^{226}Ra - Radium

- ^{238}U and ^{235}U - Uranium
- ^{239}Pu - Plutonium
- ^{90}Sr - Strontium

Nomenclatures

- E_g - Band gap
- O_2^{gas} - Oxygen molecule in the ambient atmosphere
- O_{ads}^{-} - Adsorbed oxygen species
- e^- - Electron charge
- z_n - Neck diameter
- ω - Angular frequency
- ϕ - Barrier height
- θ - Bragg angle
- δ - Debye length
- Λ - Depleted surface region
- σ - Electrical conductivity
- ρ - Electrical resistivity (specific electrical resistance)
- τ - Grain boundary relaxation time
- β - Pure full width of the diffraction line at half of the maximum intensity
- λ - Wavelength
- ε_0 - Permittivity in vacuum
- τ_0 - Pre-exponential factor
- $\bigcirc_2$ - Anion vacancy
- μ_b - Bulk electron mobility
- ϵ_r - Relative permittivity
- A - Constant

- A_0 - Pre-exponential factor
- B - value - Material constant
- C_p - Capacitance in parallel
- D - Grain diameter
- E - Fitted parameter of the CPE element
- E_a - Activation energy for conduction
- E_{rp} - Activation energy for the relaxation process at grain boundaries
- G - Thermionic conductivity
- M - Sensor's response
- N_b - Bulk charge/carrier concentration
- N_d - Donor concentration
- N_s - Number of electrons (per area unit)
- R - Resistance
- R_C - Contact resistance
- R_{air} - Resistance of the sensor when exposed toward air
- R_{gas} - Resistance of the sensor when exposed toward gas
- R_p - Resistance in parallel
- S - An unoccupied chemisorption site for oxygen-surface oxygen vacancies
- T - Temperature
- V - Volume
- X - Reactance
- d - Diameter
- eV_s - Height of the potential barrier
- g - Fitted parameter of the CPE element
- $h\varphi$ - Absorbed photon energy
- k - Boltzmann constant
- l - Length of the finger

- m - Weight
- m - Width
- n - Number of fingers
- p - Length
- q - Electron charge
- s - Interdigitated electrode spacing
- s - Spacing
- t - Thickness
- w - Interdigitated electrode width

SI unit symbols

- Å - Angstrom ($10^{-10}m$)
- μ - Micro
- Ω - Ohm
- °C – degree Celsius
- G - Giga
- Hz - Hertz
- M - Mega
- Pa - Pascal
- S - Siemens
- V - Volt
- eV – Electron volt
- g - Gram
- k - Kilo
- m - Meter
- n - Nano
- s - Second

Summary

This thesis deals with the preparation and application of pseudobrookite (Fe_2TiO_5) metal oxide semiconductor (MOS) as gas sensor to monitor hazardous gases.

One of the major drawbacks of gas sensors based on the MOS materials is the relatively high working temperature above 250 °C. In order to achieve those high temperatures, heating elements have to be implemented, which lead to a high power consumption of the sensor. Additionally, this leads towards a more complex sensor design raising the production costs.

The goal of this thesis was to synthesize, analyze and characterize pseudobrookite (PSB) metal oxide gas sensitive material and to investigate its sensitivity to nitrogen oxide (NO) gas at temperatures below 300 °C.

In Chapter 1 a comprehensive overview of the most prominent air pollutants is given, together with the respective legal regulations.

Chapter 2 gives an overview of selected, representative gas sensing methods, focusing on MOS materials. Comprehensive analyses, including the sensing mechanism and influencing factors, are studied and presented.

Chapter 3 is concerned with the production and analysis of bulk and thick film PSB. The PSB material is prepared from a mixture of nanoparticles of hematite (Fe_2O_3) and anatase (TiO_2) in two different molar ratios.

To produce bulk PSB the powder is pressed into tablets and sintered at varying sintering temperatures. X-ray Powder Diffraction (XRD) analysis is used to evaluate the resulting material with respect to the formation of orthorhombic and monoclinic PSB and the transformation of the TiO_2 phases (anatase into rutile). Scanning Electron Microscopy (SEM) and Energy-dispersive X-ray Spectroscopy (EDS) of the bulk material show the effect of sintering parameters on grain size, porosity, and homogeneity.

Thick film pastes are composed from the nanopowder mixtures by adding butyl cellulose as organic vehicle and a small amount of lead boron silicone oxide glass frit. This paste is screen printed on alumina substrate and sintered in a hybrid conveyor furnace with different parameters. The resulting material is characterized using XRD, SEM, and EDS.

Impedance measurements on the produced samples are presented in Chapter 4. The temperature dependence of the resistance is used to estimate the band gap energies and the activation energies for the differently processed materials. Additionally a dependence on the DC–voltage was determined.

Finally the sensitivity of the resistance towards a NO gas concentration was examined. The results show a reasonable sensitivity of the PSB material at temperatures below 300 °C. A concentration of 5% NO diluted in synthetic air could be sensed at an operating temperature of 150 °C.

Zusammenfassung

Diese Arbeit befaßt sich mit den Einsatzmöglichkeiten von Pseudobrookit (Fe_2TiO_5) Metalloxid–Halbleiter Material (metal oxide semiconductor, MOS) als Gassensor, und behandelt den Herstellungsprozess und die Messtechnik um die Detektion von gefährlichen Gasen zu optimieren.

Ein großer Nachteil von MOS–Gassensoren ist die relativ hohe notwendige Betriebstemperatur $> 250\,°C$. Der daher notwendige Einsatz einer Beheizung verursacht einen relativ hohen Leistungsbedarf des Sensors. Ausserdem wird dadurch der Sensor Aufbau komplexer und auch teurer.

Das Ziel dieser Arbeit war die Synthese, die Analyse und die Charakterisierung von Pseudobrookit (PSB) Metalloxid–Halbleiter Material für einen Gassensor, der bereits bei Betriebstemperaturen unter $300\,°C$ eine hohe Empfindlichkeit für Stickoxid NO zeigt.

Das erste Kapitel gibt einen Überblick über die wichtigsten Beiträge zur Luftverschmutzung sowie die dafür geschaffenen gesetzlichen Regelungen.

Aus der Vielfalt der existierenden Sensorprinzipien und Sensoren werden die für diese Arbeit relevanten in Kapitel 2 vorgestellt. Das Hauptaugenmerk liegt in diesem Kapitel natürlich auf Metall–Oxid–Halbleiter Materialien (MOS).

Kapitel 3 beschreibt die Herstellung von Pseudobrookit sowie dessen Verarbeitung zu Dickschicht–Pasten. Als Ausgangsmaterialien werden Hämatit (Fe_2O_3) und Anatas (TiO_2) in zwei verschiedenen molaren Verhältnissen, jeweils als Nano–Partikel Pulver verwendet.

Zur Herstellung von PSB als Vollmaterial werden aus dieser Pulvermischung Tabletten gepreßt und mit verschiedenen Parametern gesintert. Die Untersuchung des PSB Materials mit Röntgenbeugung (X–ray diffraction, XRD) zeigt die Formation von ortho–rhombischem und monoklinem PSB, sowie eventuell die Transformation von restlichen TiO_2 Phasen (Atanas, Rutil). Untersuchungen mit dem Rasterelektronenmikroskop (SEM) und mittels Energiedispersiver Röntgenspek-

troskopie (EDS) zeigen den Einfluß der Proz-essparameter auf Korngröße, Porosität und Homogenität des PSB Materials.

Dickschicht–Pasten werden aus dem beschriebenen Nano–Partikel Pulver vorbereitet, unter Zugabe von Butyl–Zellulose als organisches Trägermaterial und Borosilikatglas als Glasfritte. Diese Paste wurde mittels Siebdruck auf Aluminiumoxid gedruckt und in einem Durchlaufofen mit verschiedenen Parametern gesintert. Die so hergestellten PSB–Dickschicht–Proben werden mit XRD, SEM und EDS untersucht.

Im Kapitel 4 werden Impedanzmessungen an den verschiedenen PSB–Samples präsentiert und diskutiert. Die gemessene Temperaturabhängigkeit des elektrischen Widerstands wird zur Abschätzung der Bandabstände sowie der Aktivierungsenergie verwendet. Außerdem wird die DC–Spannungsabhä-ngigkeit des Widerstands bestimmt.

Schließlich wurde die Empfindlichkeit der PSB–Samples gegenüber der NO Konzentration gemessen. Die hergestellten Samples zeigen schon bei relativ niedrigen Temperaturen $< 300\,^{\circ}\mathrm{C}$ eine deutliche Empfindlichkeit für NO Gas. Eine NO Konzentration von 5% in synthetischer Luft konnte bereits bei $150\,^{\circ}\mathrm{C}$ bestimmt werden,

Chapter 1

Introduction

One of the main issues in the 21 st century is for sure growing technological development, followed with increased usage of dangerous substances in various industrial processes. Inevitably, during those industrial processes, it may happen that some dangerous substances are being released, in particular toxic and combustible gases, causing environmental pollution. The adverse effects of pollution are reflected on human health causing various chronic and acute diseases, organ failures, cancer, etc., as well as on the environment causing the greenhouse effect, global warming, ocean acidification, biodiversity and etc. Gas sensors can be used for monitoring, control and detection of harmful gases both outdoor and indoor. They can be used for safety application at work, house, car or in public by monitoring and controlling the air quality and alarming about potential presence of poisonous and combustible gases. Another example of gas sensor application is industry, where the risk of releasing dangerous substances is the highest. Gas sensors are used for process monitoring and control of the concentration of gases in petrochemical, steel, automotive industry, water treatment, power plants etc.

Gas sensors can be realized in many different technologies allowing various advantages and disadvantages one over another. During the past decades, a variety of the state-of-the-art gas sensor technologies have been emerged and the most representative technologies are summarized in chapter 2. One of the most important aspect for all of the state-of-the-art gas sensor technologies is for sure power consumption. Previously mentioned issues brought by the growing technological development imposed the need for distributed gas sensor network with sensors placed on hard accessible areas that can be operated at low temperature with independent (local) low-power supplies. Moreover, by using low-power gas sensors, renewable energy (mainly solar and wind) can be included in for sensor networks which do not have access to a power net.

Currently, the most common types of gas sensors for commercial, domestic and industrial applications are based on metal oxide semiconductor (MOS) gas sensi-

tive materials [1, 2]. Since MOS based gas sensors are requiring elevated working temperatures ($> 250\,^{\circ}\mathrm{C}$), this leads to the need for new materials (or a new material combination) such as pseudobrookite (Fe_2TiO_5) metal oxide semiconductor allowing for a significantly reduced sensing/working temperature. Moreover, PSB material can be used for realization of gas sensors by applying thick film technology.

The main goal of this thesis was to synthesize, analyze and characterize pseudobrookite (chapter 3) metal oxide gas sensitive material and to realize cheap and simple gas sensor which will express sensitivity to nitrogen oxide (NO) gas at low temperatures, below $300\,^{\circ}\mathrm{C}$ (chapter 4).

Pseudoobrookite was selected due to its lower energy band gap of round 2 eV [3, 4] enabling electrons to jump the barrier at moderate temperatures and therefore it has been believed that this material will allow lowering the operation temperature and have therefore been selected as hopeful candidates for this thesis.

In this thesis, a simple hot plate was used for reaching elevated temperatures needed for proper working of gas sensors. Nonetheless, it was though about fabrication of functional gas sensor with an integrated microheater. Such a concept is shown in appendix A, where gas sensor concept with microheater integrated in to the substrate was made in Low Temperature Co-Fired ceramic (LTCC) technology. With this prototype, the issues of thermal distribution and the thermo-mechanical buckling are addressed.

1.1 Background

One of the major forms of environmental pollution is for sure air pollution. In the last century, the most present air pollutants were mainly being introduced by anthropogenic activities such as consumption (combustion) of fossil fuels, emissions from power plants and/or factories, various industrial processes, etc. Of course, there is some contribution from the nature as well (volcanic eruptions, forest wildfires, dust storms, sea spray, plants, animals, etc.) but still they are only minor contributors. Air pollutants can be classified as *primary* or *secondary*, still some pollutants can be classified as both. Pollutants which have been emitted directly from a source are considered to be primary, while secondary pollutants are formed from a primary pollutant through physico-chemical and photochemical interactions or reactions with the surrounding environment. Various types of air pollutants can be distinguished and all of them differ in their reaction properties, efficiency, emission, presence in the atmosphere, ability to be transported for long or short distances, impact on the living world and environment, etc. [5, 6, 7]. A comprehensive overview of the most prominent pollutants with a short description and regulations is given below.

Carbon monoxide (CO) - primary pollutant
It is a colorless, odorless, tasteless, extremely toxic and yet non-irritating gas. It is a product of incomplete carbonaceous fuel combustion (gasoline, natural gas, wood, coal and etc.). It is mainly produced from motor vehicles used in everyday transportation, industrial or household fireplaces and stoves using gas, wood or coal. CO is well known by its affinity toward hemoglobin in blood and myoglobin in muscle tissue, forming carboxyhemoglobin COHb attributing toward acute poisoning due to the interference with oxygen transport. Recent studies have reported pulmonary edema, heart disease, cardiac arrhythmia, electrocardiographic changes and even mortality caused by continuous exposure to CO [6, 8].

Nitrogen oxides (NO_x) - primary pollutant
For air pollution, NO and NO_2 nitrogen oxides are relevant. NO_2 has a reddish-brown color, characteristic sharp, biting odor and it is toxic. NO_x are released during high temperature combustion. Major sources are vehicles, power plants and fossil-burning industries. It can be also produced during thunderstorms by electric discharge and bacterial processes. When oxidized, NO_2 forms nitric acid (better known as acid rain) which has adverse impacts on the living world and environment, such as soil and ocean acidification, vegetation damaging, etc. Nitrogen oxides are responsible for respiratory and pulmonary illnesses, decrements of pulmonary function and oxidative stress which may lead to hospital admission and even mortality [6, 9].

Sulfur dioxide (SO_2) - primary pollutant
It is a toxic gas with an irritating and rotten smell. It is released during the compulsion of coal, petroleum and oil. Furthermore it is released during volcanic eruptions. Sulfuric acid formed from oxidized SO_2 is another contributor to acid rain. Its impact on the living world and environment is described in the previous paragraph. Sulfur dioxide is a respiratory irritant gas pollutant which may cause respiratory and cardiovascular disease and decrements of pulmonary functions which can lead to hospitalization and medical treatment. Furthermore there are indications for a significant effect of SO_2 on mortality [6, 10, 11, 12].

Volatile organic compounds (VOC) - primary pollutant
They are diverse, numerous and omnipresent organic chemicals. Main representatives are methane (CH_4), benzene (C_6H_6), toluene (C_7H_8), n-hexane (C_6H_{14}), xylene (C_8H_{10}), dichloromethane (CH_2Cl_2), tetrachloroethylene (C_2Cl_4), formaldehyde (CH_2O), chlorofluorocarbons (CFS), hydrofluorocarbons (HFS) and etc. Major sources are hard to be determined since VOC are emitted by a wide range of products numbering in the thousands. Notable anthropogenic sources are transportation (vehicle exhaust), petrochemical industry, home and personal care products (cosmetics), building materials (paints, solvents), pesticides, etc. In the nature VOC are produced by plants, animals, bacteria and etc. There have been reports on different types of leukemia and cancer appearance as well as on aplastic anemia, Hodgkin's disease and non-Hodgkin's lymphoma due to the presence of VOC (especially benzene and other polycyclic hydrocarbons) [13, 14]. VOC are also responsible for asthma appearance, airways inflammation, respiratory and pulmonary irritation or/and illnesses, neurological toxicity as well as nervous system damage [14, 15, 16, 17, 18]. As for the impact on the nature, stratospheric ozone depletion and greenhouse effect are attributed to VOC, mainly to CFS and HFS.

Particulate matter (PM) - primary pollutant
This refers to a mixture of particles with various chemical and physical properties suspended in the breathing air. Main representatives are $PM_{2.5}$ for particles with an average diameter smaller than $2.5\,\mu$m and PM_{10} for particles with an average diameter smaller than $10\,\mu$m. Furthermore there are reports on ultra fine particles (UFP) with particle diameters less than 0.1 µm, which have still not been regulated. Major sources are combustion of fossil fuels, various industrial process, volcano eruptions, dust storms, sea spray, forest fire and etc. Particular matters are responsible for respiratory, pulmonary, cardiovascular, cardiac and allergic deceases which may contribute towards premature mortality. Negative effects of PM are enhanced in the presence of other airborne pollutants [6, 7, 9, 19, 20, 21].

Ozone (O_3) - secondary pollutant
Refers to tropospheric O_3 and should not be confused with stratospheric O_3, responsible for protection from ultraviolet (UV) radiation. Is a product of photochemical reactions in the presence of primary pollutants (mainly NO_x, CO and VOC), hydrocarbons and solar radiation. The highest ratios have been reported during warm and sunny weather. Since NO_x, CO and VOC are precursors for the formation of tropospheric ozone, respective sources are applicable. Significant increase of ozone concentrations occurs during the summer period. As for the impact on the living world, ozone is well known as greenhouse gas. Ozone is responsible for respiratory inflammation deceases, pulmonary illnesses, oxidative stress, harmful cardiovascular effects. Furthermore there has been some weak evidence for increment of the mortality ratio due to the presence of O_3 [6, 9, 11, 20].

Ammonia (NH_3) - primary pollutant
This gas does not belong to the VOC group. Is an extremely reactive colorless gas with an acrid smell. Agricultural activities (fertilizers, livestock wastes and etc.), rendering and food industry, sewage treatment, pharmaceutical industry and motor vehicles are the major sources of ammonia [22, 23, 24, 25, 26, 27]. Household appliances (refrigerator) and cleaning products as well can also be sources of ammonia [28, 29]. In nature it is released from the forests, uncultivated vegetation and animals (putrefaction of animals and plants or biomass burning of forests and other vegetation) [25, 30]. Exposure to ammonia at environmental concentrations is unlikely to have adverse effects on the health of mammals. Ammonia does not endanger humans and other mammals due to their specific body mechanism which simply expels ammonia trough urine. However, exposure to high concentrations may cause irritation and in some cases damage of skin, eyes, respiratory tract, mouth, and the digestive tract. At very high concentration organs can sustain severe burns leading toward premature death [29, 31, 32]. Ammonia is a useful compound for growth of plants, nevertheless high ammonia concentrations may be toxic for them. Negative effects are reflected through growth reduction, necrosis and decreased frost resistance, damage of tissue and etc. [22, 33]. Eutrophication with ammonia may cause disturbance in ecosystems particularly influencing the biodiversity perturbation [24, 34, 26, 30].

Persistent organic pollutants (POP)
They are similar to VOC, but still not the same. They have been known as persistent due to the exhibited resistance toward environmental degradation, furthermore they bio-accumulate increasing their adverse effects. POP can be found almost everywhere since they can be transported easily for very long distances. There are countless POP pollutants, still the most known representatives are polynuclear aromatic hydrocarbons (PAH), polychlorinated biphenyls (PCB), polychlorinated dibenzo-*p*-dioxins and-furans (PCDD/Fs) and various organochlorine pesticides [35, 36, 37]. POP are being released from fossil fuel or biomass combus-

tion, vehicle exhausts, industrial processes, agricultural activities and etc. [37, 38]. Of course some POP are being introduced from natural activities, but this is only a minor source. There are reports of POP adverse effects on reproductive, immune and neurological system, liver dysfunction and endocrine disorders. Furthermore some POP cause carcinogenic, toxic and response resulting in deaths [37, 36, 38, 39].

Environmentally persistent free radicals (Persistent free radicals)
Predominant sources are fossil fuel and/or biomass combustion. The most prominent are for sure transportation vehicles, industrial plants, power plants etc. The adverse effects of persistent free radicals are linked to oxidative stress. It has been reported that environmentally persistent free radicals are attributing toward respiratory diseases (mainly asthma) and DNA damage [40, 41].

Polycyclic Aromatic Hydrocarbons - PAH
Polycyclic Aromatic Hydrocarbons are widespread pollutants releasing during the combustion of fossil fuels in motor vehicles, domestic heating, industrial plants and power plants etc. There are reports of PAHs adverse effects linked to respiratory diseases, heart disease, carcinogenicity and DNA mutagenicity [42] as well as to bone marrow toxicity and reproductive toxicity [43].

Report on effects:
According to the World Health Organization (WHO), it is estimated that air pollution in cities and in rural areas was responsible for around 7 million premature deaths worldwide only in 2012 making the air pollution world's largest health risk [44]. It was estimated that outdoor pollution caused around 3.7 million and indoor around 2.9 million premature deaths. Approximately 88% of the deaths caused by outdoor pollution occurred in low and middle income countries [44]. Additionally, WHO provided a more detailed assessment about deaths caused by some specific diseases.

Outdoor air pollution-caused death-breakdown by disease

- 40% – ischemic heart disease;
- 40% – stroke;
- 11% – chronic obstructive pulmonary disease (COPD);
- 6% - lung cancer;
- 3% – acute lower respiratory infections in children.

Indoor air pollution-caused death-breakdown by disease

- 34% - stroke;
- 26% - ischemic heart disease;
- 22% – chronic obstructive pulmonary disease (COPD);
- 12% - acute lower respiratory infections in children;
- 6% - lung cancer.

Regulations: In order to reduce air pollution and to minimize the adverse effects caused by the pollution. In May 2008 the European Union adopted a new general framework directive [45] for air pollution with no change to the existing air quality objectives framework directive 96/62/EC, 1-3 daughter directives 1999/30/EC, 2000/69/EC, 2002/3/EC, and decision on exchange of information 97/101/EC. The adopted standards from the new framework directive can be summarized in Table 1.1 [46].

Another relevant document which regulates and control the air pollution is National Ambient Air Quality Standards (NAAQS) [47] introduced by the United Sates Environment Protection Agency (US EPA). It identifies two types of national ambient air quality standards. The first one is primary, providing public health protection, including ßensitivepopulations such as asthmatics, pregnant women, children, and the elderly. Secondary standards are for public welfare protection, such as protection against decreased visibility, animals, vegetation and buildings. EPA has set standards for six principal pollutants which are listed below in Table 1.2 [48].

Table 1.1: European Air Quality Standards [46].

Pollutant	Concentration	Averaging period	Permitted exceedances each year
$PM_{2.5}$	$25\,\mu g/m^3$***	1 year 3	n/a
PM_{10}	$50\,\mu g/m^3$ $40\,\mu g/m^3$	24 hours 1 year	35 n/a
SO_2	$350\,\mu g/m^3$ $125\,\mu g/m^3$	1 hour 24 hours	24 3
NO_2	$200\,\mu g/m^3$ $40\,\mu g/m^3$	1 hour 1 year	18 n/a
CO	$10\,mg/m^3$	maximum daily 8 hour mean	n/a
Benzen	$5\,\mu g/m^3$	1 year	n/a
Ozone	$120\,\mu g/m^3$	maximum daily 8 hours mean	25 days averaged over 3 years
Lead (Pb)	$0.5\,\mu g/m^3$	1 year	n/a
Arsenic (As)	$6\,ng/m^3$	1 year	n/a
Cadmium (Cd)	$5\,ng/m^3$	1 year	n/a
Nickel (Ni)	$20\,ng/m^3$	1 year	n/a
Polycyclic Aromatic Hydrocarbons - PAH	$1\,ng/m^3$ (expressed as concentration of Benzo(a)pyrene)	1 year	n/a

Table 1.2: NAAQS Air Quality Standards [48].

Pollutant	Type	Averaging time	Level
CO	primary	8-hour	9 ppm
		1-hour	35 ppm
Lead (Pb)	primary and secondary	Rolling 3 month average	$0.15\,\mu g/m^3$
NO_2	primary	1-hour	100 ppb
	primary and secondary	Annual	53 ppb
Ozone (O_3)	primary and secondary	8-hour	0.075 ppm
$PM_{2.5}$	primary	Annual	$12\,\mu g/m^3$
	secondary	Annual	$15\,\mu g/m^3$
	primary and secondary	24-hour	$35\,\mu g/m^3$
PM_{10}	primary and secondary	24-hours	$150\,\mu g/m^3$
SO_2	primary	1-hour	75 ppb
	secondary	3-hours	0.5 ppm

1.2 Motivation

Having better assessment of human exposure to air pollutants by using improved measurements and technology can help in prevention and protection against adverse effects. In addition, information on air quality should be disseminated to the public. Furthermore, reducing the quantities of air pollution is not going to affect just humans, it will also have a positive impact on to the living world and environment. In other words, it will have a positive influence on the entire planet and the life on it. Increasing urbanization is creating greater exposure to the pollutants released from the transportation vehicles, industrial plants and power plants.

We are witnessing that in the recent years diesel engines are taking primate on the market due to the lower fuel consumption, making transportation cheaper and more economical. As already mentioned NO gas is commonly being released from combustion engines using diesel and petrol fuel and thus the necessity for detection of exhaust gases becomes obvious.

The motivation for this research was to provide NO gas sensor which will be operational at low temperatures and thus require low energy consumption. Low-power consumption is of crucial importance for distributed gas sensor networks placed on hardly reachable locations or locations without connection to a power nets. By having low-power consumption, renewable energy sources can be also used.

Since the goal is to have low-power gas sensors working on low temperatures, thermometric and electrochemical types of gas sensors have been excluded from the further considerations, since they operate at temperatures higher than 400 °C and thus require high power consumption.

Of course there are many technologies (chapter 2) where low-power gas sensors working on low temperatures can be realized, but only the MOS based gas sensors are offering the best trade off between fabrication cost, selectivity, sensitivity, life time, reproducibility, level of field robustness, power consumption and working temperatures.

The main goal of this thesis was to synthesize, analyze and characterize pseudo-brookite (PSB) metal oxide gas sensitive material and to realize cheap and simple gas sensor which will express sensitivity toward nitrogen oxide (NO) gas at low temperatures, below 300 °C.

Chapter 2

Gas Sensing Methods

Many different methods for gas sensing have been studied and analyzed. They can be classified according to the type of the sensing material used, measured value (resistance/conductance, capacitance, frequency, mass, transmittance, absorbance, light scattering, reflective index of light etc.) or other kinds of criteria [49].

The most representative gas sensing methods are summarized in this chapter.

2.1 Metal Oxide Semiconductor (MOS)

Gas sensors based on metal oxide semiconductor sensitive materials have been developed since many years. Today, they are one of the most common types of gas sensors for commercial, domestic and industrial applications [1, 2]. They are being used for monitoring the air quality in industrial productions (factories, mines, working cites, etc.) and also for environmental protection caused by industrial production. Moreover they are used for quality control in urban areas where they are controlling and monitoring the air quality in public institutions and households (public, working and living places, public transportation, educational institutions, etc.). They have attracted the attention of the scientific community for the last few decades because of the wide range of target gases (organic and inorganic) toward which they exhibit sensitivity [50]. Gas sensors based on metal oxides exhibit short response time and relatively high sensitivity and selectivity toward a wide range of gases [51, 52]. They proved to have a long lifetime and to be quite reliable and resistant to poisoning [2], therefore they have been intensively used in the industry. Finally, fabrication of gas sensors based on metal oxides as the sensitive material is relatively cheap and simple compared to other types of gas sensors [2, 50].

Of course, gas sensors based on MOS materials are not perfect, they also have some disadvantages. High operation temperature is one of the bigger disadvantages of MOS based gas sensors [53]. Fortunately this drawback can be overcome utilizing microheaters, were pulse operating mode with short heating intervals is being used in order to have minimum power consumption. Another disadvantage is a long recovering period, so that MOS based sensors are not suited for applications such as e-noses or applications where gas concentrations are changing rapidly [53]. Moreover MOS materials have issues with the structural instability and defects limiting their applications. As a solution for this disadvantage as well for the response time, metal oxide nanostructures are being introduced [53].

Metal oxides exhibit a wide range of electro-physical properties, ranging from insulators (e.g. Al_2O_3 and MgO) through wide-band and narrow-band semiconductors (e.g. TiO_2, SnO_2 and Ti_2O_3) to metals (e.g. V_2O_3, Na_xWO_3 and ReO_3) and superconductors (e.g. reduced $SrTiO_3$). Some metal oxides are ferroelectric ($BaTiO_3$) and some are antiferroelectric (WO_3). They can possess ferromagnetic (CrO_2), paramagnetic (RuO_2) and diamagnetic (FeO, NiO) properties [50, 54].

2.1.1 Classification of Metal Oxide Materials

In terms of electronic structure, metal oxide materials can be classified into **transition** and **non-transition** categories. Transition metal oxides have a cation valence orbital with a d symmetry, while the non-transition ones have cation valence orbitals with s and p symmetry. Non-transition category is additionally divided

into *pre-transition-metal oxides* (e.g., Al_2O_3, MgO, etc.) and *post-transition-metal oxides* (e.g., ZnO, SnO_2, etc.) [54].

Non-transition metal oxides have elements that with some exceptions have only one oxidation state on the surface. To create more oxidation states they need a large amount of energy to add or remove an electron from the cations when they are bound to the oxygen ion ligand (O^{2-}) [2, 53].

Post-transition metal oxides have a filled valence band of a predominantly O $2p$ character and a gap between the valence band and an empty conduction band. The band gaps are typically around 3-4 eV. They have filled d orbitals ($3d$ and $4d$) and in addition they have a stable lower oxidation state [54].

Pre-transition-metal oxides have a large band gap and thus holes or electrons cannot be easily formed, therefore they cannot be easily reduced or oxidized. They are also characterized by a high electrical resistance and therefore they are not the most suitable to be used as gas sensitive material due to the difficulties which can be encountered in electrical conductivity measurements [52].

On the other hand **transition-metal oxides** have various stable oxidation states due to the small energy difference between d^n and either d^{n+1} or d^{n-1} cation configurations. Compared to non-transition metal oxides, holes and electrons are easily formed, allowing chemisorptions on the material surface causing significant changes when exposed to gaseous molecules making them preferable for gas sensing applications. However, structure instability and non-optimality of other parameters such as band gap (E_g) and electroconductivity limit their field of application [2, 52].

Theoretically materials with a d^n (where $n \geq 0$) electronic configuration state can be oxidized and reduced easily and thus used as a gas sensitive material. Practically materials with the d^0 configuration possess the highest oxidation state and they cannot be oxidized, but can be reduced. The metal oxide semiconductors with d^0 electronic configuration have bandgaps typically around 3-4 eV, filled valence band of predominant O $2p$ character and a gap between the valence band and an empty conduction band, the same as the non-transition metal oxides. The materials with d^n (where $n \geq 1$) electronic configuration can be potentially reduced and oxidized [52].

Unlike transition-metals oxides with $0 < n < 10$, stoichiometric, post-transition-metal oxides and d^0 transition-metal oxides may be reduced but not oxidized. The majority of transition-metal oxides as well as post-transition metal oxides are active in reduction reactions since the electron configuration of the solid may be changed. However, the reaction with oxidizing species such as O_2 is expected only with specimens that have been bulk reduced or where the surface has been made oxygen deficient. The reduction of post-transition metal oxides leads to the for-

mation of free carriers, which greatly increase conductivity of the metal oxide.This is very important for gas sensing application [52, 49].

In practice only transition-metal oxides with d^0 (e.g., TiO_2, WO_3, V_2O_5, etc.) and post-transition-metal oxides with d^{10} (e.g., SnO_2, ZnO, In_2O_3, etc.) electronic configurations are used as gas sensitive materials [2, 53].

Metal oxide gas sensitive semiconductive materials can be divided into n-type and p-type while some materials can be both n- and p-type. In n-type semiconductors, electrons are the majority carriers and holes are the minority carriers, while in p-type semiconductors the situation is reversed [55].

N-type and p-type metal oxide gas sensitive semiconductors have inverse behavior of electrical resistivity (conductivity) change at interaction with the same gases. The electrical resistivity of n-type semiconductors is decreased when interacting with reducing gases such as carbon monoxide (CO) or ammonia (NH_3) and when exposed to oxidizing gases such as oxygen (O_2) or nitrogen dioxide (NO_2) electrical resistivity is increased. On the other hand, p-type semiconductors exhibit completely opposite behavior, electrical resistivity is increasing when exposed to reducing gases and when exposed to oxidizing gases electrical resistivity decreases.

The most popular and most investigated n-type semiconductors are SnO_2 [55], TiO_2, ZnO, WO_3, and In_2O_3 in pure, mixed or doped form. The most known representatives of p-type are CuO and Co_3O_4 as well in pure, mixed or doped form.

2.1.2 Sensing Mechanism

The true sensing mechanism is not completely and fully known, nevertheless the basic sensing mechanism of MOS materials can be described using the **oxygen-vacancy model** and **ionosorption model** [55].

The Oxygen-vacancy model includes reduction-reoxidation mechanism which occurs at the surface of the material and it will be explained on the example of SnO_2 (n-type) MOS material [55]. Namely is it known that oxygen vacancies in the crystal structure of SnO_2 represent an electron donor. Native donors, such as singly or doubly ionized oxygen vacancies mainly determine the doping level. If the material is exposed to a reducing analyte there will be a reaction between the material and the analyte on the materials' surface, causing partial reduction of the surface of the material. That reduction will cause the creation of more oxygen vacancies which will lead to an enlargement of the number of electrons in the conductive zone and thus the electrical resistance will decrease.

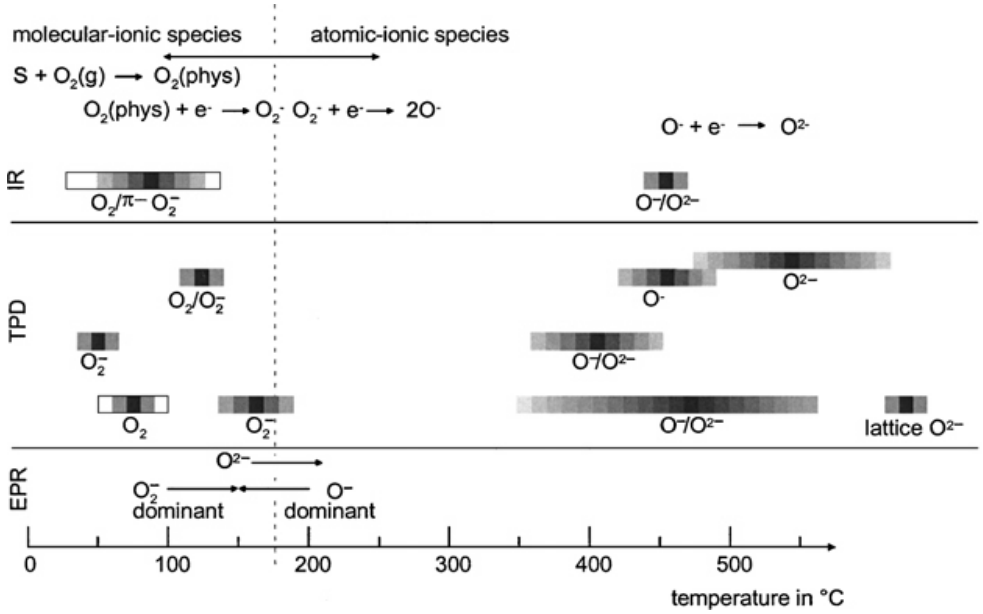

Figure 2.1: Literature survey of oxygen species detected at different temperatures at SnO_2 surfaces with IR (infrared) analysis, TPD (temperature programmed desorption), EPR (electron paramagnetic resonance) [56].

If the material is exposed to an oxidizing analyte or simply if the reducing analyte is being removed, reoxidation will occur on the material's surface. This means that the oxygen vacancies will be filled and as a result the electrical resistance of SnO_2 will be increased. The process and mechanisms described in this model take up a relatively lot of time to occur, compared to the reaction time of the final devices produced with MOS as a sensitive material. Therefore additional models and mechanisms, such as ionosorption (chemisorption) have to be taken into account [55].

The ionosorption model describes the basic sensing mechanism of metal oxide materials and it is explained through oxygen chemisorption on the grain surfaces of the gas sensing material. The process is fast and equilibrium with atmospheric oxygen is reached rapidly. When an n-type MOS material is exposed to regular dry air, the molecular oxygen species ${O_2}^-$ and atomic oxygen species O^- and O^{2-} from the air will be adsorbed at the surface of MOS. Those adsorbed species will trap the electrons from the MOS material and therefore be charged, making the oxygen species to become ionized and therefore ionosorbed. Generally the molecular species are more dominant at temperatures lower than 150 °C, while the atomic species are more dominant at temperatures higher than 150 °C (Figure 2.1) [55] [56].

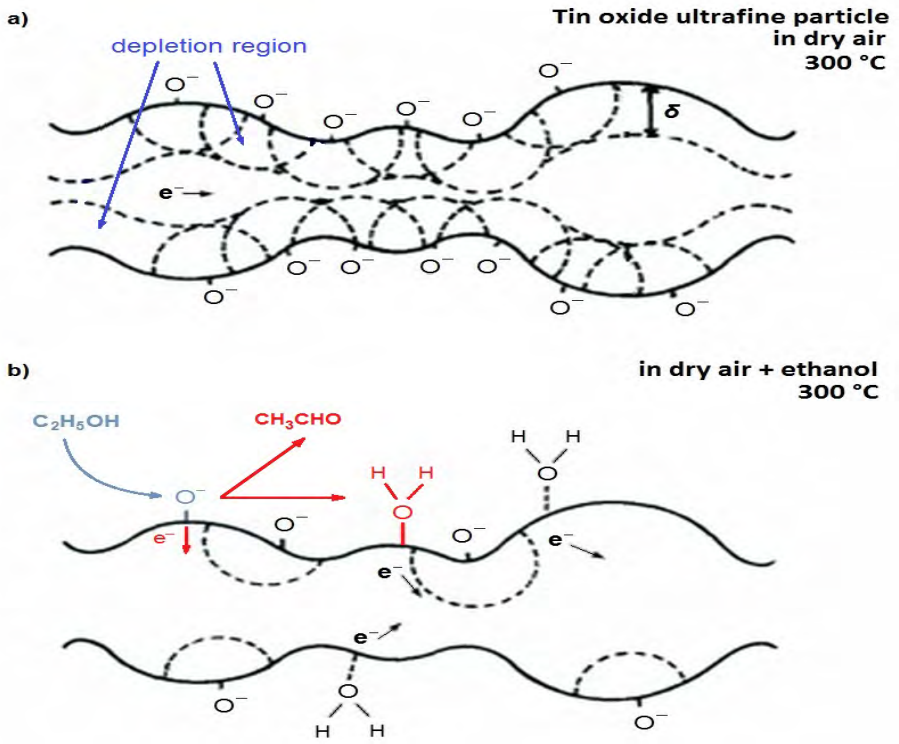

Figure 2.2: Schematic model of oxygen ionosorption on the surface of SnO_2 MOS material in a) pure dry air and b) ethanol. In (a) absorbed oxygen species (O^-, O_2^- and O^{2-}) are trapping the electrons from SnO_2 on its surface and thus form ions that are dispersing the electrons with the Debye length δ of the MOS. As consequence, at the surface of the material an electron depletion region is formed and the mobility of electrons is decreased resulting in an enlargement of electrical resistivity of SnO_2 [55].

The adsorbed ions are dispersing the electrons within the Debye length δ of the MOS causing the formation of an electron depletion region (space-charged layer) at the surface of the material (Figure 2.2a). That depletion region will cause the reduction of the electron mobility and will further cause increase of the electrical resistivity of the material. Depending on the type of gas to which the MOS material is exposed, that depleted region can increase or decrease causing the change of the material's electrical resistance. If it is exposed to reducing gas, such as ethanol (Figure 2.2b), the oxygen species will be removed from the material's surface, releasing the electrons back and thus reduction of the depletion region and the electrical resistivity will occur. If on the other hand the material is being exposed to an oxidizing gas, the number of ionized oxygen species will be enlarged, leading toward enlargement of the depletion region and electrical resistivity.

The equation describing oxygen chemisorption can be written as [57]:

$$\frac{\beta}{2}O_2^{gas} + \alpha e^- + S \Leftrightarrow O_{\beta s}^{-\alpha} \tag{2.1}$$

where $O_2{}^{gas}$ is an oxygen molecule in the ambient atmosphere, e^- is an electron, which can reach the surface, meaning it has enough energy to overcome the electric field resulting from the negative charging of the surface, and their concentration is denoted as $n_s=[e^-]$, S is an unoccupied chemisorption site for oxygen-surface oxygen vacancies, where other surface defects are also considered as candidates. $O_{\beta s}^{-\alpha}$ is a chemisorbed oxygen species, with $\alpha = 1$ for singly ionized forms, $\alpha = 2$ for doubly ionized forms, $\beta = 1$ for atomic forms, $\beta = 2$ for molecular form.

Chemisorption of oxygen consists of an electronic part and a chemical part. This follows from the fact that adsorption occurs as capture of an electron at a surface state, but the surface state does not exist in the absence of the adsorbed atom/molecule. At the beginning of adsorption the limiting factor is chemical (the activation energy for adsorption/dissociation) due to the unlimited availability of free electrons in the absence of band bending. After building the surface charge, a strong limitation coming from the potential barrier has to be overcome by the electrons in order to reach the surface (Figure 2.3). From the start desorption is controlled by both electronic and chemical parts. The activation energy does not change during the process if the coverage is not high enough to provide interaction between the chemisorbed species. The analysis of oxygen adsorption, desorption and diffusion was simplified assuming that the main adsorbed oxygen species on the film surface are $O_{ads}{}^-$ [57], reducing the relevant reactions to:

$$\frac{1}{2}O_2^g + S \Leftrightarrow O_{ads}^0 \tag{2.2}$$

$$O_{ads}^0 + e^- \Leftrightarrow O_{ads}^- \tag{2.3}$$

where S denotes a surface site, e^- is an electron and O_2 an oxygen molecule in the gas phase. Adsorbed oxygen leaves its site creating a doubly ionized interstitial ($O_{int}{}^{2-}$):

$$O_{ads}^- + e^- \Leftrightarrow O_{int}^{2-} + S \tag{2.4}$$

Then interstitial oxygen migrates from the surface to the bulk annihilating oxygen vacancies:

$$V_O^{2+} + O_{int}^{2-} \Leftrightarrow O_{latt} \tag{2.5}$$

where $V_O{}^{2+}$ denotes doubly ionized oxygen vacancy and O_{latt} oxygen in the lattice. All reactions are in equilibrium and the concentrations of the species

involved depend on the partial pressure of oxygen. Thus the basic mechanisms involving oxygen are: a) Oxygen adsorbs in the atomic form and desorbs as oxygen molecules; b) Oxygen adsorbed on the surface diffuses into the grain as interstitials; c) Oxygen may also diffuse out of the grain to be incorporated at the surface and d) oxygen vacancies and oxygen interstitials recombine to generate oxygen in the lattice, as illustrated in Figure 2.3.

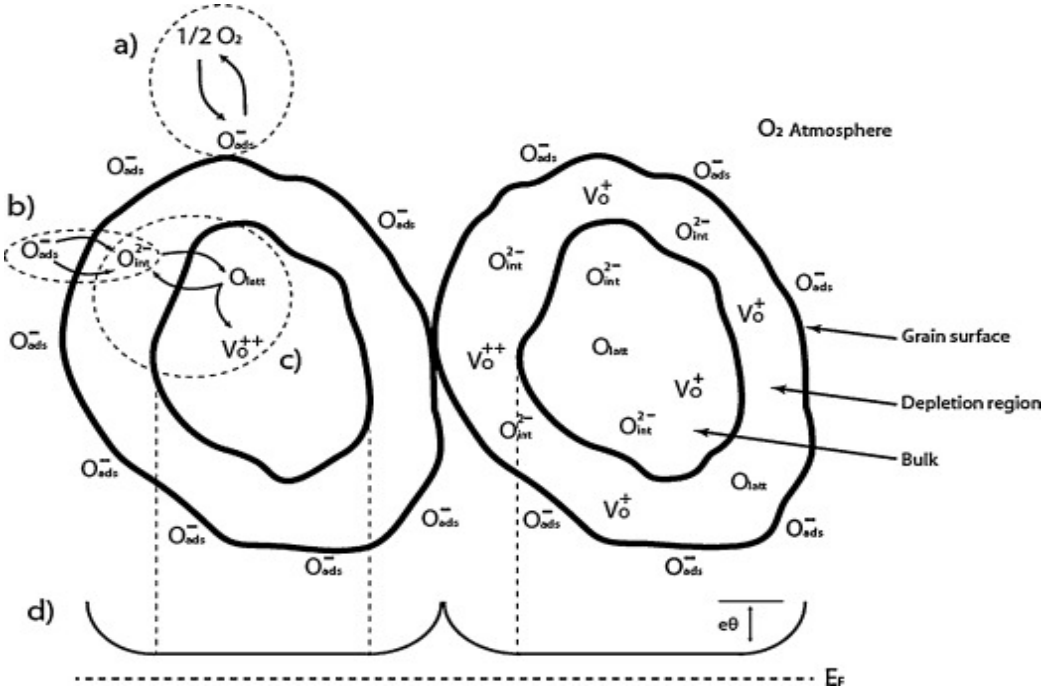

Figure 2.3: Basic mechanisms in n-type thick film sensors a) Oxygen adsorbs in the atomic form and desorbs as oxygen molecules; b) Oxygen adsorbed on the surface diffuses into the grain as interstitials; c) Oxygen may also diffuse out of the grain to be incorporated at the surface and d) Oxygen vacancies and oxygen interstitials recombine to generate oxygen in the lattice [57].

Absorbed oxygen species will trap the electrons on the material's surface and therefore they will extract the electrons from the conduction band that would further cause the upward band bending, as illustrated in Figure 2.4. The length of the band bending region is the thickness of the depletion region (Debye length δ). An illustration of a physical model with energy zone diagram, including double Schottky barrier in polycrystalline oxide layer, is given in Figure 2.5.

2.1.3 Grain Size Effect

Electron mobility is directly proportional to the concentration of ionosorbed oxygen species. Despite that, the actual change in electron mobility is significantly

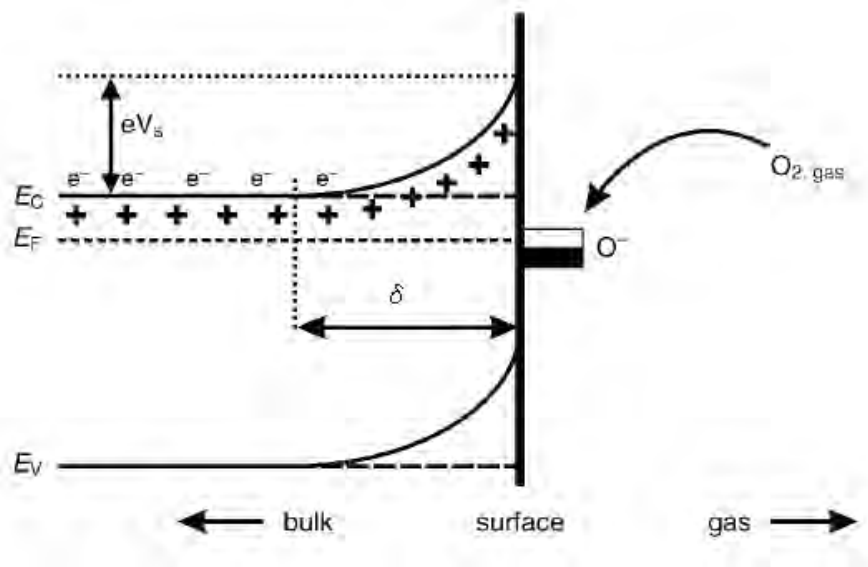

Figure 2.4: Schematic diagram of band bending after chemisorption of charged oxygen species. EC, EV, and EF denote the energy of the conduction band, valence band, and the Fermi level, respectively, while δ denotes the depth of depletion region and eVs denotes the height of the potential barrier. The conducting electrons are represented by e– and + represents the donor sites [50].

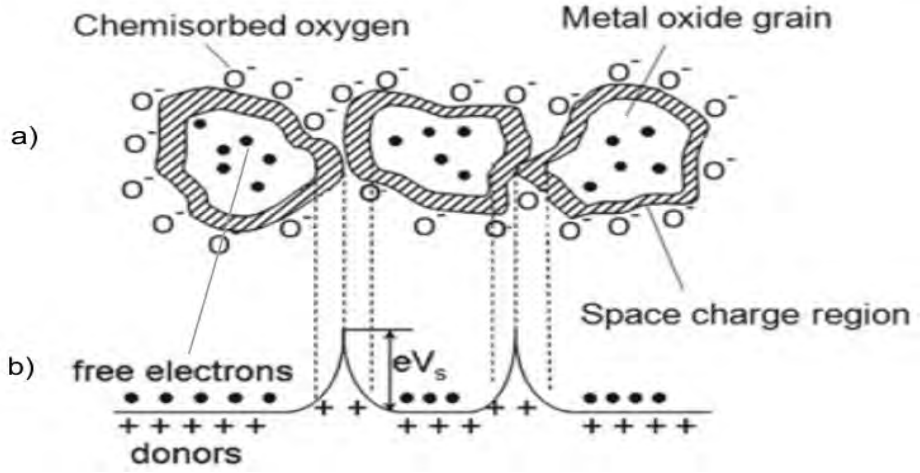

Figure 2.5: Schematic model of double Schottky barrier in polycrystalline MOS: a) physical model; b) energy zone diagram, eV_s denotes the height of the potential barrier [49].

affected by the grain size, the morphology of the material, defects and connectivity between particles [58, 55]. Namely for the grain size effect (Figure 2.6), the main factor is the ratio between the grain diameter (D) and the Debye length δ. If the grain diameter is much larger than the δ ($D \gg \delta$), the sensing mechanism is fully controlled by the grain boundaries (Figure 2.6 a). Compared to the bulk material, the depletion region will have insignificant contribution to the overall electrical resistivity and therefore this is the case when low sensitivity is expected as only a small part of the MOS is affected by interactions with the analyte. When $D \approx \delta$ (Figure 2.6 b), the conductivity channel is established, but the width of the channel (Ls) is dependent on the concentration of the absorbed oxygen ions on the material's surface. The depletion region is now significantly contributing to the overall electrical resistance as a larger part of the MOS is affected by interaction with the analyte and thus this is the case of moderate sensitivity. In the case that the grain size is much smaller than δ ($D \ll \delta$), we have a situation that the entire electrical resistivity is being controlled by the depletion region and this is the case of high sensitivity.

The microstructure of polycrystalline metal oxides is important when determining the number of junctions present and the nature of intergranular barriers. The nature of intergranular junctions is mainly dictated by the n-type semiconducting features of grains, due to oxygen vacancies acting as shallow donors. The barriers formed between particles or grains have a Schottky-type nature. The negative charge due to chemisorbed oxygen at grain surface increases the Schottky barriers at the intergrains and has a significant influence on electrical conduction in polycrystalline semiconductors [59].

In the case of n-type semiconductors the sensor resistance is mainly determined by the resistive shell-to-shell contacts formed between particles, so equivalent circuits can be explained as serial connections between semiconducting cores and resistive interparticle contacts (Figure 2.7) [60]. If hopping of electrons from one grain to another in the sensing layer controls electrical conduction then electron concentration participates in conduction [56]. The electroneutrality equation in the Schottky approximation states that the charge in the depletion region is equal to the charge captured at the surface. At high enough temperatures all donors are ionized, then all electrons from the depletion region are captured on surface levels. Two limiting cases can be distinguished: grains/crystallites are large enough to have a bulk region unaffected by surface phenomena or they are smaller. When they are smaller it is important to evaluate the band bending between the surface and the center of the grain.

2.1.4 Conduction Mechanism

Barriers formed between grains are generally responsible for changes in sensor conductivity [56, 61]. The first approach to barrier height calculations considered

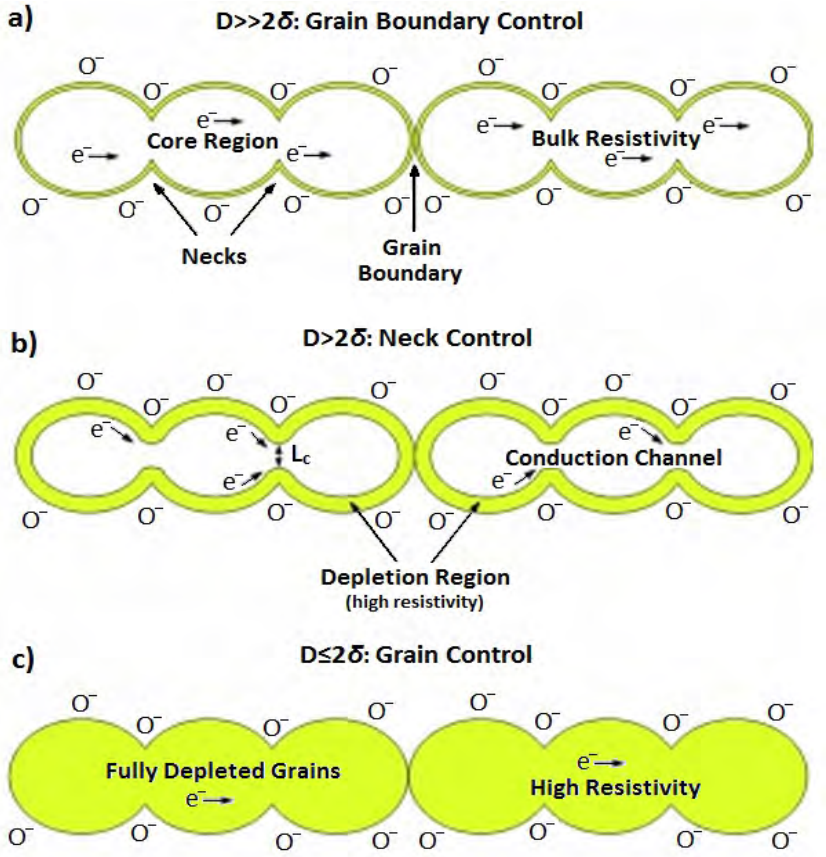

Figure 2.6: Control of electron mobility and thus resistivity (conductivity) change depends mainly on the ratio between grain size(D) and Debye length δ. If $D \gg \delta$ (a), the overall material resistivity is controlled by depletion of the surface between grain boundaries and in this case low sensitivity to the analyte is expected. If $D > \delta$ (b), a conduction channel with low resistivity exists but its width (Lc) is controlled by the surface concentration of oxygen ions leading to moderate sensitivities. If $D \leq \delta$ (c), the whole grain is depleted and changes in the surface oxygen concentration affects the whole semiconductor resulting in high sensitivity [55].

only the thermionic conductivity (G) of n-type semiconductors [57]:

$$G = G_0 exp(\frac{-\phi}{kT}) \tag{2.6}$$

where ϕ is the barrier height, T is the temperature and k is the Boltzmann constant. This equation reflects an activated process due to intergranular barriers. However, as the oxygen concentration increases, there is a larger amount of chemisorbed oxygen and this will increase the potential barrier height and

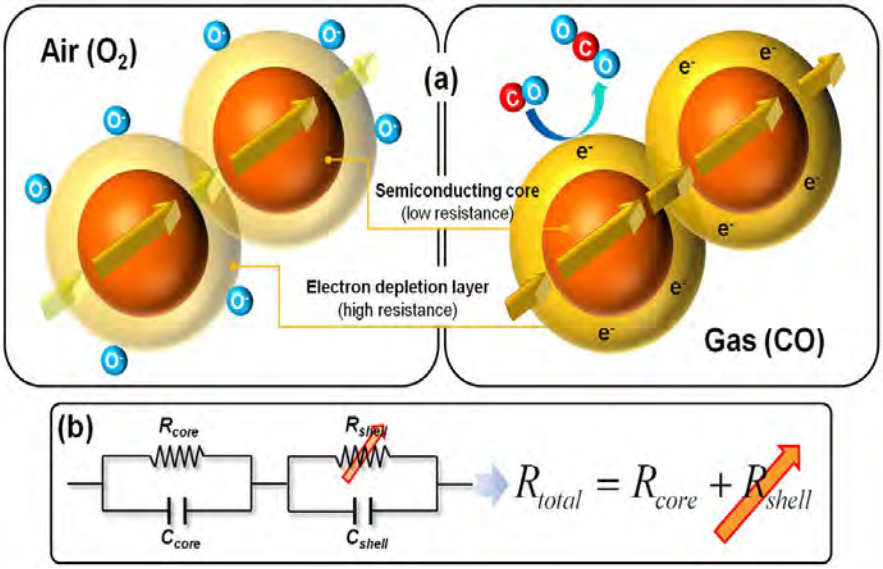

Figure 2.7: Gas-sensing mechanism and equivalent circuit of n-type oxide semiconductors [60].

decrease thick film sensor conductivity. The relationship between the potential barrier height and donor concentration can be given as [57]:

$$\phi = \frac{q^2 N_2^2}{2\varepsilon_r \varepsilon_0 N_d} \tag{2.7}$$

where N_d is the donor concentration, N_s represents the number of electrons (per area unit) extracted from the depleted surface region (Λ), ε_r is the relative permittivity, ε_0 is the permittivity in vacuum and q is the electron charge. As an n-type semiconductor has a double Schottky barrier ($2N_d = Nx$) the following relation is valid:

$$\Lambda = \left[\frac{2\varepsilon_r \varepsilon_0 \phi}{qN_d}\right]^{1/2} \tag{2.8}$$

In this case the depletion layer region has been measured at the barrier bottom.

The relationship between the surface band bending and measured resistance/ conductance of the sensitive layer depends on the layer morphology [56]. Commonly the layers are divided into compact or porous. In the case of compact layers the interaction with gases takes place only at the (smooth) outer surface, while in the case of porous layers the volume of the layer is also accessible to the gases increasing the active surface. Thick film technology allows producing porous layers, so attention will be paid to this case. In the case of porous thick film layers the conduction process takes place due to surface/bulk (due to the presence of

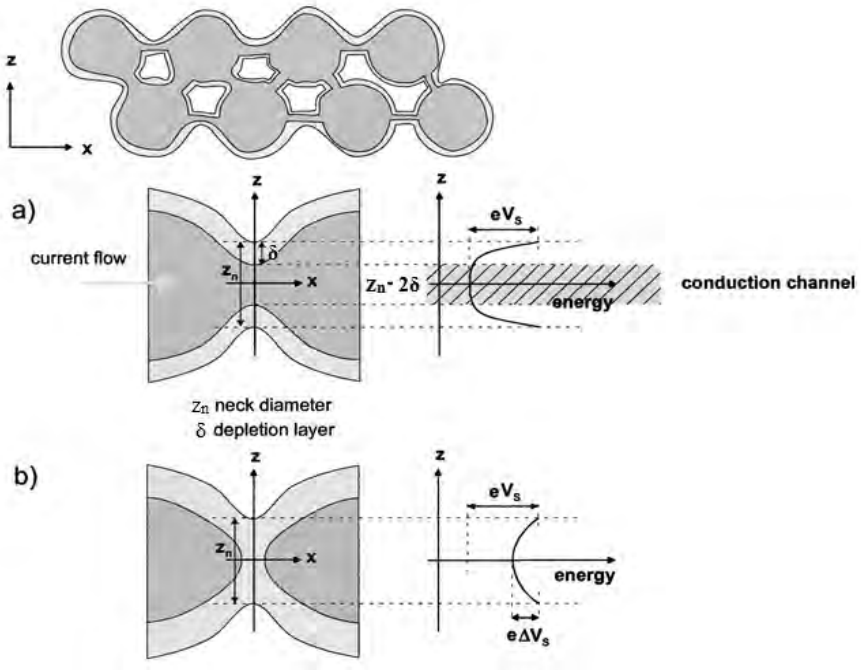

Figure 2.8: Schematic representation of a porous sensing layer with geometry and surface band energy a) partly depleted necks b) large grains where the neck contact is completely depleted, z_n is the neck diameter, δ is Debye length [56].

necks between grains), grain boundaries (for large grains not sintered together) and flat bands (for small grains and small necks), Figures 2.8 and 2.9. In the case of small grains and narrow necks when the mean free path of free charge carriers is comparable with the grain dimensions a surface influence on mobility also needs to be taken into account.

In the case of n-type semiconducting compact layers the conductance can be defined as:

$$G = AqN_b\mu_b \tag{2.9}$$

where A is a constant that includes sample geometry, N_b is the bulk charge/carrier concentration, μ_b is the bulk electron mobility. When the surface effects are included the conductivity depends on the depth, so the conductance needs to be integrated over the entire thickness.

In the case of porous layers the charge carrier transport from one grain to another is controlled by the inner surface barriers of mechanisms similar to the ones occurring in compact layers (Figure 2.9). Layers controlled by inner surface

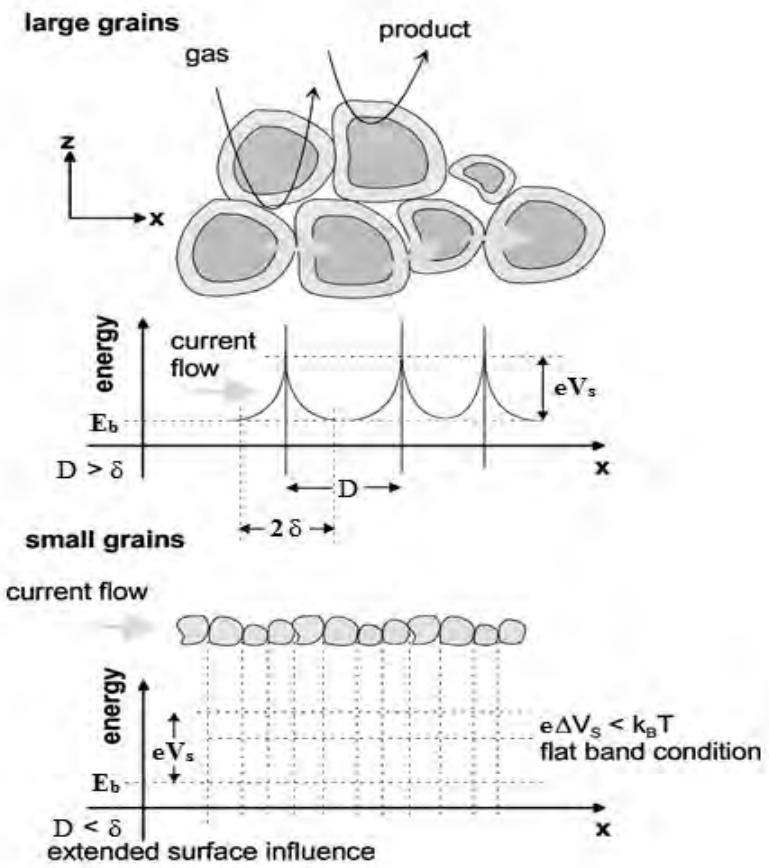

Figure 2.9: Schematic representation of a porous sensing layer with geometry and energy band, δ Debye length, D grain diameter, eV_s is the height of the potential barrier [56].

barriers can be classified according to grain dimensions.

The influence of the metal-semiconductor junction in sensors on the overall conduction process is shown in Figure 2.10. In the case of compact layers the contact resistance (R_C) is serially connected to the resistance of the sensor layer (a). In the case of a porous layer the influence of contact resistance could be minimized due to geometry and energy bands, showing possible influence of electrode-sensing layer contacts

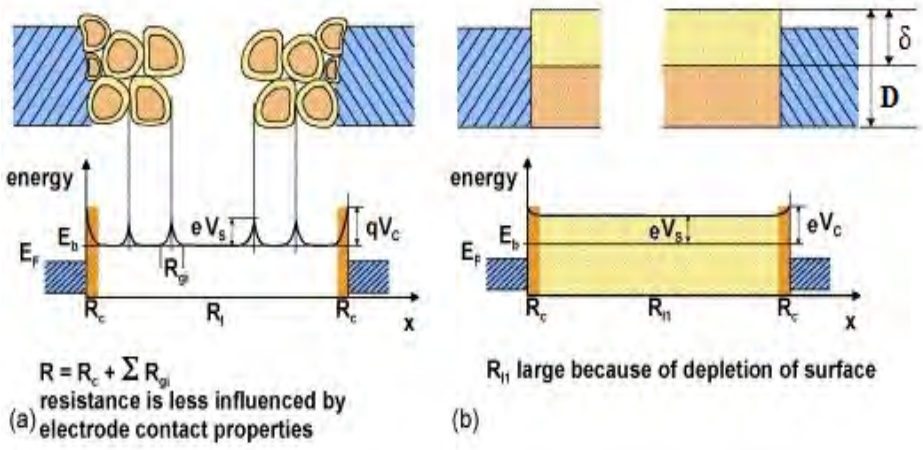

Figure 2.10: Schematic representation of compact and porous sensing layers with geometry and energy bands, showing possible influence of electrode-sensing layer contacts [61].

2.2 Polymer Based Gas Sensors

Gas sensors based on metal oxide semiconductor materials exhibit great sensitivity toward a wide range of gases. However, detection of some volatile organic compounds (VOC) using gas sensors based on MOS, can be difficult. On the other hand, gas sensors based on polymer materials are known for their greater sensitivity toward volatile organic compounds (VOC) and some inorganic gases (NH_3, NO, NO_2, SO_2 etc.) [49]. The working principle of those sensors is quite similar to the gas sensors based on MOS. When the polymer material is exposed toward an gaseous analyte, reactions between the polymer and analyte will occur leading to a change of physical properties of the polymer material. Physical properties such as resistance, conductance, capacitance, inductance (dielectric properties) and mass will change upon reaction with the targeted gas [53]. The sensing mechanism can be explained through various physisorption mechanisms which include hydrogen bonds (Lewis acidity/basicity-concept), dipole induced/dipole induced interactions (London dispersion), dipole/dipole interactions and dipole/dipole induced interactions [53, 62].

Due to the different sensing mechanism, compared with MOS base sensors, polymer based gas sensors can detect gases already at room temperature giving them great advantage [53]. Polymers are relatively easy to synthesize and their molecular chain structure can be modified. Moreover, they exhibit high sensitivity, short response time, good mechanical properties and production is relatively easily achieved [63].

Their disadvantage is a relatively low electrical conductivity in pure state, making them difficult to be used in such condition. Other disadvantages are poor selectivity and low long-time stability making them undesirable for applications where monitoring over a longer period of time is needed. Moreover, gas sensors based on polymer materials are irreversible, meaning that after a chemical reaction between the polymer and targeted gas, the polymer material will not return to the previous state as it was before the gas exposure [53]. Polymers used for gas sensing are classified as conducting and non-conducting.

The most straight forward operation principle of non-conductive polymers is the principle of a capacitance sensor, where the polymer material is swelling due to the gas exposure, which will further cause changing of the materials' volume and dielectric permittivity. Non-conductive polymers have been used in most cases as a sorptive material, where the polymer is actually used as a coating material for some other respective transducer. As already mentioned, polymers change their physical properties and mass, when exposed toward targeted gases. Therefore if a polymer is applied as a coating on calorimetric, mass-sensitive (eg. Quartz Crystal Microbalance (QCM) or Surface Acoustic Wave (SAW), described in chapter 2.4),

or dielectric sensor devices it would cause change in enthalpy, resonant frequency or dielectric permittivity, respectively [53, 49].

Conductive polymers change their electrical conductivity as a result of gas exposure and reaction. Polyaniline (PAni), polyacetylene (PA), polypyrrole (PPy), polythiophene (PTh) and their derivatives are common conductive polymers used for gas sensing application. It is important to note that the electrical conductivity of a pure polymer is rather too low ($\sigma < 10^{-5} S/cm$) to be used as a gas sensitive material. In order to overcome that problem, polymers are being doped by redox reactions or protonation after which they become semiconductors or conductors ($\sigma \approx 10^{0} - 10^{5} S/cm$). The doping process is completely reversible meaning that the doped polymer can be easily returned into the previous undoped state by chemical or electrochemical reductions. The doping level can be changed after the exposure and reaction with targeted gas, making them irreversible. In this application, conductive polymers can be defined as transducers which directly reflect the changes, due to a reaction between the gas and polymer, by a change of an electrical signal [53, 63]. They can be also used for realization of thin film transistors (TFT) where the conductive polymer layer is used as an active layer (gate) and diode gas sensors where change in transmittance or absorbance is measured [64, 49].

2.3 Optical Gas Sensors

Optical gas sensors are working on the principle of detecting changes in optical phenomena which occur as a result of interactions between analyte and the light. Optical gas sensors have general advantages in terms of operating at room temperatures, resistance to corrosive or reactive gaseous analyte, contact free measurements, relatively fast response and they can be used for detection of flammable gases [65, 53]. They can detect a wide range of gases and moreover they have capability to detect different types of gases in the same atmosphere by using differences in the polarization, wavelength, intensity and phase of the probe light signal, giving them great advantage for gas selectivity. By using optical fibers, optical gas sensors exhibit a capability for remote monitoring as well as a possibility for local and distributed gas sensing. In addition, usage of optical fibers allows optical gas sensors to be flexible, environmentally robust and compact [65]. On the other hand, bulk optical systems for gas sensing exhibit disadvantages of massive size, high costs, low level of field robustness and miniaturization. Moreover due to the presence of mist, smoke, steam etc., the measurement range of the frequency bands will be reduced. Additional non solved issues are related to fouling (dust, dirt etc.) and /or condensation of moisture on parts of the measuring system which are exposed to the measuring environment [65, 53].

There are various configurations of optical gas sensors (Figure 2.11) [49]. The most primitive construction of an optical gas sensor is comprised of a light source and a detector. Other versions can have a wavelength selector, a recognition element used for identification and interaction with the target gas and also a transducer element for converting the interaction with the gas into a detectable and processable signal. The mode of operation of optical gas sensors strictly depends on the chemical and physical properties of the targeted gas and it determines the type of interaction with the sensitive chemistry.

The basic working principle is the following: the light source is generating light which is modulated and emitted toward the targeted gas. While passing through the gaseous environment, certain changes of light parameters occur. After interaction with the targeted gas, light is reflected or directed toward the detector enabling detection of changes and thus information about the type of gas can be extracted.

In many cases measurements are not made directly meaning that light is not directly emitted toward the gas, yet it is emitted toward an indicator. The need for an indicator is determined by the analyte itself. If an analyte has an intrinsic optical property, light is emitted directly, if that is not the case an indicator will be used. The targeted gas will react with the indicator, changing its optical properties such as the reflection or absorption index, photoluminescence intensity,

reflective index etc. The generated light will be emitted (or reflected) toward the indicator and the occurred changes will be detected.

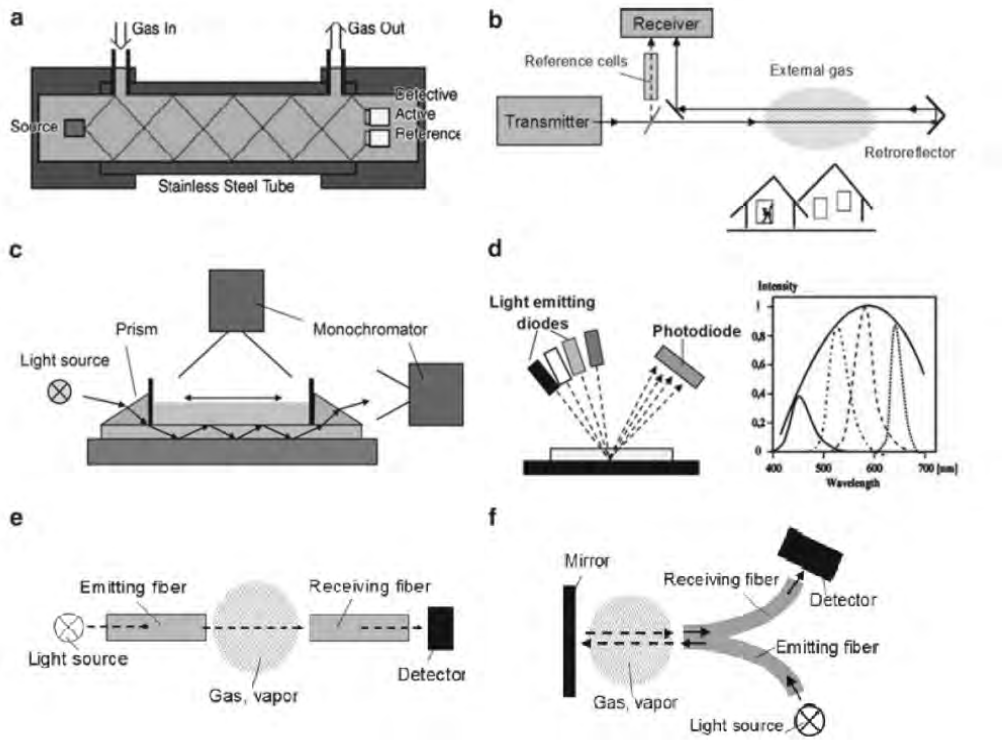

Figure 2.11: Examples of different types of optical sensors: (a) configuration of portable analyzer for detection of methane gas in a stainless steel tube, (b) set up for atmosphere monitoring using reflector, (c) waveguide configurations for measurements of absorbance, scattering (Brillouin and Raman) and luminescence, (d) experimental setup with light emitting diodes, (e) and (f) variations of optical gas sensors with implementation of optical fibers [49].

The most common gas sensing techniques are for sure spectroscopic techniques with all their numerous variations. Spectroscopic analysis is mainly based on optical absorption or emission of a targeted gaseous analyte at a specific wavelength. The distribution of absorption or emission with wavelength gives a so-called optical fingerprint of specific gas. The wavelength distribution of a chosen optical characteristic allows identification of the presence of the targeted gas, while the intensity of the characteristic spectral distribution gives information about the concentration of the gas. Absorption spectroscopy is based on the concentration dependent absorption of emitted light at a specific gas wavelength. The principle

of emission spectroscopy is based on the emitted photons of exited atoms which are going back to the ground state. Mentionable representatives for spectroscopic techniques are Differential Optical Absorption Spectroscopy (DOAS), Differential Absorption LIDAR (DIAL), Tunable Diode Laser Absorption Spectroscopy (TDLAS), Laser-Induced Breakdown Spectroscopy (LIBS), Raman Light Detection and Ranging (LIDAL), Fourier Transform Infrared Spectroscopy (FTIR), Intra-Cavity Absorption Spectrometry (ICAS) etc.

Many gaseous analytes have shown very strong absorption in the near infrared, mid infrared and ultra violet spectrum [66]. In case of infrared spectroscopy, the concentration of a targeted analyte can be measured on the base of a characteristic spectral absorption or more precisely the change of spectral intensity due to both, absorption and emission by the gas in question with respect to the reference response with no gas is detected using this method. By using this method the obtained absorption lines or bands of every gaseous analyte exhibit unique characteristics, meaning that every gaseous analyte has a unique absorption fingerprint. Infrared and ultraviolet spectroscopes are mainly used when the analyte has an intrinsic optical property. The most widely techniques used are optical absorption, fluorescence and chemiluminescence.

2.4 Acoustic Gas Sensors

Acoustic based gas sensors are used to overcome issues of short lifetime and secondary pollution, making that their main advantage [53]. On the other hand, acoustic based senors are exhibiting low sensitivity, large power consumption [53] and they are sensitive to environmental change [65].

Measuring parameters which are being observed in acoustic based gas sensors are: speed of sound, attenuation and acoustic impedance. The most investigated parameter is speed of sound, which uses the travel time of acoustic wave to obtain the information about the propagation velocity of the wave [53]. From the measured propagation velocity, concentration and type of the gaseous analyte can be obtained. Big drawback is that this method rather needs high power consumption [53]. During the propagation of an acoustic wave through a targeted gaseous analyte, the wave there will be a certain thermal or scattered energy lost, this phenomenon is known as an attenuation of the acoustic wave [53]. Depending on the type of analyte, different attenuation properties will be demonstrated and using that information, individual gases can be easily detected and recognized. However, the attenuation method is less robust regarding the impurities in the gaseous analyte (droplets and/or particles), making them undesirable for commercial application [53].

Acoustic impedance is usually used for determination of the gas density. In practice, measuring gas acoustic impedance is quite difficult so they are not been widely used for commercial application [53].

Quite frequently a gas sensitive material is used [65]. In that case the working principle is based on propagation of an acoustic wave along the surface or through the bulk of the sensitive material. Implementation of an acoustic gas sensor relies on the sensitivity of an acoustic wave towards small changes occurring at the active surface of the sensitive material. The gas sensitive material will react with the targeted gaseous analyte causing small but still visible changes in the waves' properties allowing detection of the targeted gas.

Acoustic wave gas sensors with an implemented gas sensitive material are generally divided in two types. The first one is focused on wave propagation in through the bulk of the sensitive material and they are known as bulk acoustic wave (BAW). The main representative of this type, among others, is Quartz Crystal Microbalance (QCM). The second representative type is focused on the propagation of an acoustic wave on the surface of the sensitive material, and the main representative is Surface Acoustic Wave (SAW) [65]. QCM is classified as mass sensitive, while SAW is sensitive toward changes in sheet conductivity of the gas sensitive material.

Reaction of the targeted gaseous analyte and the gas sensitive material is reflected on the perturbation of the phase velocity of the propagating wave, where perturbation is directly related with the concentration of the analyte. Usually phase shift, resonate frequency and attenuation are measured, but in the case of QCM measurement of impedance is also possible.

QCM is for sure the most commonly used acoustic wave based gas sensor [65]. Typically it is comprised of a thin circular quartz crystal, which has metal electrodes on both sides. The gas sensitive material is deposited on top of the metal electrode (Figure 2.12). The working principle is based on mass changes on the surface of the gas sensitive layer when interacting with the targeted gaseous analyte. The mass changes will be reflected in the response of the resonating frequency. Different gases will cause different mass changing and thus a specific gas can be detected.

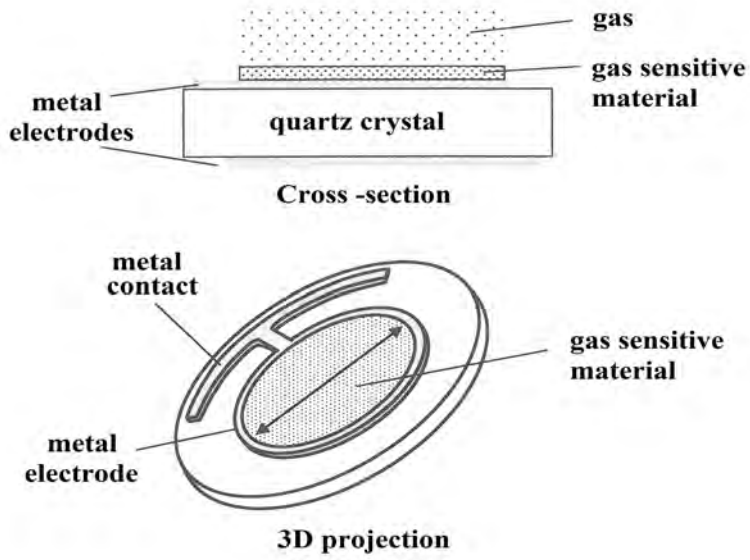

Figure 2.12: Example of a typical QCM gas sensor with gas sensitive material with cross-section and 3D projection view [65].

Regardless of the type of the sensing material, the characteristics of QCM gas sensors will be the same. However the period of exposure, non-reversibility of the sensing material, gas concentration as well as presence of other gaseous analytes can considerably affect the performance of the sensor. In quite a lot of cases organic polymers are used as a gas sensitive material. In other cases metal oxide semiconductor materials and more recently organic monolayers, molecular imprinted polymers (MIPs) and of course carbon nanotubes are also used as a gas sensitive material [65].

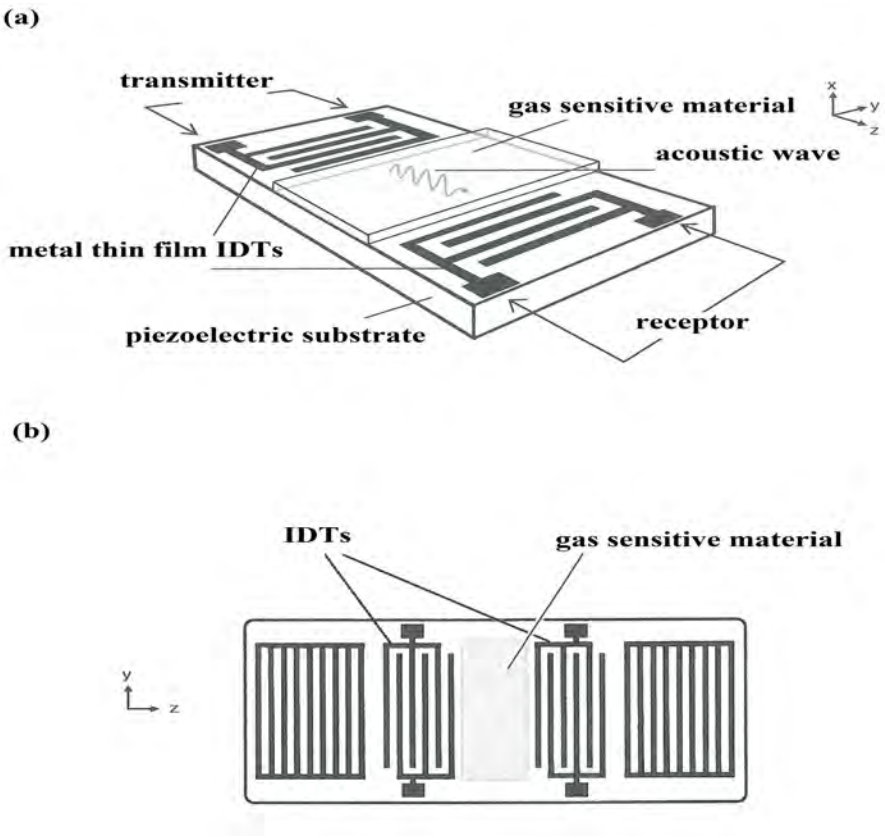

Figure 2.13: Illustration of two typical SAW gas sensors arrangements with a gas sensitive material (a) 2-port delay line SAW and (b) 2-port line SAW resonator [65].

SAW are typically comprised from a piezoelectric substrate on top of which two interdigital transducers are deposited on different sides of the substrate, Figure 2.13. One transducer serves as transmitter of the acoustic wave while the other one serves as receptor. The transducers are separated so that a delay path between the transmitter and receptor can be created. The gas sensitive material is usually deposited between the transducers but sometimes it can be deposited over the entire structure.

By applying an electrical signal on the transmitting transducer an acoustic wave will be exited. The wave will propagate through the gas sensitive material, interact with it and continue toward the receptor where the wave will be converted again into an electrical signal. While interacting with the sensitive material the properties of the acoustic wave will be altered. SAW sensors exhibit excellent sensitivity toward surface perturbations. These perturbations are causing change

of phase, frequency or a shift in propagating acoustic mode's phase velocity. In any case, the measured changes are strongly correlated to the targeted gaseous analyte.

2.5 Carbon Nano Tubes (CNT) Based Gas Sensors

Carbon nanotubes (CNTs) have recently attracted a lot of attention from the scientific community due to their sensitivity toward extremely small amounts of gases at room temperature. CNTs are classified in to two types. The first type is single-walled carbon nanotubes (SWCNTs) and as the name says it has only one layer of graphene, which is rolled in a form of a cylinder. They are usually used for sensing of toxic gases [53]. The second type is multi-walled carbon nanotubes (MWCNTs), and has multiple coaxial layers of graphene cylinders. They are usually used for sensing oxygen (O_2), carbon dioxide (CO_2) and ammonia (NH_3) [53]. SWCNTs are about 0.5 nm to 3 nm in diameter and from 1 μm to 100 μm long, while MWCNTs are about 2 nm to 25 nm in diameter, with 0.34 nm distance between the layers [67].

Because of their nanosize, CNTs possess a large surface-area-to-volume ratio and great adsorptive capacity resulting in extreme sensitivity with rapid response time and significant changes of electrical properties of CNTs [53, 64]. Since they can operate at room temperature, naturally the power consumption is quite low allowing them to have a simple configuration. Moreover they have low weight, they are very resistant toward corrosion [53] and according to Lakkis et al. the cost of manufacturing is low [64]. However, this opinion is questionable according to some other sources. Synthesis of CNTs is relatively complex and it is quite challenging to reproduce CNTs with controlled physical and chemical properties [67]. Synthesizing only semiconducting SWCNTs with high purity and uniformity without defects is still difficult. Because of the empirical synthesis process separation and selection of CNTs with similar physical characteristics is quite complex and demanding, making the fabrication costs even higher. CNTs have a tendency to deform. There have been reports about deformation of two near nanotubes by van der Walls forces [67].

The fast response time of the sensor is also brought to question, due to the slowness of the adsorption/desorption processes [67]. Recovery time of CNTs based gas sensors can be up to several hours and quite often recovery is not complete, meaning that the sensing process is partly irreversible. Still, the recovery time can be sped up by applying elevated temperatures (165 °C) or ultraviolet (UV) light [67]. The disadvantage of CNTs based gas sensors about which most authors are agreeing is low selectivity toward gases or mixtures of gases [67]. Although the number of gases toward CNTs is sensitive and selective, many authors are naming CNTs the most promising gas sensitive material of the future.

The most accepted approach to describe the sensing mechanism is by observing the adsorption/desorption phenomenon taking place at the surface of SWCNTs [67]. This approach is commonly related to SWCNTs because they have better performance than MWCNTs and SWCNTs can be either metallic or semiconducting

depending on various parameters, while MWCNTs are only metallic and thus they are not suitable [67]. The working principle is quite simple: CNTs exhibit change of electrical resistance and/or capacitance when reacting with a gaseous analyte. The ones where the electrical resistivity is affected are referred to as chemiresistors and they are seen as the most promising types of gas sensors based on CNTs. There are reports that several gases can be detected at room temperature using CNTs, however for some (CO and H_2) elevated temperatures are needed [67].

Using this approach high sensitivity can be achieved but on the other hand it is very hard to distinguish the type of gaseous analytes which are being detected, making the selectivity low. Another drawback of this method is its sensitivity toward temperature changes, moisture and gas flow rate [68]. All of the listed parameters influence the electrical resistance of CNTs making this sensor principle less attractive.

Every gas has a unique breakdown voltage at constant pressure and temperature, making a unique gas fingerprint. Normally this method would require a very high voltage source but with implementation of CNTs, a high electrical field is achieved with a relatively low voltage due to the sharp tip curvatures of CNTs. Using the ionization technique it is possible to distinguish specific gases. Furthermore this technique does not include gas adsorption and desorption, allowing the sensor to have a faster response and to be immune to irreversibility [68].

As already mentioned, CNTs are sensitive toward a limited number of gases and they express poor sensitivity for others. In order to improve the sensitivity and selectivity, quite often the CNTs are mixed with silane or oligonucleotides (Deoxyribonucleic acid (DNA) and Ribonucleic acid (RNA)). Sometimes CNTs are mixed with metal oxide semiconductor materials in order to improve their sensitivity [53].

Chapter 3

Pseudobrookite

Many MOS gas sensitive materials have been the subject of wide and excessive investigations such as SnO_2, TiO_2, ZnO, WO_3, Fe_2O_3, In_2O_3 etc. [2, 53, 49]. In this thesis, the focus will be on a new binary MOS gas sensitive material comprised of TiO_2 and Fe_2O_3, so called pseudobrookite (PSB) Fe_2TiO_5. Several investigations for Fe_2O_3–TiO_2 binary MOS gas sensitive materials toward oxygen [69], ethanol and oxygen [70] have been reported. Moreover there is an investigation of TiO_2-Fe_2O_3 binary MOS sensitive toward CO gas at 150 °C [71].

A systematic investigation of the $Fe_{1+x}Ti_xO_5$ system, using X-ray diffraction, Mössbauer spectroscopy and neutron diffraction has been reported [72]. The crystal structure of pseudobrookite MOS material is most commonly orthorhombic, containing four formula units per unit cell and belongs to the ${D_{2h}}^{17}$ ($Cmcm$) space group. Iron ions in Fe_2TiO_5 according to [72] appear to be Fe^{3+}. The site preference for these ions is 72% for 4c sites, indicating that 36% of the total Fe is in this site, with the remaining Fe^{3+} ions occupying 8f sites. Thus, two different octahedral cationic sites are present [73, 74]. The A - less distorted site (Wyckoff notation 4c, point symmetry mm) has three couples of metal-oxygen distances in the 1.91 Å to 2.15 Å range, with an average of 2.021 Å. The B site (Wyckoff notation 8f, point symmetry m) is more strongly distorted and has a mean metal-oxygen distance of about 2.01 Å [74]. The B octahedron has a larger polyhedral volume (10.17 Å^3 versus 9.98 Å^3) and they share edges to form trioctahedral units linked into infinite double chains along c. Their further sharing results in a three-dimensional framework. Orthorhombic Fe_2TiO_5 exhibits anisotropic spin glass behavior below 55 K [75].

The structure of monoclinic pseudobrookite (Fe_2TiO_5) was analyzed and determined as $C2/c$ containing slightly distorted TiO_6 and FeO_6 octahedra [76]. Defects in monoclinic Fe_2TiO_5 were studied in [77, 78, 79]. The monoclinic structure of Fe_2TiO_5 can be derived from a hexagonal close-packed structure and considered a member of the family of crystallographic structures derived from rutile and simi-

lar to V_3O_5. The $4a$ cations occupy relatively symmetric positions within oxygen octahedral, with metal-oxide distances between 2.00 Å and 2.03 Å. The $8f$ cation sites are very asymmetric with distances from 1.85 Å to 2.26 Å [78]. Stacking faults, antiphase boundaries and two different crystallographic planes are caused by two different slips corresponding to two hexagonal basal slips [77]. Analysis of Mössbauer spectra showed iron spins directed along the b axis [78]. Iron ions are distributed over crystallographic $4a$ and $8f$ sites, with $4a$ sites preferentially occupied by Fe^{3+} ions, and Fe^{3+} and Ti^{4+} ions randomly distributed over $8f$ sites [79].

Pseudobrookite is formed on hematite grains at temperatures above 800 °C through Ti^{4+} diffusion to the Fe_2O_3 surface forming a pseudobrookite layer around Fe_2O_3 particles [3]. The reaction progress is further controlled by solid-state diffusion through this layer [80]. The phase transformation of anatase to rutile occurs separately from pseudobrookite formation, with Fe presence enhancing the phase transformation [81]. The enhancement effect of hematite starts by diffusion of Fe^{3+} into anatase at the contact points between particles during heating. Iron can change valence during heating, undergoing a reaction creating an oxygen vacancy:

$$2\,Fe^{3+} + O^{2-} \rightarrow 2\,Fe^{2+} + \bigcirc_a + 1/2O_2 \tag{3.1}$$

where $\bigcirc_a$ denotes an anion vacancy.

The anatase to rutile transformation in the TiO_2 lattice will be promoted by the formation of oxygen vacancies due to the reduction of dopant iron:

$$Fe^{3+} + Ti^{4+} + 2\,O^{2-} \rightarrow (Fe^{2+} + \bigcirc_a + O^{2-}) + Ti^{3+}_{intersticial} + \frac{1}{2}O_2 \tag{3.2}$$

with the anion vacancy enhancing the phase transformation. The surface oxygen vacancies present due to Fe^{3+} dissolution migrate from the TiO_2 surface into the bulk, favoring rutile nucleation in both the surface and bulk of anatase particles. With increase in temperature, Fe^{3+} dissolution and diffusion increase promoting further nucleation and formation of rutile.

According to [76] the structure of monoclinic pseudobrookite is isostructural with V_3O_5 that is a member of the family of crystallographic shear structures derived from rutile. Monoclinic pseudobrookite transforms irreversibly into orthorhombic pseudobrookite at 1000 °C [79, 77]. The formation of monoclinic pseudobrookite in the temperature interval 750 °C- 950 °C in the presence of chlorine gas using starting hematite and TiO_2 (95 % anatase, 5 % rutile) in the molar ratio 1:1 was studied in [82]. Samples thermally treated at 750 °C and 850 °C for shorter durations consisted of both monoclinic and orthorhombic pseudobrookite, while longer heating times or higher thermal treatment temperatures resulted in the formation of only orthorhombic pseudobrookite.

So far, to the best knowledge of the author, no work has been reported dealing with pseudobrookite (Fe_2TiO_5) MOS as a gas sensitive material.

3.1 Material Characterization

3.1.1 Bulk Pseudobrookite

Chosen starting materials were hematite (Fe_2O_3, Alfa Aesar, 99%, grain size 20-60 nm) and anatase (TiO_2, Alfa Aesar, 99.7%, grain size 15 nm) in the form of nanopowders. The ideal molar ratio for pseudobrookite (Fe_2TiO_5) formation is 1:1 (hematite:anatase) [72]. For this research we wanted to try out mixing ratio 1:1.5 (hematite:anatase), with slight excess of anatase (TiO_2). Excess anatase was added to ensure no remaining hematite as available literature data [72] showed that this was often the case. The mixture was homogenized using a planetary ball mill (Fritsch Pulversisette 5) in stainless steel bowls with stainless steel balls for one hour. For the sake of simplicity, this nanopowder mixture will be referred to as PSB-1.5.

Density of Bulk Material

The obtained PSB-1.5 nanopowder mixture was placed in a mold and compressed with 2 GPa. Round shaped tablets 10 mm in diameter (d) and 2 mm thick (t) were fabricated and sintered in air in the temperature range 750 °C - 1250 °C for two hours. Overall dimensions and weights of all tablets were measured in a green (non-sintered) state and also after sintering, enabling calculation of the density of green and sintered specimens as:

$$\rho = \frac{m}{V} \tag{3.3}$$

where m is the sample mass and V is the sample volume calculated as:

$$V = td^2\frac{\phi}{4} \tag{3.4}$$

where t is the sample thickness and d is the sample diameter.

The change of specimen density with sintering temperature was experimentally determined (Figure 3.1). For green (non-sintered) specimens it was estimated that the average density is 2.59 g/cm^3. From Figure 3.1 it can be observed that the rapid change of specimen density occurs from 750 °C till 1050 °C and in particular the fastest change takes place from 2.78 g/cm^3 at 850 °C to 3.63 g/cm^3 at 950 °C.

If we analyze the XRD results (Figure 3.2), it can be seen that at 850 °C the pseudobrookite is formed and the anatase to rutile phase transformation was complete, giving us a possible explanation about the reason for such a behavior. After 1050 °C, the density will continue to increase with a significantly smaller rate reaching 4 g/cm^3 at 1250 °C.

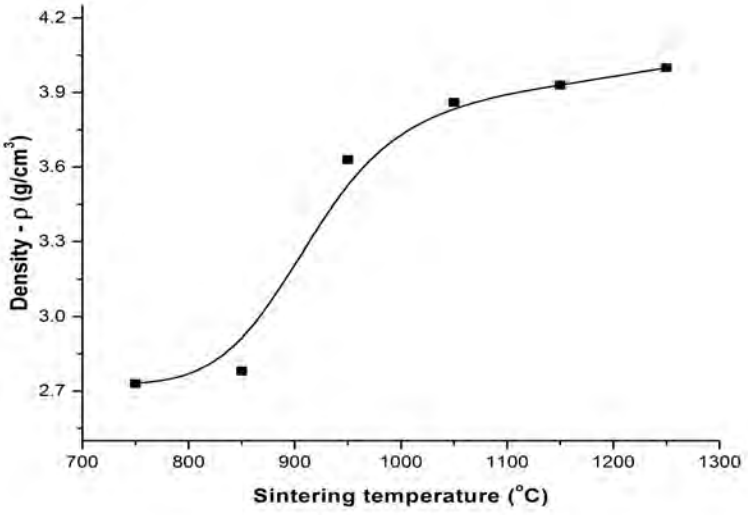

Figure 3.1: Change of sample density for PSB-1.5 material with the increase of the sintering temperature.

X-rax Powder Diffraction of Bulk Material

Sintered specimens have been analyzed with X-ray Powder Diffraction (XRD) on a RIGAKU RINT2000 diffractometer, CuKa$_\alpha$=1.54178 Å, and the results are presented in Figure 3.2.

Analysis of XRD diagrams of PSB-1.5 specimens sintered at 750 °C were composed of anatase (JCPDS 89-4921), rutile (JCPDS 89-4920) and hematite (JCPDS 89-8104) showing that the anatase to rutile phase transformation had started at this temperature, but was not complete as some anatase remained. Additionally, this temperature was too low for the onset of pseudobrookite formation. Specimens sintered at 850 °C contained rutile and pseudobrookite (JCPDS 76-1158) with an orthorhombic structure, showing that the anatase to rutile phase transformation was complete, most probably accelerated by the presence of Fe, while hematite and anatase had formed pseudobrookite. Specimens sintered at higher temperatures (850-1250 °C) also comprised of only orthorhombic pseudobrookite and rutile.

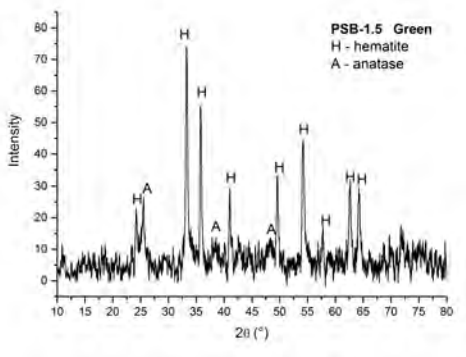

(a) Green

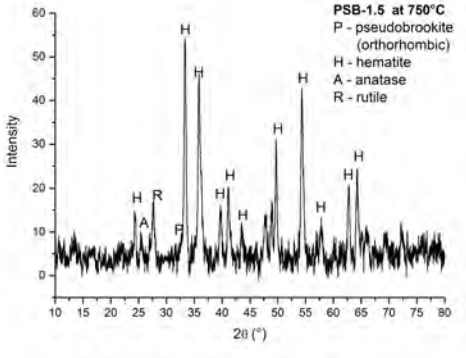

(b) 750 °C

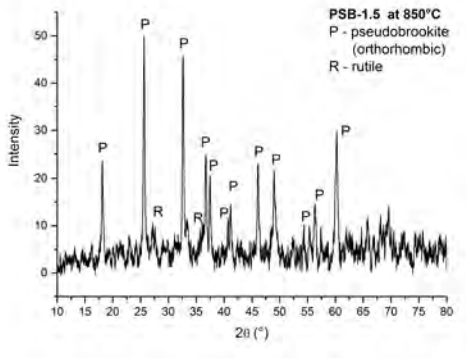

(c) 850 °C

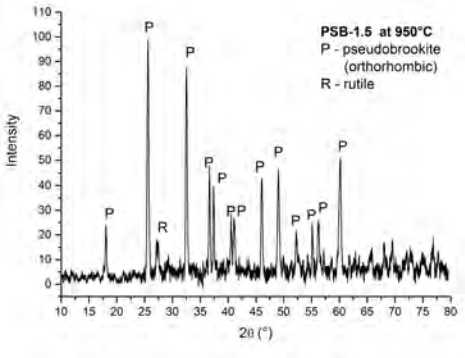

(d) 950 °C

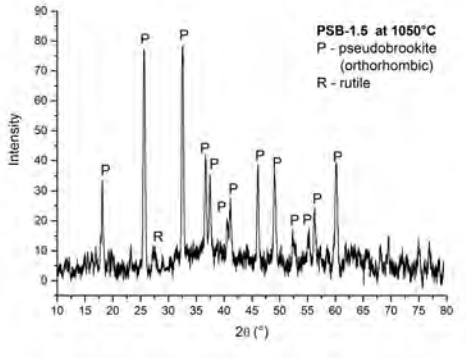

(e) 1050 °C

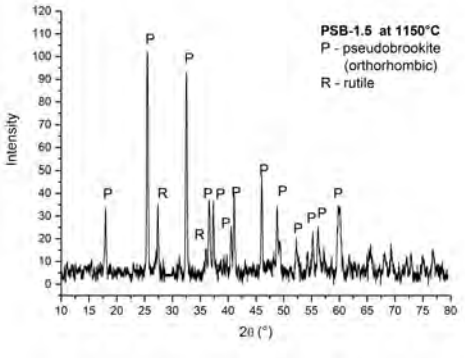

(f) 1150 °C

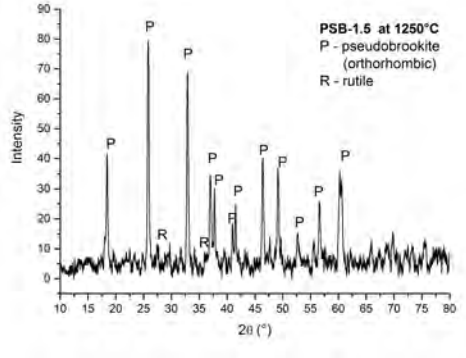

(g) 1250 °C

Figure 3.2: XRD patterns for the specimens sintered in region 750 °C - 1250 °C.

Scanning Electron Microscopy (SEM) and Energy-dispersive X-ray spectroscopy (EDS) of Bulk Material

Scanning Electron Microscopy (SEM) analysis was performed on a TESCAN Electron Microscope VEGA TS 5130MM device while Energy-dispersive X-ray spectroscopy (EDS) analysis was performed on an INCA Penta FETX3 energy dispersive system. Images were observed on freshly fractured specimens, meaning that specimens were broken and the cross-sections of the specimens were analyzed. SEM images for the specimens sintered in region 850 °C - 1250 °C are given in Figure 3.3.

Since the starting materials were nanopowders, for the specimen sintered at 850 °C (Figure 3.3 (a)), the grain size is small and the porosity is relatively high. At this stage it is simply too difficult to distinguish the presence of any of the phases. At 950 °C sintering has advanced and is in the intermediate stage, Figure 3.3 (b). A slightly lower porosity can be noted as well as grain growth. Furthermore, grains with slightly different sizes and shapes can be recognized, especially rod shaped grains characteristic for orthorhombic pseudobrookite. These rods are more noticeable in specimens sintered at temperatures of 1050 °C and above. Specimens sintered at 1050 °C (Figure 3.3 (c)) showed an inhomogeneous microstructure consisting of large and small grains with a relatively high density. At this sintering temperature rod shaped grains have grown rapidly and become much larger than the surrounding grains, as can be seen from Figures 3.3 (d). Further increase in the sintering temperature results in further agglomeration and grain growth; so the large rod shaped grains are slightly less noticeable, as the grains around them also grow rapidly as shown in Figure 3.3 (e) and Figure 3.3 (f) for specimens sintered at 1150 °C and 1250 °C.

Back scattering (BSE) imaging combined with EDS analysis of a sample sintered at 1150 °C (Figure 3.4) showed that the phase composition of the large rod shaped grains and most of the surrounding smaller ones is the same, corresponding to the Fe_2TiO_5 (PSB) phase composition. Slightly darker relatively large grains are rutile with small amounts of diffused Fe^{3+}. A few small grains with the phase composition $FeTi_2O_5$ were also noted.

A comparison of the difference between BSE and SEM of specimen sintered at 1250 °C (Figure 3.5) showed that it is comprised primarily of orthorhombic pseudobrookite (larger and smaller grains) and rutile (also large grains). The sintering process at this temperature was in the final stage.

As already noted, agglomeration was observed. It was taking place during the sintering process and became more visible with the increase of the sintering temperatures. Large macropores between the agglomerated particles can be distinguished as well as some pores between individual particles. Sintering is responsible for grain growth which can cause the microstructural heterogeneities in the mate-

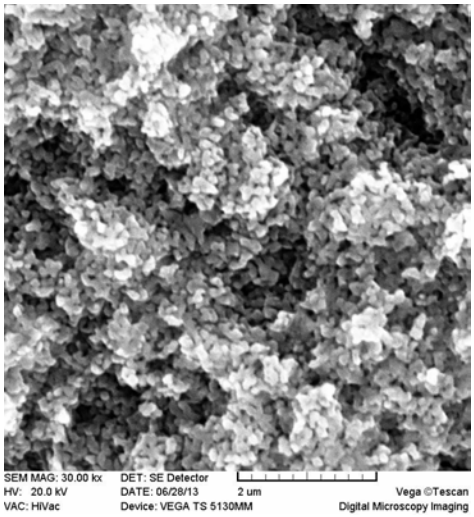

(a) 850 °C

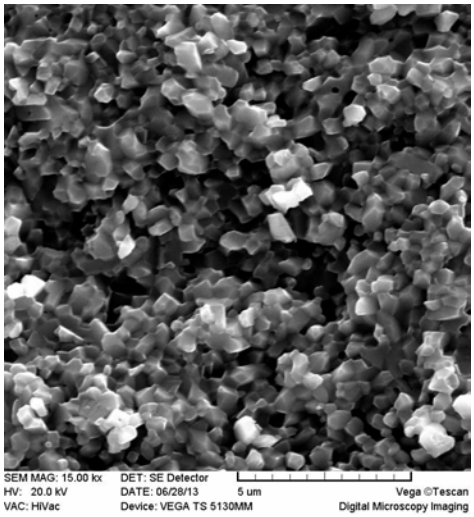

(b) 950 °C

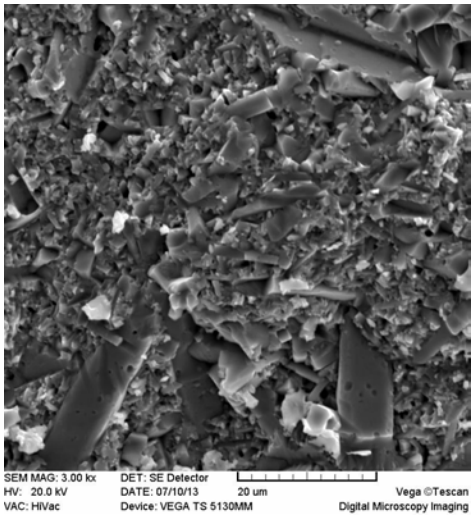

(c) 1050 °C

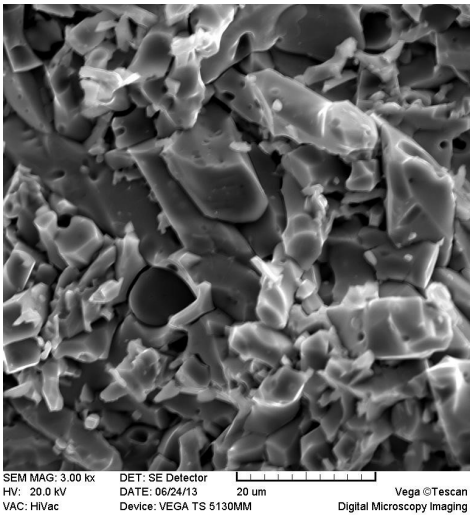

(d) 1150 °C

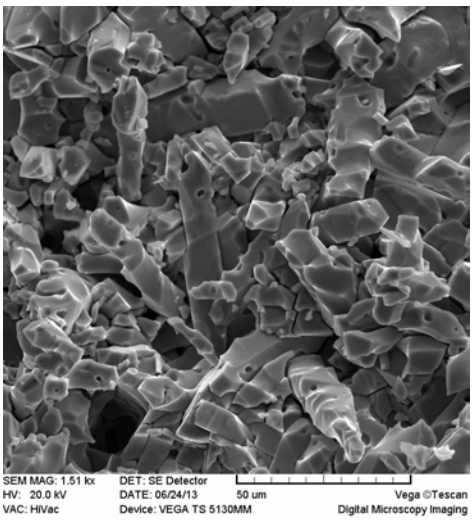

(e) 1250 °C

Figure 3.3: SEM images for the specimens sintered in region 850 °C - 1250 °C.

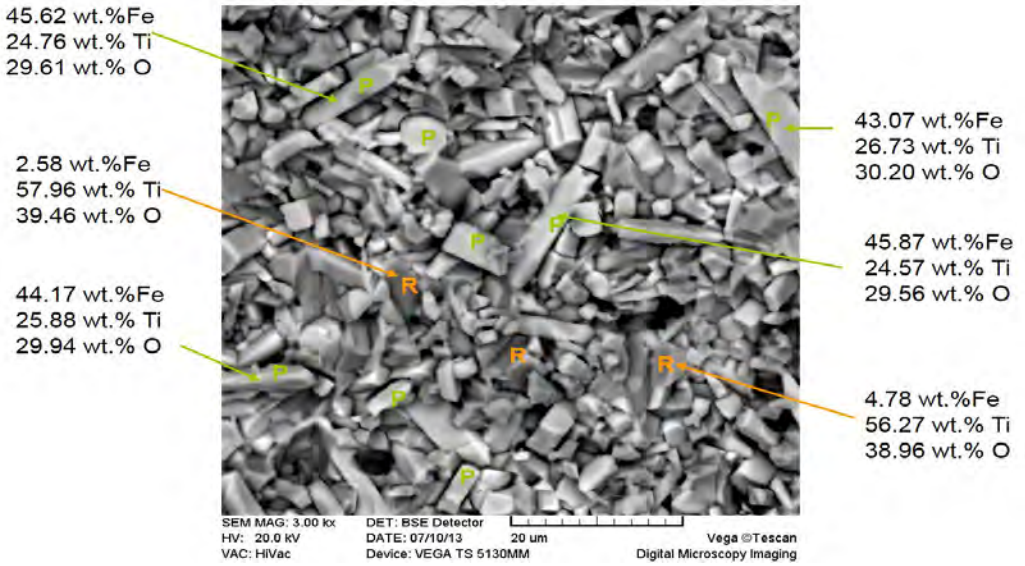

Figure 3.4: Back scattering (BSE) image and EDS analysis of a specimen sintered at 1150 °C.

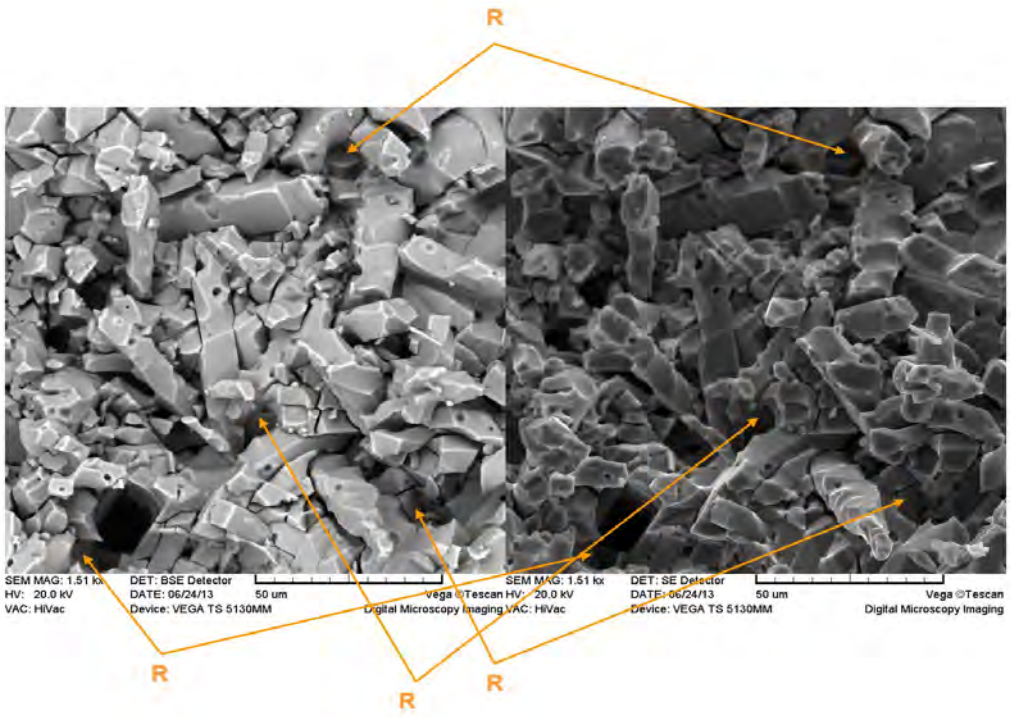

Figure 3.5: Back scattering (left) and SEM (right) images of a specimen sintered at 1250 °C.

rial. Some effects of the small grain size of the starting powder are in the much larger fraction of atoms localized at interfaces or close to them. It is interesting to observe how the increase of the sintering temperature, above 850 °C, is influencing the sample morphology when pseudobrookite has formed and the anatase to rutile phase transformation is complete according to XRD analysis.

Grain Size of Bulk Material

The average grain size was estimated from SEM images by averaging at least 100 grains on the analyzed SEM micrograph, while from XRD patterns, using the Sherrer equation, the average crystallite size was estimated (Table 3.1):

$$D = \frac{0.9\lambda}{\beta \cdot \cos\theta} \tag{3.5}$$

where λ is the X-ray wavelength, θ is the Bragg angle and β the pure full width of the diffraction line at half of the maximum intensity.

Table 3.1: Phase analysis, crystallite size and mean grain size.

Sintering temperature (°C)	Phases	Crystallite size D (nm)	Grain size (μm)
750	A+R+H	R-25, H-25	-
850	R+PSB	PSB-35	0.158 (sd 0.032)
950	R+PSB	PSB-36	0.54 (sd 0.19)
1000	R+PSB	PSB-36	0.88 (sd 0.31)
1050	R+PSB	PSB-36	Smaller grains 0.95 (sd 0.32) Larger grains Longer side 4.13 (sd 1.34) Shorter side 1.94 (sd 0.72)
1150	R+PSB	PSB-37	5.27 (sd 2.53)
1250	R+PSB	PSB-38	12.69 (sd 8.96)

A – anatase, R – rutile, H – hematite, PSB – pseudobrookite (orthorhombic), sd – standard deviation.

Electrical Resistance

For the purpose of electrical resistance measurements an electrode structure was screen printed on both sides of the sintered specimens using a silver paste (DuPont 4929N, dried 30 minutes at 150 °C). The prepared specimens had the form of

a capacitor, hence it was considered electrically equivalent to a capacitance C_p in parallel with a resistance R_p. Both values were measured using a HP-4194A impedance/gain-phase analyzer with a HP-16047A test fixture, at room temperature and 100 Hz. Electrical resistance was measured for all sintered specimens and it is given in Figure 3.6.

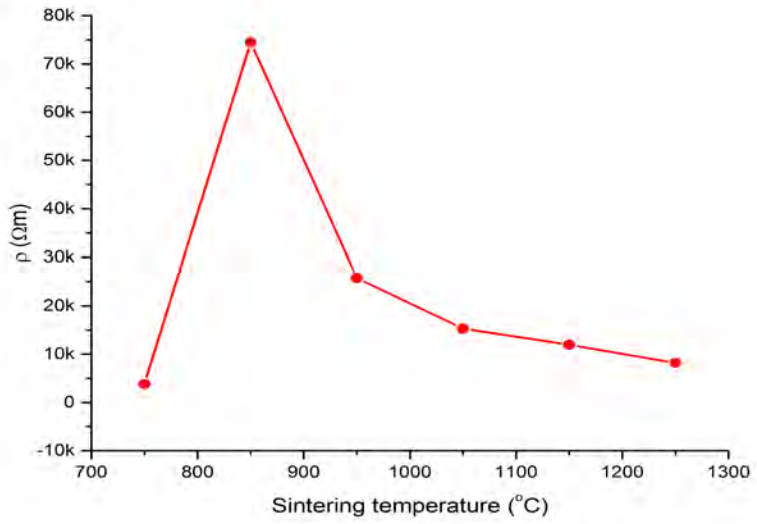

Figure 3.6: Electrical resistance at 100 Hz measured at room temperature depending on the sample sintering temperature.

As can be seen from Figure 3.6 the specimen sintered at 750 °C exhibited the lowest resistance, while the specimen sintered at 850 °C exhibited the highest one. This drastic difference between them could be possibly explained with different composition and morphology of the specimens. Namely the specimen sintered at 750 °C is comprised from anatase, rutile and hematite, while the specimen sintered at 850 °C is comprised from orthorhombic pseudobrookite and rutile. Another observation is that with the increase of the sintering temperature above 850 °C after formation of pseudobrookite and the phase transformation of anatase to rutile the electrical resistance decreases, which could be attributed to increase in sample density and change in sample morphology reflected in grain growth.

3.1.2 Pseudobrookite Thick Film

During the sintering process, the anatase to rutile phase transformation and formation of pseudobrookite are expected to occur. Temperatures at which the anatase to rutile phase transformation occurs are hard to be established since it is dependent on the characteristic of anatase. Depending on the characteristics of the

anatase powder, this transformation usually takes place in the temperature interval between 400 °C and 1000 °C [82]. It is possible to accelerate the transformation from anatase to rutile by adding dopants such as Fe. Formation of pseudobrookite occurs on hematite grains at temperatures higher than 800 °C through a solid–solid reaction in which Ti^{4+} diffuses to the Fe_2O_3 surface and forms a pseudobrookite layer around Fe_2O_3 particles [3, 80].

In subsection 3.1.1, investigation on bulk material obtained from a nanopowder mixture of anatase and hematite was made. From the XRD analysis of bulk PSB material it was concluded that starting at 850 °C pseudobrookite (orthorhombic) has formed and the anatase to rutile phase transformation is completed. Furthermore, from SEM analysis it was concluded that the material has high porosity when sintered at temperatures till 950 °C. In order to obtain thick film specimens with small grains and high porosity, as required for thick film gas sensors, pseudobrookite thick film specimens were analyzed in the temperature interval of 800 °C - 950 °C.

By mixing the previously obtained nanopowder mixture, an organic vehicle (butyl cellulose) and a small amount of binding lead boron silicone oxide glass frit, a thick film paste was obtained. The obtained paste was screen printed on alumina substrate and the specimens were sintered in a hybrid conveyor furnace in a temperature range 800 °C - 950 °C , with a 50 °C step, for 10 minutes (Figure 3.7).

Figure 3.7: Thick film sample obtained by screen printing thick film paste PSB-1.5 on alumina substrate after sintering.

X-ray Powder Diffraction of PSB Thick Film

Fabricated specimens were characterized by XRD analysis, performed on a Philips PW1050 diffactometer with CuK_αradiation, step 0.02 s and hold time 10 s, 2θ 10-110 °. Structural refinement was achieved by implementing the Rietveld method using the GSAS package [83] with the EXPGUI graphical user interface [84]. Specimens were analyzed for the presence of TiO_2 (rutile – space group $P4_2/mnm$ and

anatase – space group $I4_1/amd$), α-Fe_2O_3 and pseudobrookite (monoclinic and orthorhombic). Starting values for orthorhombic pseudobrookite (space group $Cmcm$) were taken from [85], while the starting values for monoclinic pseudobrookite (space group $C2/c$) were taken from [86]. Peaks from alumina substrate have been also taken into account and they can be seen in the obtained XRD patterns, Figure 3.8. They indicate that the thick film thickness is too low to be tested as a sensor. Therefore, further thick film specimens were realized by applying more layers during the screen printing process and XRD patterns of these films did not show any alumina peaks with the composition remaining the same.

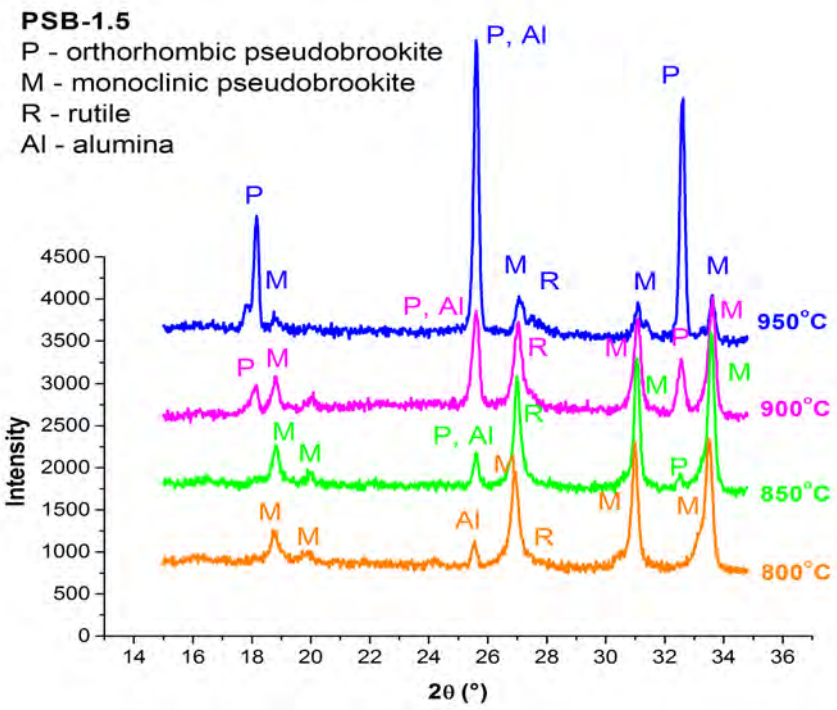

Figure 3.8: XRD patterns of PSB-1.5 thick film paste printed on alumina substrate after sintering in region 800 °C - 950 °C.

Analysis of XRD diagrams of PSB-1.5 specimens shows that for specimen sintered at 800 °C monoclinic pseudobrookite was the dominant phase, and also a small peak for rutile was noted. This showed that pseudobrookite formation had taken place, but monoclinic pseudobrookite had formed rather than orthorhombic. Also, excess anatase had transformed into rutile. At 850 °C still the small rutile peak is visible and still the monoclinic pseudobrookite phase remains the dominant one. However, small orthorhombic pseudobrookite peaks (023) and (110) can be noted at about 25.595 ° and 32.536 °, respectively. The peak (023) at 25.595 °, which is overlapping with the peak from alumina, is more perceptible than the peak (110) at 32.536 °. XRD patterns show that at 900 °C all three phases are clearly visible as the transformation from monoclinic into orthorhombic pseudobrookite has continued. At this temperature it was estimated that the weight ratio between monoclinic and orthorhombic pseudobrookite is 2.36:1. At 950 °C, most of monoclinic pseudobrookite has transformed into orthorhombic and the estimated weight ratio is 1:23.3 (monoclinic:orthorhombic).

From the XRD patterns (Figure 3.8) it was concluded that already at 800 °C monoclinic pseudobrookite is formed and the anatase to rutile phase transformation was completed. But what is most interesting is that compared to bulk specimens, where orthorhombic pseudobrookite formed, in the case of thick film specimens monoclinic pseudobrookite is the dominant phase. Since the same starting nanopowder composition was used in both cases, the possible explanation for this phenomenon could be attributed to the presence of the binder in thick film paste.

Scanning Electron Microscopy (SEM) of PSB Thick Films

SEM analysis was performed on a TESCAN Electron Microscope VEGA TS 5130 MM device. Specimens sintered at 800 °C were flaking indicating that the sintering temperature was apparently too low to give a good quality thick film sample, so we did not analyze it further. Specimens sintered at 850 °C showed the most homogeneous structure (Figure 3.9 (b)), while rod-shaped grains started to be noticeable at 900 °C (Figure 3.9 (c)). At 950 °C sintering is in its final stage, closed porosity is noticeable and grain size has increased (Figure 3.9 (d)). The thickness of the analyzed specimens was between 55 μm (initial specimens) and 80 μm (later specimens) was achieved by screen printing several layers. Higher film thickness enabled obtaining specimens where XRD analysis did not show any peaks originating from alumina. The cross section of one of the specimens sintered at 850 °C is given in Figure 3.10, where the thickness of the specimen was around 80 μm.

Since the specimens sintered at 800 °C showed a weak mechanical stability, they have not been considered for further investigation. By contrast, specimens sintered at 850 °C had great mechanical stability and at the same time this temperature was the lowest temperature where, according to XRD patterns, two different phases of pseudobrookite (monoclinic and orthorhombic) existed. Moreover, analyses of SEM imaging showed that at 850 °C the porosity of the thick film specimens was still relatively high and the grains were still small, hence this temperature has been selected as the optimal sintering temperature.

The fact that thick films are much more porous than bulk specimens could also contribute to the formation of the more defective monoclinic pseudobrookite structure (in case of the thick films). As already mentioned, the possible explanation for formation of monoclinic pseudobrookite structure could be attributed to the presence of the binder in thick film paste.

Crystallite Size and Lattice Parameters of PSB Thick Film

Structural refinement of XRD diffractograms using the Rietveld method enabled determination of the lattice parameters and average crystallite size and they are given in Table 3.2 and Table 3.3, respectively. These parameters have been determined for orthorhombic pseudobrookite only for specimens where the peak was big enough (orthorhombic pseudobrookite content high enough) to enable calculation.

It was determined that the estimated crystallite size of monoclinic pseudobrookite is bigger than the estimated crystallite size of orthorhombic pseudobrookite as shown in Table 3.3. As expected, with increase in the sintering temperature, the crystallite size increases corresponding to the grain growth which is also triggered by increase of the sintering temperature.

Table 3.2: Lattice parameters for PSB-1.5 thick film specimens sintered in region 850 °C - 950 °C.

	Sintering temperature °C			
Phases	800	850	900	950
PM	a= 10.133(17)	a= 10.119(12)	a= 10.116(2)	a= 10.131(4)
	b= 5.0345(7)	b= 5.0298(6)	b= 5.0276(10)	b= 5.024(2)
	c= 7.0374(10)	c= 7.0271(8)	c= 7.0264(12)	c= 7.022(2)
PO			a= 3.7365(6)	a= 3.1718(4)
			b= 9.803(3)	b=9.766(2)
			c= 9.985(2)	c=9.955(2)

PM – Monoclinic pseudobrookite, PO - Orthorhombic pseudobrookite.

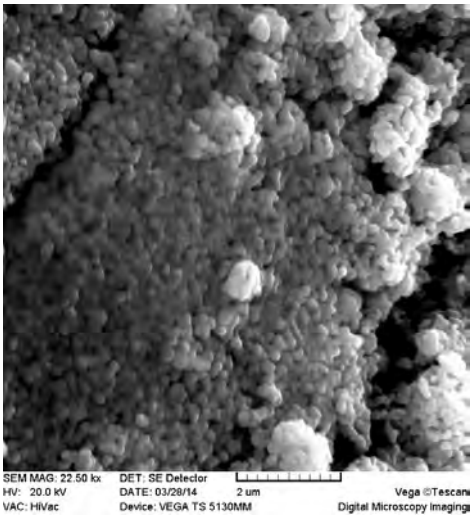

(a) 850 °C

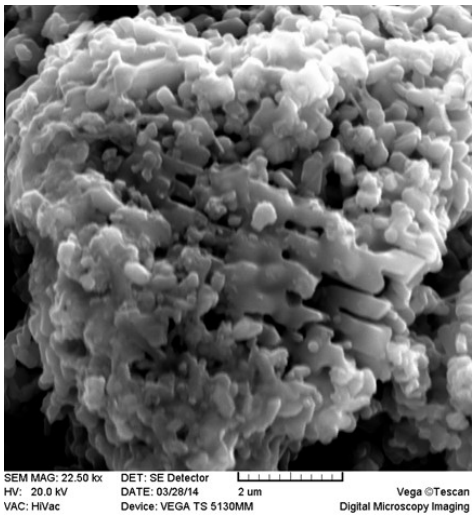

(b) 900 °C

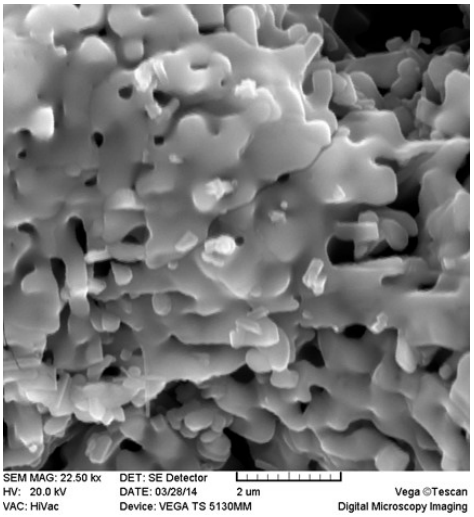

(c) 950 °C

Figure 3.9: SEM images of the thick film specimens screen printed on alumina substrate sintered in region 850 °C - 950 °C.

Comparison of PSB-1 and PSB-1.5 PSB Thick Film

As already mentioned, the ideal molar ratio for pseudobrookite (Fe_2TiO_5) formation is 1:1 (hematite:anatase) [72]. In order to compare the ideal molar ratio (1:1) with 1:1.5 molar ratio, nanopowder mixture with molar ratio (1:1) was made. Starting from hematite (Fe_2O_3, Alfa Aesar, 99%, grain size 20-60 nm) and anatase (TiO_2, Alfa Aesar, 99.7%, grain size 15 nm) in a form of nanopowders. The mixture was homogenized using a planetary ball mill (Fritsch Pulversisette 5) in stainless

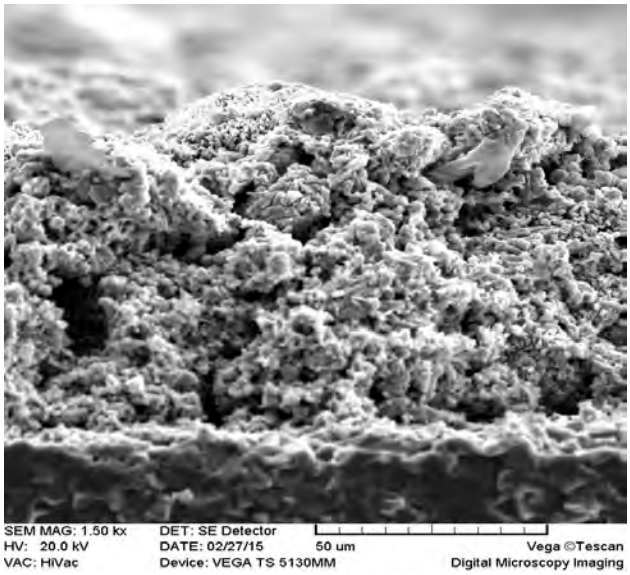

Figure 3.10: SEM image of cross section of PSB-1.5 thick film paste sintered at 850 °C.

Table 3.3: Crystallite size for PSB-1.5 thick film specimens sintered in region 850 °C - 950 °C.

	Sintering temperature °C			
Phases	800	850	900	950
PM	43.2 nm	80.6 nm	164.7 nm	194.8 nm
PO				167.1 nm

PM – Monoclinic pseudobrookite, PO - Orthorhombic pseudobrookite.

steel bowls with stainless steel balls for one hour. This nanopowder mixture will be referred to as PSB-1. From the obtained mixture a thick film paste was prepared using the same preparation technique described at the beginning of this subsection.

Further analysis will involve a comparison between PSB-1.5 and PSB-1 thick film specimens sintered in a hybrid conveyor furnace at 850 °C, for 10 minutes. These PSB films were screen printed in several layers to obtain slightly thicker thin films, around 80 μm.

X-ray powder diffraction (XRD) analysis are given in Figure 3.11 and from them it can be observed that PSB-1.5 is a mixture of orthorhombic (a=3.7461(3), b=9.805(2), c=9.9882(18)), monoclinic pseudobrookite (a=10.1076(4), b=5.0323(8), c=7.0528(10)) and a small amount of rutile (TiO_2), while PSB-1 has a pure or-

thorhombic pseudobrookite morphology (a=3.7625(3), b=9.98029(16), c=9.9885(13)), Table 3.4. No alumina peaks originating from the substrate were noted on the XRD patterns.

The average crystallite size was determined using the Sherrer equation (equation 3.5). It was 41 nm for orthorhombic pseudobrookite in PSB-1 and 43 nm for orthorhombic and 41 nm for monoclinic pseudobrookite in PSB-1.5, respectively.

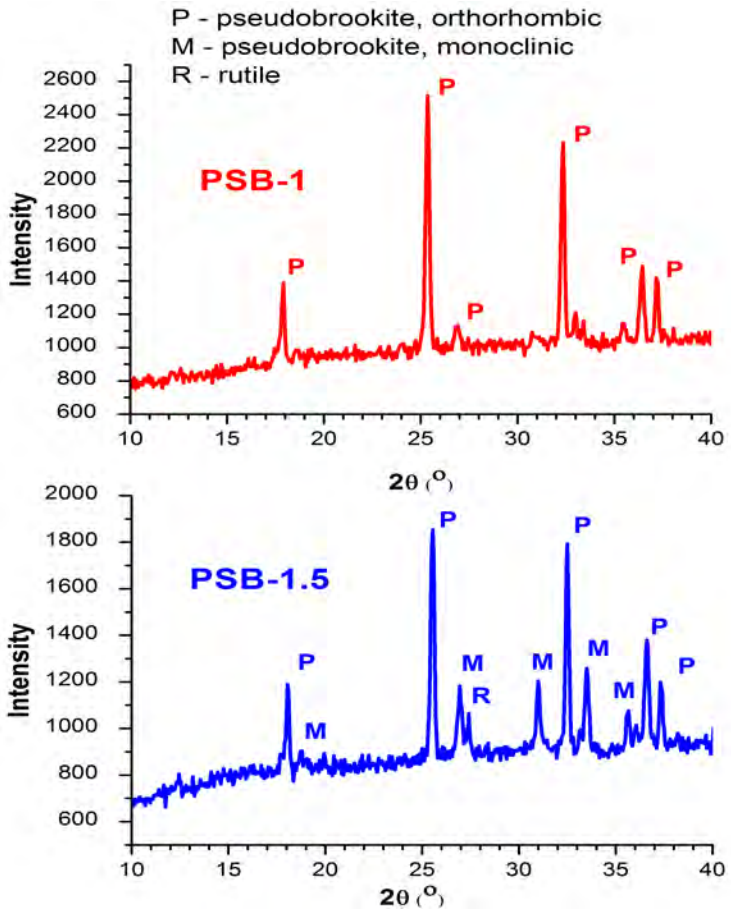

Figure 3.11: XRD patterns for PSB-1.5 and PSB-1 thick film pastes printed on alumina substrate sintered at 850 °C.

Scanning Electron Microscope (SEM) micrographs of PSB-1 and PSB-1.5 specimens are shown in Figure 3.12. PSB-1 has a slightly larger grain size than PSB-1.5 that contains a small amount of excess TiO_2.

Table 3.4: Phases, lattice parameters and crystallite size for PSB-1.5 and PSB-1 thick film specimens sintered at 850 °C.

	PSB-1.5	PSB-1
Phases	PO PM	PO
Lattice parameters	Orthorhombic a=3.7461(3) b=9.805(2) c=9.9882(18) Monoclinic a=10.1076(4) b=5.0323(8) c=7.0528(10)	Orthorhombic a=3.7625(3) b=9.98029(16) c=9.9885(13)
Crystallite size	Orthorhombic 43 nm Monoclinic 41 nm	Orthorhombic 41 nm

PM - Monoclinic pseudobrookite, PO - Orthorhombic pseudobrookite .

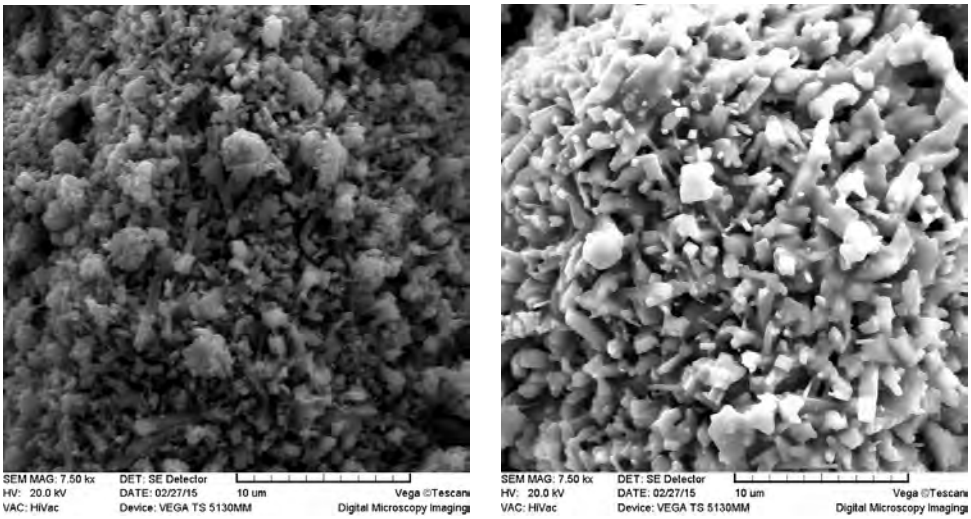

(a) PSB-1.5 (b) PSB-1

Figure 3.12: SEM images of PSB-1.5 and PSB-1 thick film paste sintered at 850 °C.

Electrical Resistivity. For this purpose test matrices with AgPd interdigitated (ID) electrodes were printed on alumina substrate, on top of which PSB-1.5 and PSB-1 have been screen printed, Figure 3.13. The interdigitated electrode spacing (s) was 0.2 mm and 0.25 mm, while the thickness of the PSB thick film layer was around 80 μm. Specimens have been sintered at 850 °C for 10 minutes.

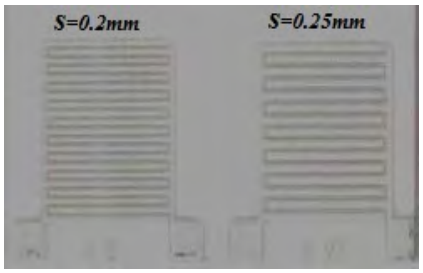

(a) ID electrodes

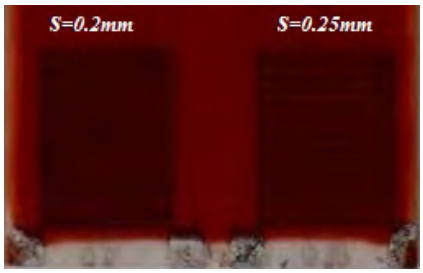

(b) PSB material on top of ID electrodes

Figure 3.13: Test matrices for electrical characterization of PSB-1.5 and PSB-1 thick film paste sintered at 850 °C.

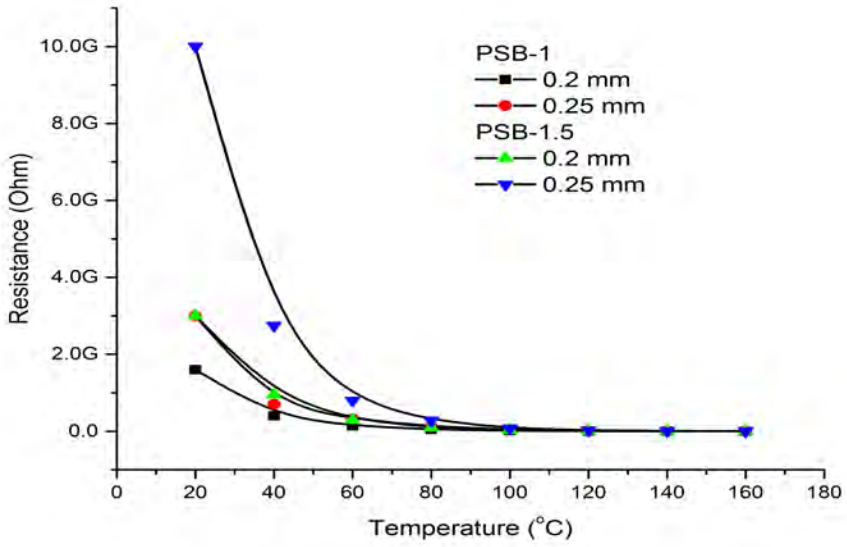

Figure 3.14: Change of resistance for PSB-1 and PSB-1.5 thick film test specimens with temperature, linear scale.

The change of resistance for PSB-1 and PSB-1.5 interdigitated thick film test specimens with temperature has been measured with a HP.4329a high-resistance meter with 50 V DC. Results are shown in Figure 3.14 and 3.15. As could be seen from the figures, PSB-1.5 specimens are showing higher resistance values than the PSB-1 specimens. Another observation is that in the both cases, specimens with 0.25 mm electrode spacing are showing significantly higher resistance, compared to the ones with 0.2 mm electrode spacing. For both types of PSB an exponential decrease in the resistance with increase in temperature can be noted, classifying them as materials with negative temperature coefficient (NTC). The B-value (material constant) can be determined from the slope of the $lnR - 1000/T$ (in Kelvin) characteristic over the specified temperature range. In the case of PSB-1 it is 6335, while for PSB-1.5 it is 7182.

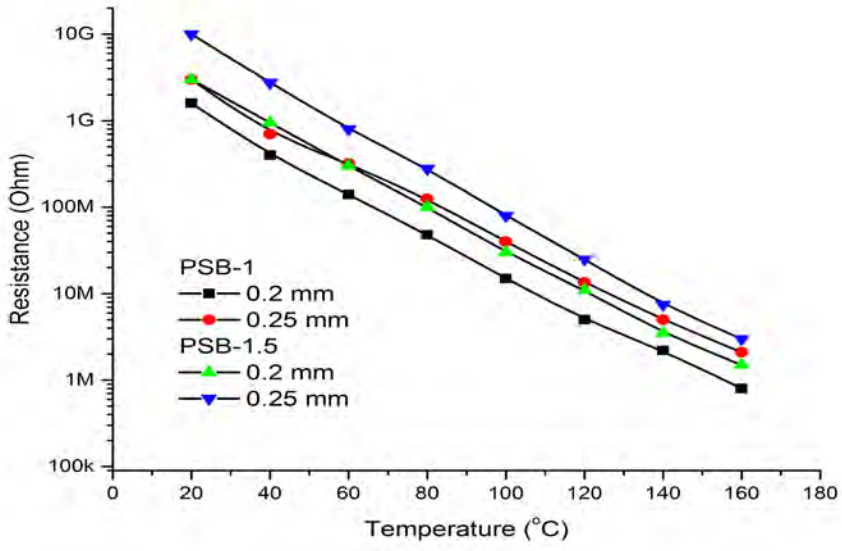

Figure 3.15: Change of resistance for PSB-1 and PSB-1.5 thick film test specimens with temperature, logarithmic scale.

Diffuse reflectance spectra were measured on a UV/Vis Shimadzu UV-2600 with an ISR2600Plus integrating sphere attachment in the measuring range 220 nm - 1000 nm. Measured diffuse reflectance spectra of PSB-1 and PSB-1.5 specimens are shown in Figure 3.16. The acquired spectra were converted using the UV-Probe software to the Kubelka-Munk function $F(R_\infty)$ proportional to the absorption coefficient. The optical band gaps were estimated using Tauc plots and the relationship of Mott and Davies:

$$h\varphi \cdot F(R_\infty) = A(h\varphi - E_g)^m \tag{3.6}$$

where $h\varphi$ is the absorbed photon energy, A is and constant related to the density of electronic states above and below the band gap, E_g is the optical band gap where m=1/2 is direct allowed transition and m=2 is indirect allowed transition. For direct band gap semiconductors, electronic transition from the valence band to the conduction band is allowed and thus the electrical absorption and emission are usually strong in this case. In the case of indirect band gap semiconductors the electronic transition from the valence band to the conduction band is possible only with the assistance of additional energy, such as photon or phonon and in this case the electrical absorption and emission are weaker [87].

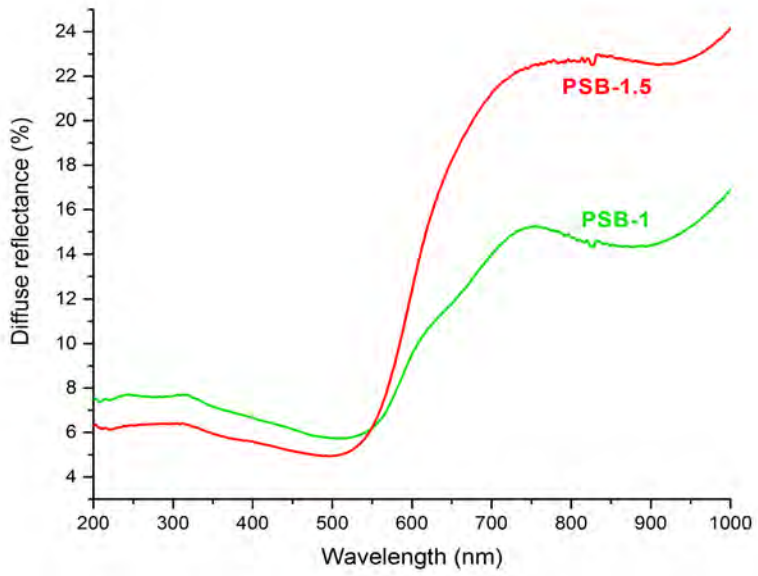

Figure 3.16: Diffuse reflectance spectra for PSB-1.5 and PSB-1 thick film pastes printed on alumina substrate sintered at 850 °C.

The values determined from the Tauc plots for PSB-1 were 2.05 eV direct band gap, 1.63 eV indirect and for PSB-1.5 2.09 eV direct band gap, 1.77 eV indirect. The values obtained for direct allowed transitions are pretty much similar to the band gap value of pure orthorhombic Fe_2TiO_5 of 2.18eV [4].

From the diffuse reflectance, differential reflectance ($dR/d\lambda$) was calculated as a function of the energy wavelength (λ) (Figures 3.17 and 3.18). From the

differential reflectance, presence of additional transition energies was possible to be determined and in addition to confirm the results obtained from the Tauc plot analysis. In Figures 3.17 and 3.18, the most prominent peaks are depicting the overall band gap energy and the accompanying lower peaks are representative of the additional transitions energies within the band gap [88, 89]. As can be seen, both material compositions have two transition energies, direct and indirect ones. Another observation is that PSB-1 has two distinguished separate peaks while PSB-1.5 has only one notable peak, showing a difference in the contribution of transition energies. The difference in the peaks and transition energies could again be contributed to the fact that the PSB-1.5 specimen is comprised of orthorhombic and monoclinic pseudobrookite phases, while the PSB-1 specimen contains only the orthorhombic pseudobrookite phase.

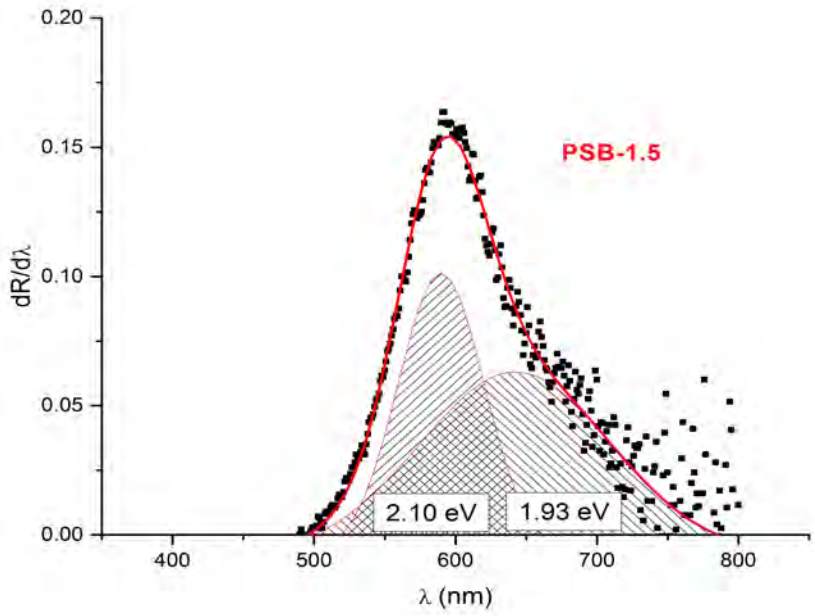

Figure 3.17: Differential reflectance as a function of the energy wavelength for PSB-1.5 thick film paste sintered at 850 °C.

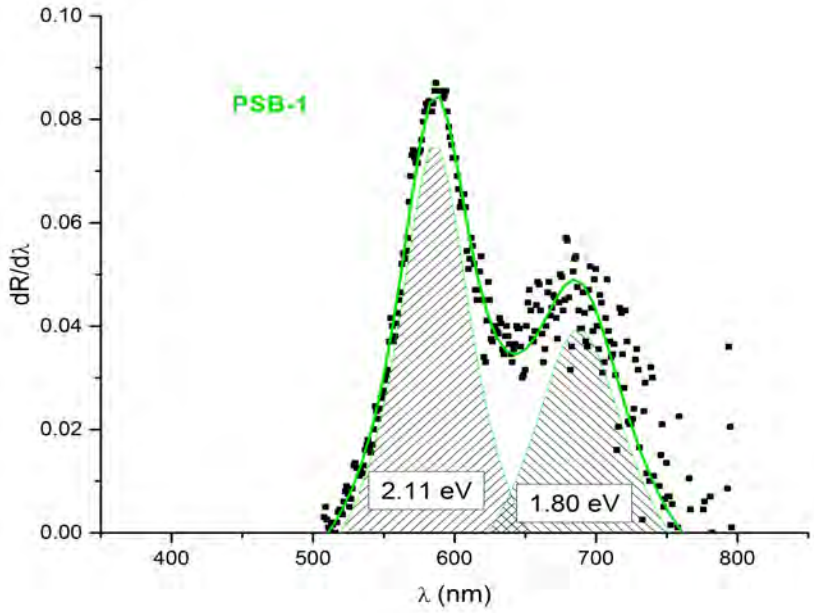

Figure 3.18: Differential reflectance as a function of the energy wavelength for PSB-1 thick film paste sintered at 850 °C.

Chapter 4

Sensor Characterization

From the results given in chapter 3 the conclusion was drawn that the resistance value of the testing specimens was too high for low voltage measurements so redesign of the specimens needed to be done. The basic design of the testing specimens was kept the same as the one used in chapter 3, but miniaturization was performed regarding the electrode dimension and the overall size of the specimens in order to achieve lower electrical resistance of the specimens.

For the purpose of characterizing the PSB materials with respect to NO gas sensitivity, test specimens were needed to be fabricated. Dual matrices with an interdigitated electrode structure were realized on alumina substrate (Al_2O_3). The interdigitated (ID) electrodes were made from PdAg paste, which were screen printed on the alumina. On top of the ID electrodes, PSB thick film pastes were deposited, again using print screen technique, and sintered in a hybrid conveyor furnace at 850 °C for 10 minutes in air. In total four layers of PSB were deposited; a drying process was applied after each layer deposition. The appearance of the fabricated specimens is given in Figures 4.1, while the overall dimensions are presented in Figure 4.2. Interdigitated electrode width (w) and spacing (s) were 0.2 mm, respectively, while the length of the finger (l) was 2 mm and the electrode had 10 fingers (n). The thickness of pseudobrookite thick films was 80 μm. Outer sample dimensions were 6 mm in width (m) and 12 mm in length (p).

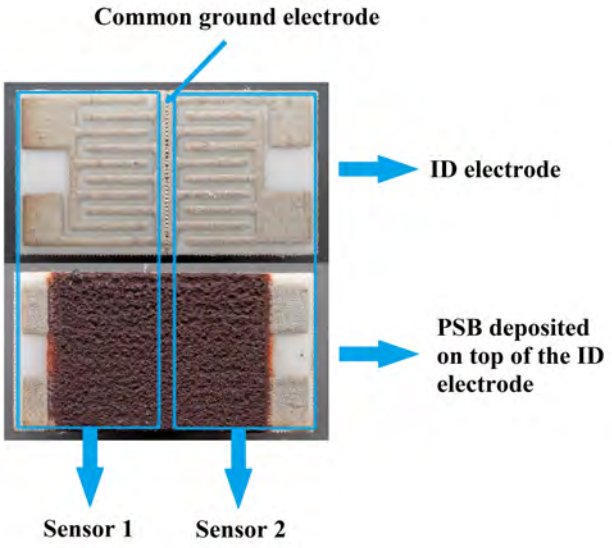

(a) ID (AgPd) electrode and PSB deposited on top of the ID electrode

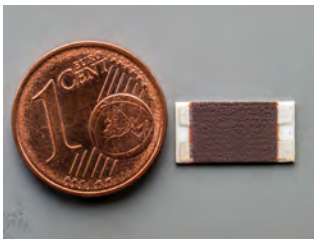

(b) comparison with one euro cent

Figure 4.1: Appearance of fabricated dual test specimens.

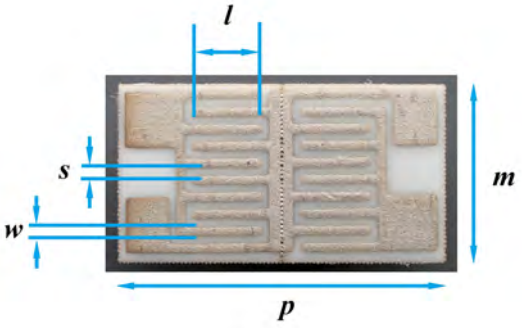

s	0.2 mm
w	0.2 mm
l	2 mm
p	12 mm
m	6 mm
n	10

Figure 4.2: Interdigitated electrode (ID) with marked geometries.

4.1 Electrical Characterization

Electrode Effect on Sheet Resistance of PSB

Interdigitated geometry consists of two complementary comb PgAg electrodes printed on alumina substrate (Figure 4.2), while the PSB MOS layer was printed on electrodes as a top layer (Figure 4.1 (a)). The effect of electrode is inherent for all thick films. Migration of conductor material to the MOS depends on the materials selection, their microstructure and sintering temperature or sintering profile. The effect of electrode on electrical resistivity ρ is given in Figure 4.3.

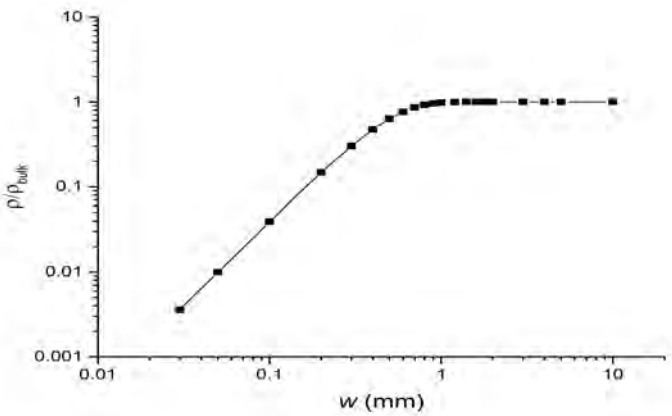

Figure 4.3: Electrode effect on electrical resistivity ρ of MOS resistive layer.

The resistance of an interdigitated resistor depends on electrical resistivity ρ of the MOS layer and geometry values of electrodes. An ideal model for resistance of an interdigitated geometry is given by the following equation:

$$R = \rho \frac{s}{2lnt} \tag{4.1}$$

where ρ is the electrical resistivity (specific electrical resistance) of the MOS material, s is the spacing between electrodes, n is the number of fingers, t is the thickness of the MOS film and l is the finger length.

The electrical resistivity ρ is constant only for large electrode spacing, much higher than critical distance (w_0), for example $w \gg 0$, $\rho = \rho_{bulk}$. For the distances smaller than w_0 the electrical resistivity decreases rapidly (exponentially) and it can be modeled as:

$$\rho = \rho_{bulk}(1 - e^{-(\frac{w}{w_0})^2}) \tag{4.2}$$

In the case of the critical distance for electrode, spacing is defined as $w = w_0$ and $\rho = \rho_{bulk}(1-1/e)$. The equation 4.2 takes into account the so called "electrode

effect" caused by diffusion of the PdAg electrode layer into MOS layer during the sintering process. The critical distance w_0 can be obtained from the experimental behavior $\rho(w)$ and in practice these values are around 0.5 mm (Figure 4.3). By joining the equations 4.1 and 4.2 the resistance R can be given as:

$$R = \rho_{bulk}(1 - e^{-}(\frac{w}{w_0})^2)\frac{s}{2lnt} \tag{4.3}$$

4.1.1 Impedance Measurements

Measurements of the impedance $Z = R + jX$ of PSB-1.5 and PSB-1 thick film specimens were performed on a HP4194 impedance analyzer in air at temperatures 50 °C - 300 °C (in steps of 50 °C). The resistance as a function of frequency is given in Figures 4.4 and 4.5, while reactance as a function of the resistance is given in Figures 4.6 and 4.7. The analyzed specimens were heated with a hot plate.

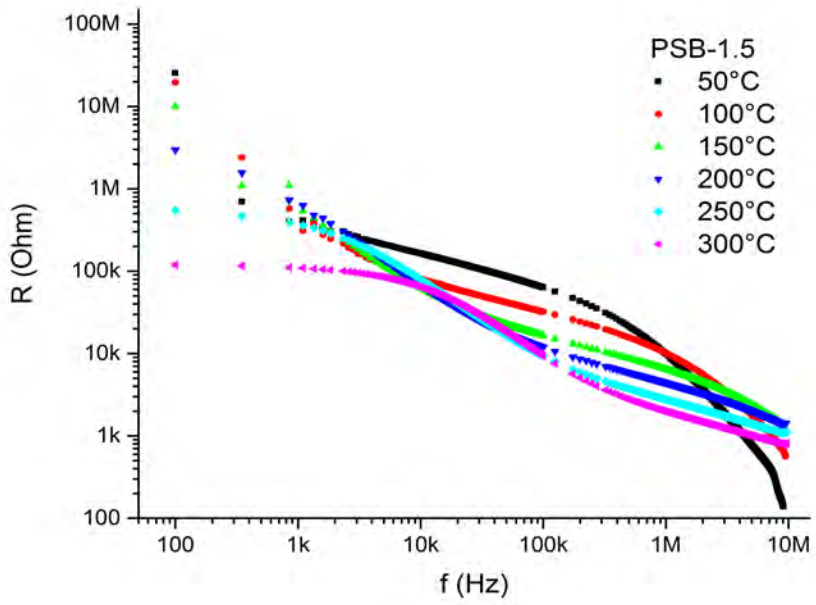

Figure 4.4: Resistance as a function of frequency at temperatures from 50 °C to 300 °C for PSB-1.5.

As it can be seen from the Figures 4.4 and 4.5, higher resistance values were obtained for PSB-1.5, compared to PSB-1. The differences in resistance could be attributed to different morphology of the materials. Analysis of the obtained results showed that for both materials the electrical resistance was high at lower

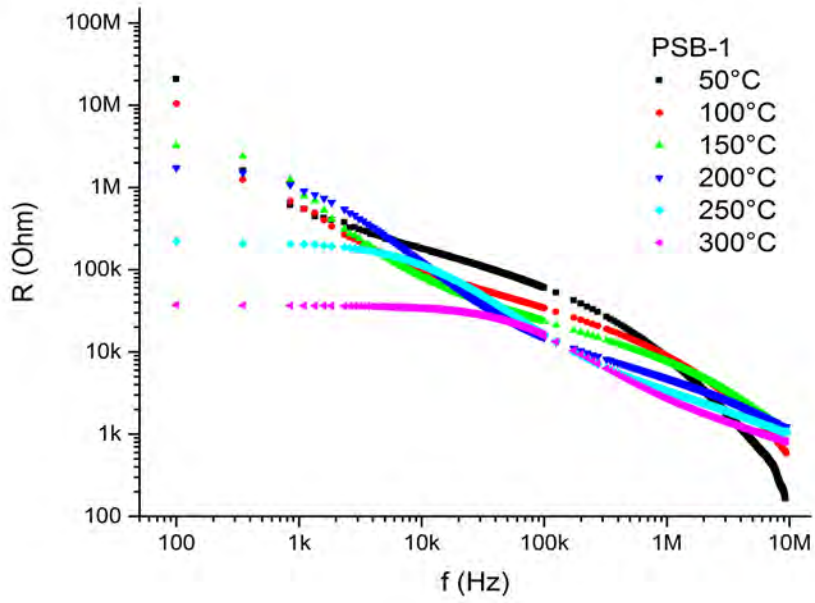

Figure 4.5: Resistance as a function of frequency at temperatures from 50 °C to 300 °C for PSB-1.

frequencies and with the increase of frequency, the resistance decreased. The electrical resistance also decreased with increase of the temperature; the lowest values are obtained for the sample heated to 300 °C.

For both materials (Figure 4.6 and Figure 4.7), the impedance values were high and the shape of the resistance-reactance curve at low frequencies at 50 °C and to some extent at 100 °C was almost linear. Starting from 150 °C this effect was less noticeable. In case of PSB-1.5, at 250 °C the resistance-reactance curve is almost semicircular, while at 300 °C the curve is semicircular. Compared to PSB-1.5, the values of resistance-reactance curve of PSB-1 are lower than the values of PSB-1 and as it can be noted from the Figure 4.6 and Figure 4.7, the resistance-reactance curve of PSB-1 is semicircular already at 250 °C. As expected, the resistance-reactance curve of PSB-1 at 300 °C is also semicircular.

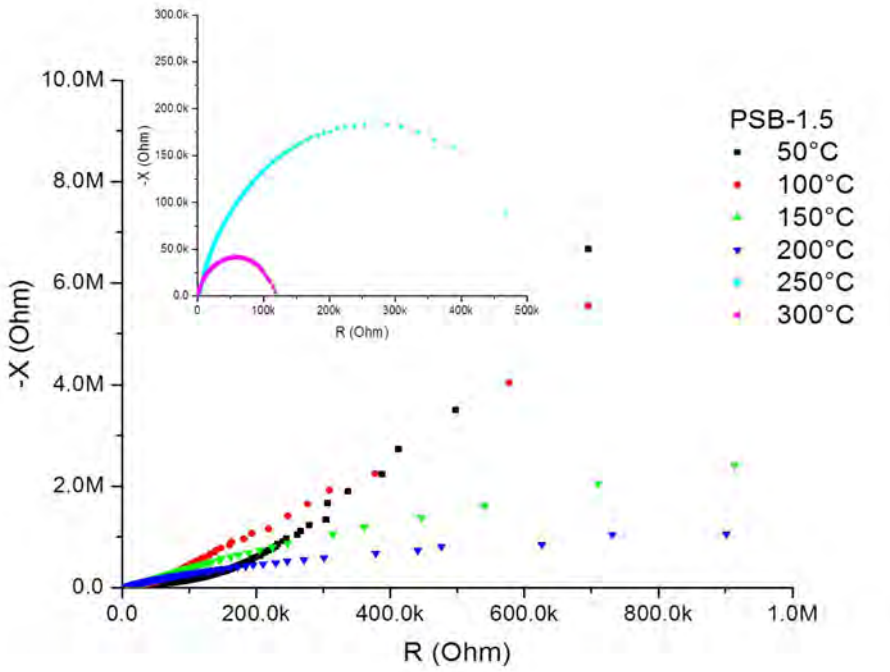

Figure 4.6: Reactance as a function of resistance at temperatures 50 °C - 300 °C for PSB-1.5.

The measured impedance of thick film oxide specimens is usually analyzed using an equivalent circuit composed of a resistance (R_{gb}) and a capacitance (C_{gb}) connected in parallel [90]. This equivalent circuit reflects the electrical properties of barriers at grain boundaries. A constant phase element (CPE) was used to replace the parallel capacitor in the RC equivalent circuit. It is applied in the cases when impedance semicircles are depressed with a center below the real axis [91]. CPE enables taking into account phenomena occurring in interface regions associated with inhomogeneity and diffusion processes [92]. The impedance of a CPE element is given as following:

$$Z_{CPE} = E^{-1}(j\omega)^{-g} \tag{4.4}$$

where ω is the angular frequency, E and g ($0 \leq g \leq 1$) are fitted parameters. When $g = 1$, the CPE described an ideal capacitor with $E = C$, when $g = 0$ the CPE describes an ideal resistor with $E = 1/R$. The (true) value of capacitance can be determined as [93]:

$$C_{CPE} = (ER^{-(g-1)})^{\frac{1}{g}} \tag{4.5}$$

where R is the determined resistance.

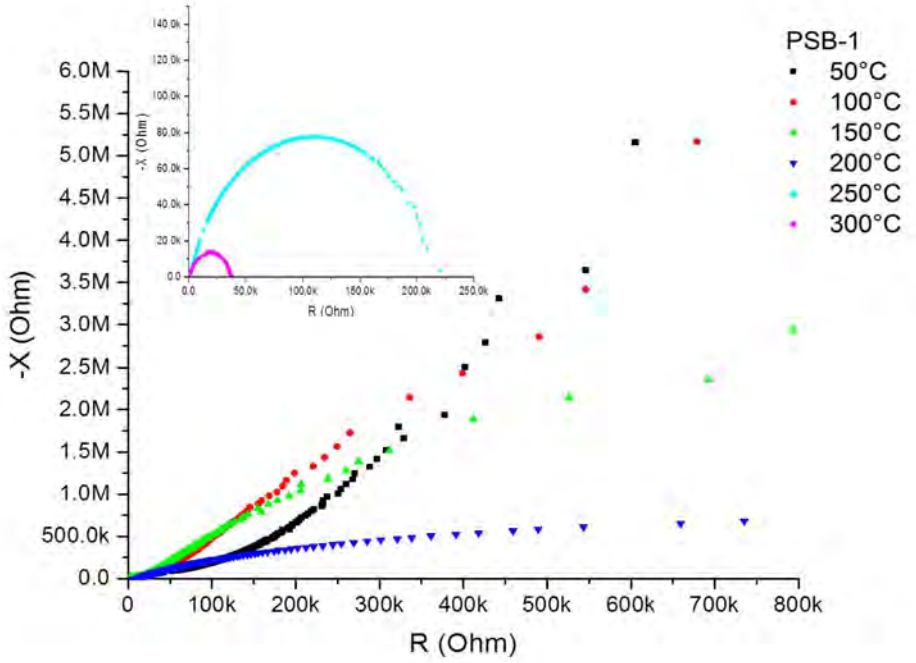

Figure 4.7: Reactance as a function of resistance at temperatures 50 °C - 300 °C for PSB-1.

The impedances of PSB-1.5 and PSB-1 thick film specimens measured in the temperature range between 150 and 300 °C were analyzed using the equivalent circuit shown in Figure 4.8, where R_{gb} and CPE_{gb} represent the grain boundary resistance and constant phase element, respectively. The measurements made at 50 °C and 100 °C were excluded from analysis as the obtained impedance values increased rapidly and could not be modeled using the applied simple equivalent circuit.

Other possible influences such as the electrode effect and bulk component were low enough not to be taken into account. Analysis and simulation of impedance spectra was performed using Electrochemical Impedance Spectroscopy (EIS) spectrum analyzer software [94], by using the equations 4.4 and 4.5. The examples of fitted experimental values are given in Figures 4.9 and 4.10. The values for resistance, g, capacitance and relaxation frequency determined for the grain boundary component are given in Table 4.1.

The temperature dependence of the determined grain boundary resistance can be analyzed using the adiabatic small polaron hopping (SPH) model [91],

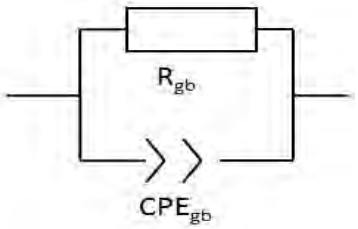

Figure 4.8: Equivalent circuit employed to fit PSB-1 and PSB-1.5 impedance data.

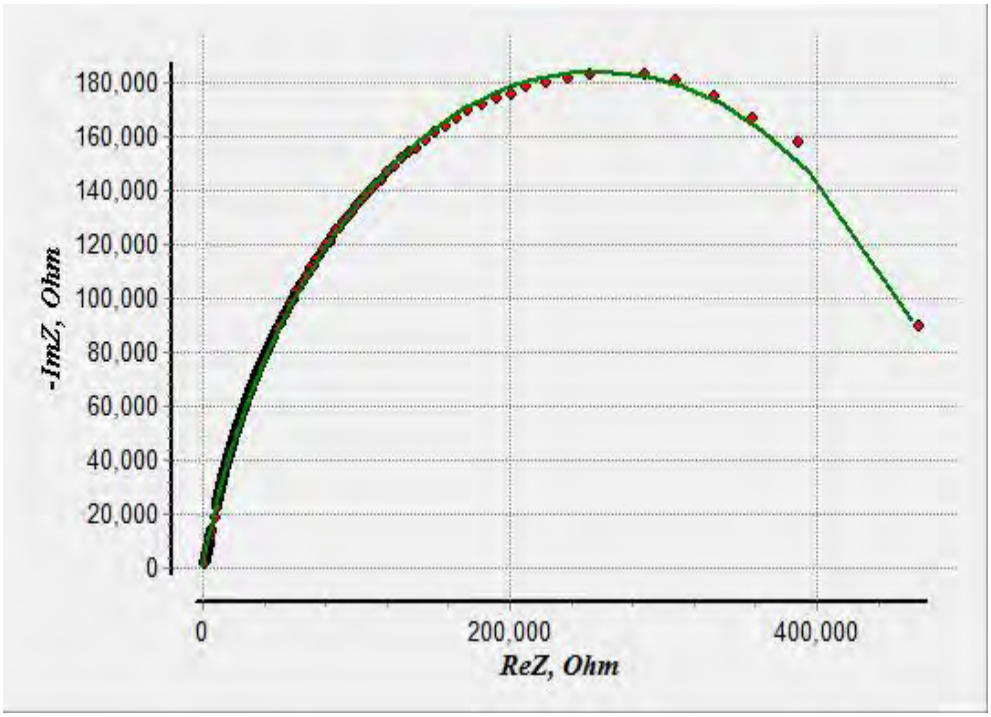

Figure 4.9: Example of fitting for PSB-1.5 at 250 °C using EIS spectrum analyzer software; red dots: measured dots, green line: fitting function.

$$\frac{R_{gb}}{T} = A_0 exp^{\frac{E_a}{kT}} \tag{4.6}$$

where A_0 is the pre-exponential factor, k is the Boltzmann constant and E_a is the activation energy for conduction.

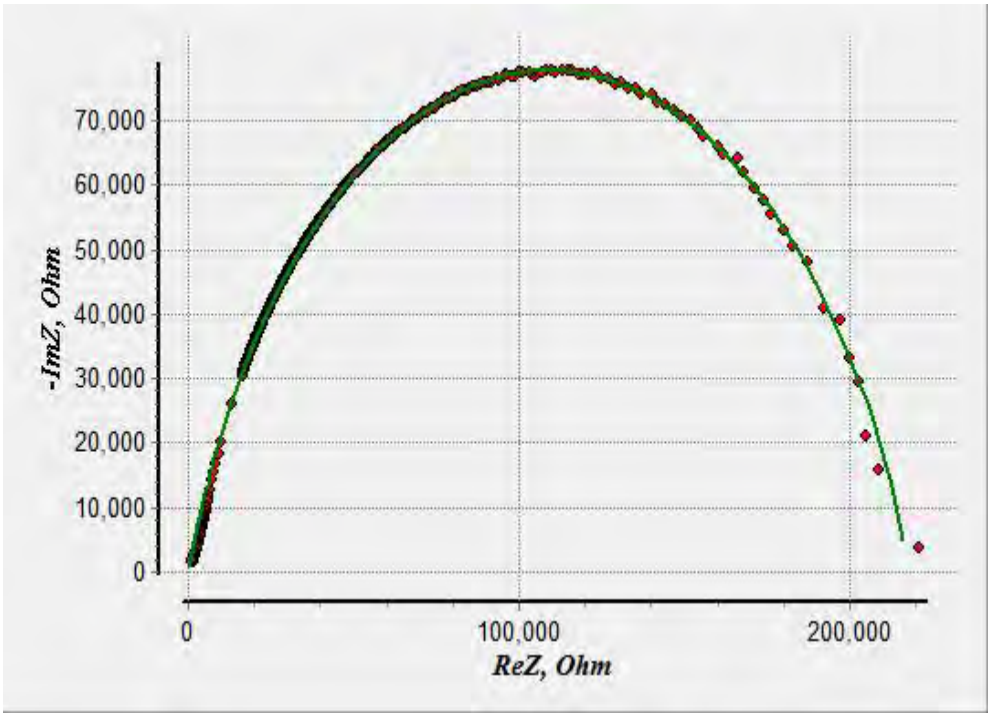

Figure 4.10: Example of fitting for PSB-1 at 250 °C using EIS spectrum analyzer software; red dots: measured dots, green line: fitting function.

The temperature dependence of the grain boundary relaxation time can be analyzed as:

$$\tau = \tau_0 exp^{\frac{E_{rp}}{kT}} \tag{4.7}$$

where τ_0 the pre-exponential factor, E_{rp} is the activation energy for the relaxation process at grain boundaries and T is the absolute temperature in Kelvin.

The ratio $R_{gb}/T - T$ was fitted with a polynomial curve (Figure 4.11) from which the activation energy for conduction (E_a) was estimated, 0.764 eV for PSB-1.5 and 0.796 eV for PSB-1. Using the same approach, from ratio $\tau - T$ (Figure 4.12), activation energy for the relaxation process (E_{rp}) was obtained, 0.732 eV for PSB-1.5 and 0.747 eV for PSB-1.

The small differences in the values of activation energies for conduction and relaxation may be due to the fact that the relaxation process involves only the hopping energy of carriers between localized states, while the conduction mechanism involves hopping energy and also disorder and binding energy of polarons [91]. The same type of charge carrier is responsible for both relaxation and conduction processes.

Table 4.1: Impedance spectra and its components for PSB-1.5 and PSB-1.

PSB-1.5					
Temp. (°C)	R_{gb} (Ohm)	g	$C(F)$	ω (Hz)	τ (s)
150	$2.056E^{7}$	0.91323	$5.638E^{-10}$	774.13	$1.29E^{-3}$
200	$1.839E^{6}$	0.85132	$1.283E^{-10}$	378.87	$2.64E^{-3}$
250	$5.145E^{5}$	0.79272	$1.340E^{-10}$	14496.14	$6.89E^{-5}$
300	$1.167E^{5}$	0.78721	$1.171E^{-10}$	73156.34	$1.37E^{-5}$
PSB-1					
Temp. (°C)	R_{gb} (Ohm)	n	$C(F)$	ω (Hz)	τ (s)
150	$2.291E^{7}$	0.91323	$5.638E^{-11}$	774.13	$1.29E^{-3}$
200	$1.839E^{6}$	0.83508	$7.109E^{-11}$	7648.96	$1.31E^{-4}$
250	$2.181E^{5}$	0.78839	$6.823E^{-11}$	67179.73	$1.49E^{-5}$
300	$3.771E^{4}$	0.76943	$5.565E^{-11}$	6476545.19	$2.09E^{-6}$

Temp. – temperature, R_{gb} – grain boundary resistance, g – fitted parameter, C – capacitance, ω – frequency, τ - grain boundary relaxation time .

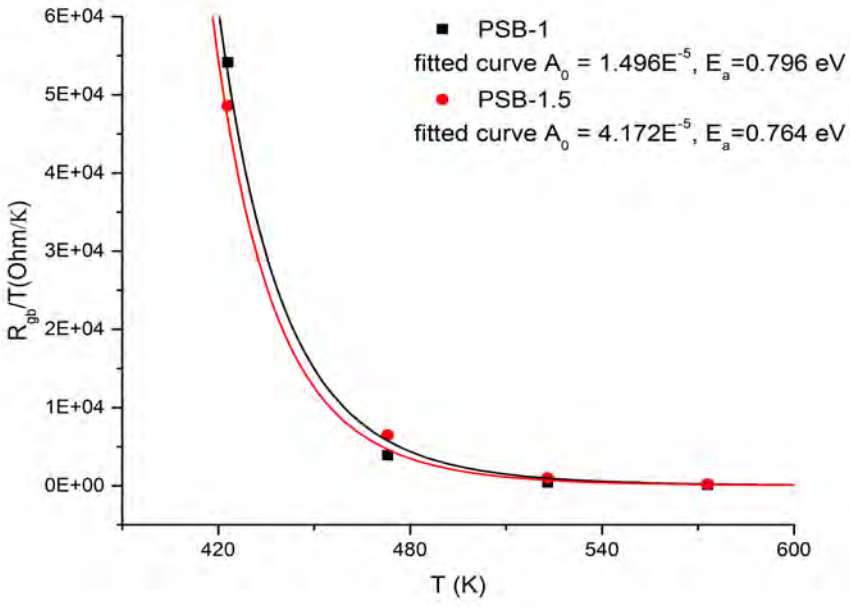

Figure 4.11: R_{gb}/T as a function of T for PSB-1.5 and PSB-1

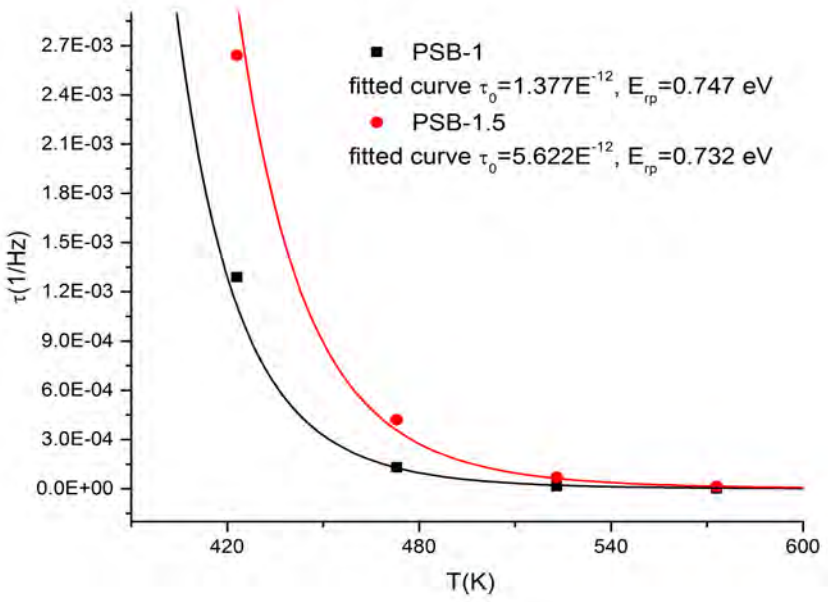

Figure 4.12: τ as a function of T for PSB-1.5 and PSB-1

4.1.2 Electrical Resistance

The electrical resistance of the specimens was measured as a function of temperature in the range of 100 °C - 300 °C, with different DC voltages in the range 1 - 12 V and they are given in Figure 4.13 and Figure 4.14.

PSB-1.5 has higher resistance values, compared to PSB-1, as can be distinguished from Figures 4.13 and 4.14. It can be also noted that for both materials with the increase of temperature, the electrical resistance is decreasing exponentially for all DC voltage values, showing a strong temperature dependence. Consequently it can be concluded that both PSB materials have a negative temperature coefficient (NTC). As the temperature increases, the difference in resistances of PSB-1.5 and PSB-1 are becoming smaller and smaller. Starting from 200 °C the resistances are in the same range, while at 300 °C the values are almost the same. Another observation is that for both materials with the increase of the DC voltage value, the resistance is decreasing, which makes them also voltage dependent materials. The resistance decrease is more prominent at lower temperatures (Figure 4.15).

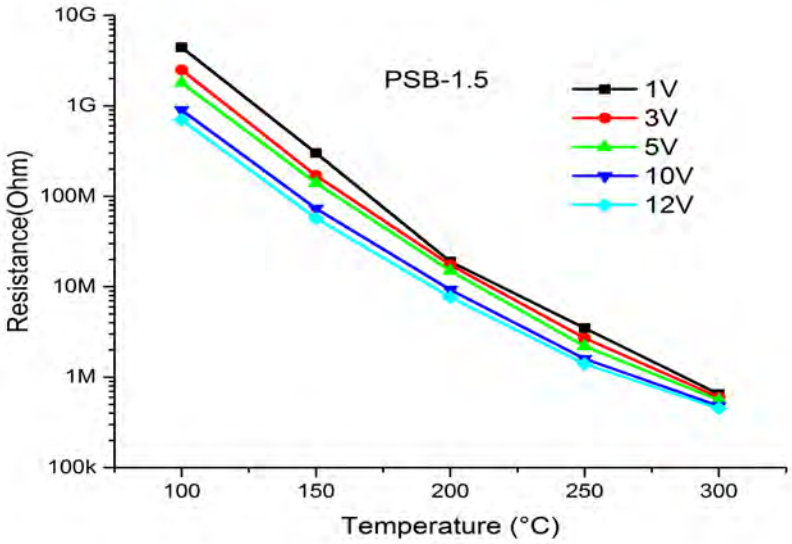

Figure 4.13: Resistance dependence of PSB-1.5 material on ambient temperature at various DC voltages.

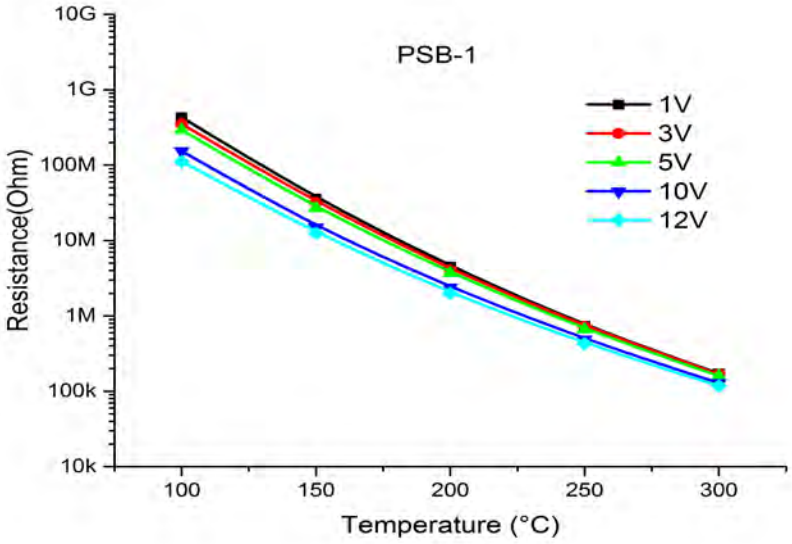

Figure 4.14: Resistance dependence of PSB-1 material on ambient temperature at various DC voltages.

Taking in to consideration the observed conclusions, it was decided that all future measurements will be performed with 3 V DC. This voltage value was selected mostly because of the practical aspects, it can be easily obtained from any power source, especially batteries, which offers excellent advantages for low power outdoor measurements using hand held devices.

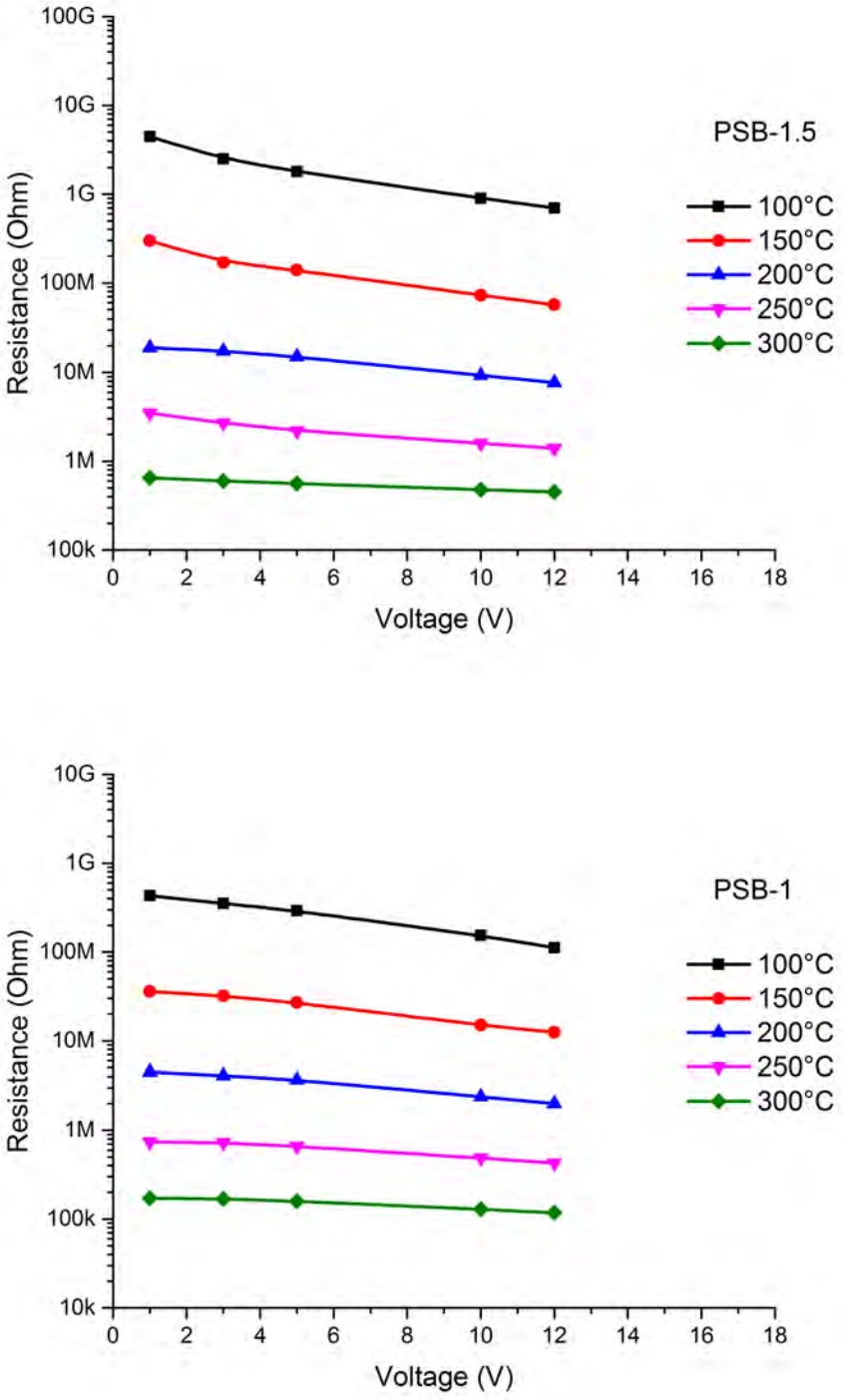

Figure 4.15: Resistance dependence of PSB-1.5 and PSB-1 material on *DC* voltage at various ambient temperatures.

4.2 Gas Sensitivity Analysis

Pseudobrookite thick films were tested for possible application for NO gas sensing. For that purpose, an in-house gas sensor testing set-up was developed in the frame of this thesis (Appendix B). The set up comprises of a gas mixing unit, measuring unit and a gas reactor where the testing specimens are placed. Inside the gas reactor, a hot plate and testing specimens are placed on top of it (Appendix B, Figure B.4). The hot plate was used to achieve the elevated temperatures necessary for proper operation of the gas sensor specimen under test. It is comprised of an aluminum block, in which two heating elements and a Pt100 element have been integrated. Pt100 was used for controlling and monitoring the on-site temperature. The entire heating process was controlled by a microcontroller unit with a closed loop heating/cooling sequence. Specimens were fixed on the hotplate and connected to a Keithley picoammeter/voltage source (Model 6487), which was used as a measuring unit for DC resistance measurements.

Before exposure to NO gas, samples were heated at 100 °C for one hour in order to eliminate moisture, which might have got in while the samples were stored in regular environmental air. At the same time 100 °C was the starting measuring temperature. Measurements were made in region 100 °C - 300 °C with a step of 50 °C, with 3 V DC.

At a certain temperature, real-time measurements have been performed before, during the gas exposure and after the gas exposure. The measuring sequence was the following: At a certain constant temperature specimens were measured for 15 minutes in dry air and afterwards 5% of NO diluted in synthetic air was released into the reactor with a flow of 3000 cm^3/min for the next 5 minutes in order to identify the initial state. The reactor volume is 80 cm^3 and it is estimated that after 5 minutes with a flow of 3000 cm^3/min the entire volume has the final targeted gas concentration. Once the reactor volume is filled, the NO gas is trapped in the reactor at a pressure of 1 bar. During that period, a chemical reaction is expected to occur and the specimen behavior is recorded. After the gas exposure phase, the reactor is refilled with dry air at the mentioned flow rate for 5 minutes and closed for characterizing the specimen's relaxation behavior.

4.2.1 PSB-1.5

When an n-type MOS gas sensitive material is being exposed to a reducing gas such as NO, the electrical resistance will decrease, while when exposed to an oxidizing gas such as O_2, the electrical resistance will increase. Having this in mind, the obtained measurement results have been analyzed. First PSB-1.5 was analyzed and it was determined that at 100 °C the measured values are relatively high and unstable, and identifying characteristic reactions on the gas was too uncertain.

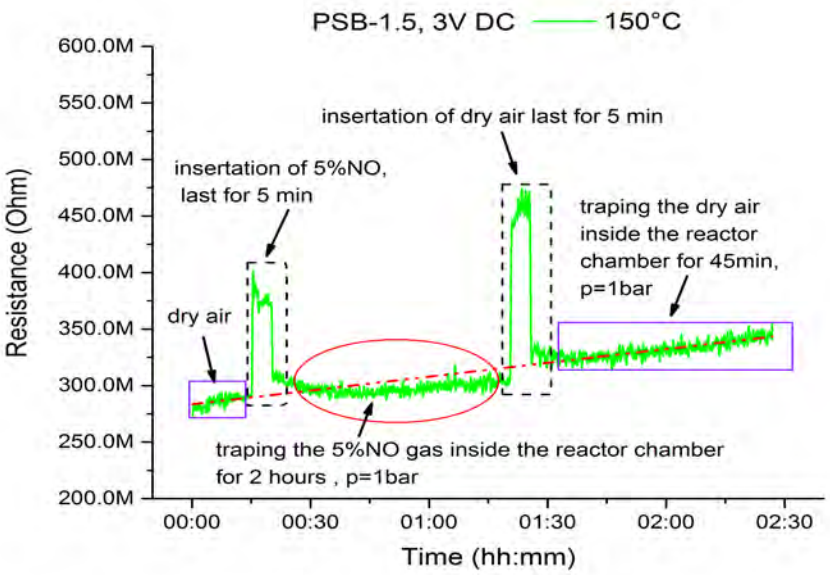

Figure 4.16: Resistance change of PSB-1.5 when exposed to 5% of NO diluted in synthetic air at 150 °C.

At 150 °C, PSB-1.5 exhibited a better and clearer response (Figure 4.16). Figure 4.16 shows that when the sensor is exposed to dry air (purple rectangle), the resistance is increasing, while when exposed to NO (red ellipse) the resistance stopped increasing and it relatively stagnates. When air is introduced again (purple rectangle) the resistance again started to increase so that a conclusion can be drawn that already at 150 °C PSB-1.5 exhibited a distinct sensitivity to NO gas.

Another observation is that there is a clearly visible rapid resistance increase when inserting gas or air, as shown in Figure 4.16 with dashed black rectangles. This increase is due to the temperature difference between the inserting gaseous analyte and the sensor ambient. As already shown in section 4.1, PSB materials exhibited a strong temperature dependence. When inserting gas or air we are disturbing the thermal equilibrium and the boundary conditions of the entire sensor environment. With this disorder, the sample's immediate environment is cooled down in this moment and we are directly influencing the heat transfer, mostly the convection and radiation. In other words, the inserting gas (air) is close to room temperature, while the sensor specimen was heated up to a much higher temperature, thus by inserting a gaseous analyte the sensors's local environment is being cooled down hence the resistance is increased.

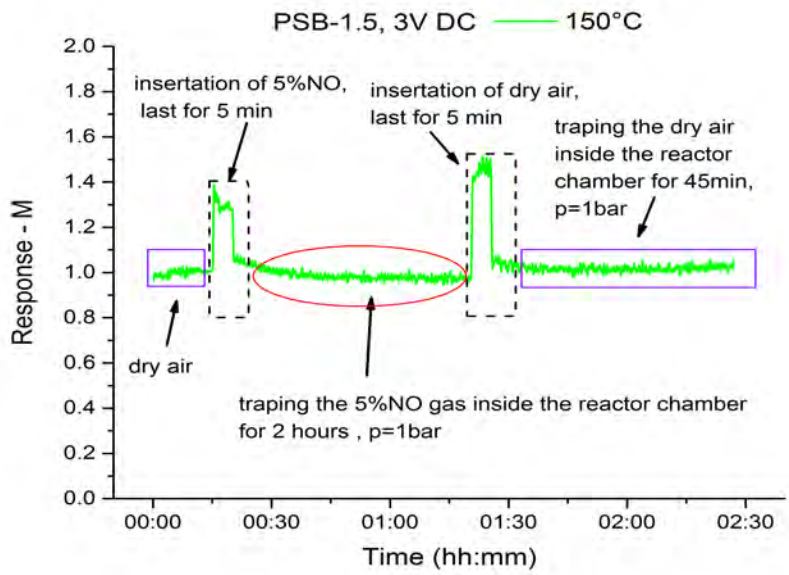

Figure 4.17: Response of PSB-1.5 to 5% of NO diluted in synthetic air at 150 °C.

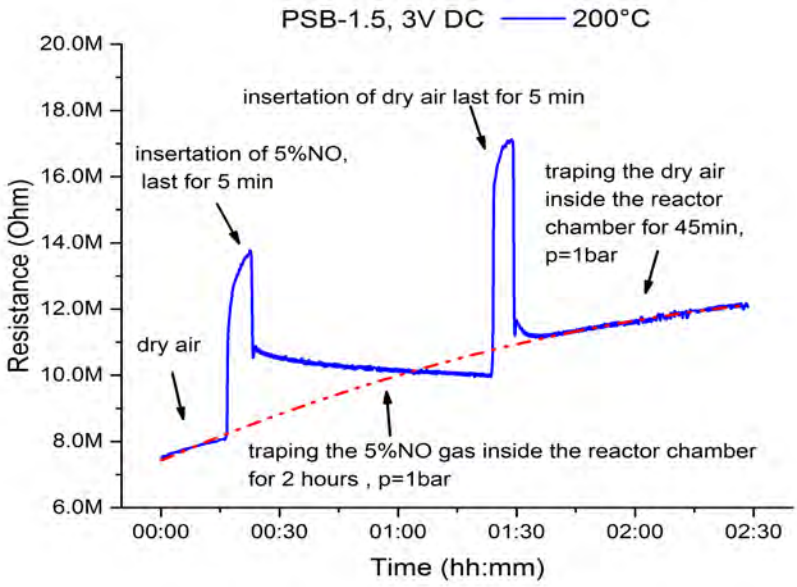

Figure 4.18: Resistance change of PSB-1.5 when exposed to 5% of NO diluted in synthetic air at 200 °C.

If the resistance change upon an exposure to dry air is fitted with a polynomial function (Figure 4.16, red dotted line), we can anticipate the resistance change of the sensor over longer period of time. From the Figure 4.16 (red ellipse) it can be easily seen that there is a resistance decrease when the NO gas is being trapped inside the reactor chamber, compared to the anticipated resistance change when it is exposed to air. The sensor's response (M) can be expressed (Figure 4.17) using the following equation:

$$M = \frac{R_{gas}}{R_{air}} \tag{4.8}$$

where R_{gas} is the measured resistance of the sensor when it is exposed to gas and R_{air} is the anticipated resistance of the sensor when it is exposed to air.

When the sensor is exposed to dry air, $M \approx 1$ ($R_{gas} = R_{air}$, Figure 4.17, purple rectangles), while when exposed to NO gas, $M < 1$ ($R_{gas} < R_{air}$, Figure 4.17, red ellipse). The influence of thermal disorder caused by the insertion of gaseous analyte is intentionally omitted from this graph.

Already at 200 °C the resistance change is much more prominent, as can be seen from Figure 4.18. Here it can be seen that again when exposed to dry air, the resistance increases, while when exposed to gas, it decreases. The longer the exposure, the higher is the resistance change, since more gas molecules will react with ionosorbed oxygen species (2.1.2). Compared to 150 °C, here it can be noted that the gas sensing is much more prominent because the resistance is clearly decreasing when PSB-1.5 is exposed to NO gas. The sensor's response at 200 °C is given in Figure 4.19.

By increasing the temperature to 250 °C and 300 °C, the decrease of the electrical resistance is much more prominent (Figures 4.20 and 4.22) thus the response-to-noise is much higher and the material's reaction on the gas can be quantified much better (clearer) as can be seen from Figures 4.21 and 4.23, respectively. It can be noted that by increasing the temperature the sensor's response is becoming better and that the best response is achieved at 300 °C.

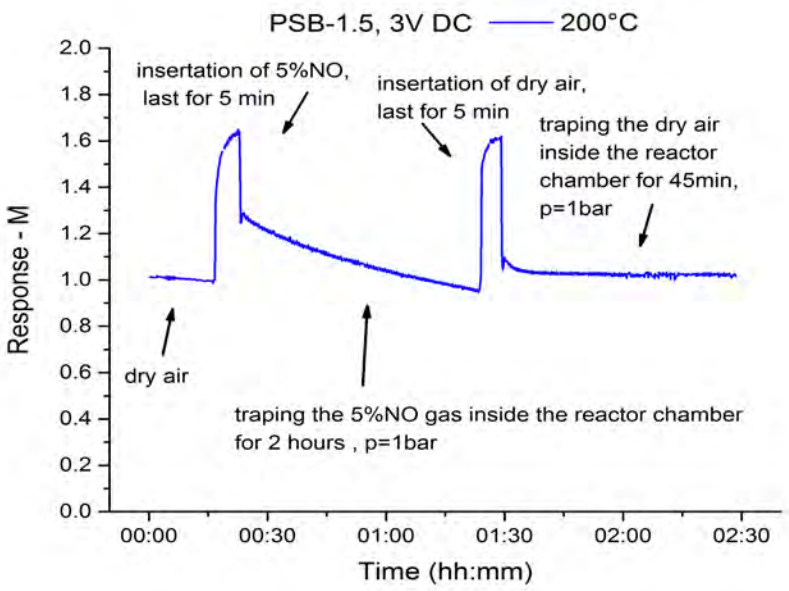

Figure 4.19: Response of PSB-1.5 to 5% of NO diluted in synthetic air at 200 °C.

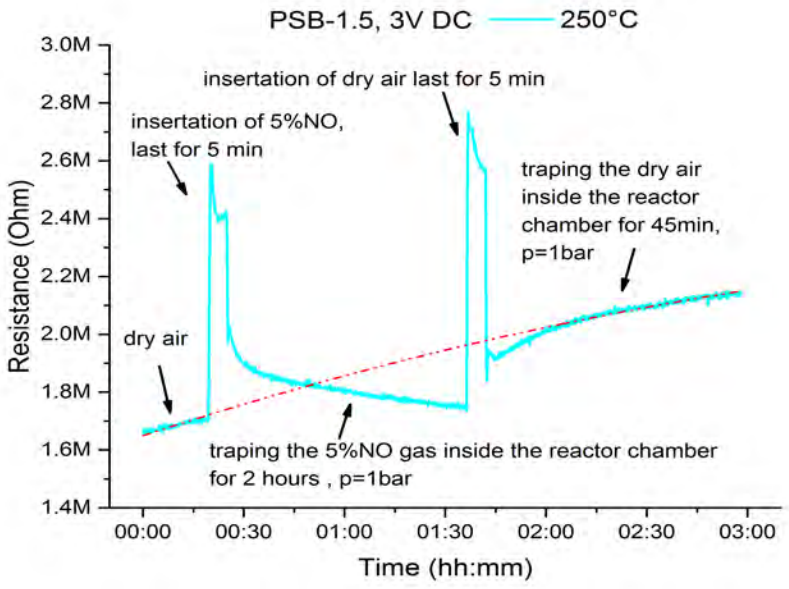

Figure 4.20: Resistance change of PSB-1.5 when exposed to 5% of NO diluted in synthetic air at 250 °C.

Nonetheless at 300 °C, after repeated exposure to dry air, different behavior of PSB-1.5 was noted. It can be seen that resistance continued to decrease even after reinsertion of dry air. This phenomenon could be explained by the enhanced material sensitivity at 300 °C and thus the time needed for NO deliverance from PSB will be significantly longer. The same specimen was exposed under the same condition on the following day and a similar response was obtained, indicating that after a longer period of time, the material will regain its sensing properties.

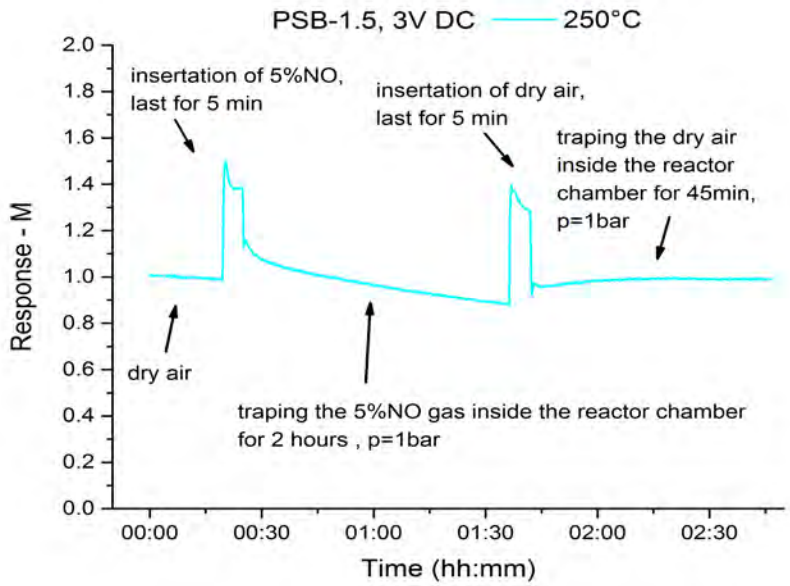

Figure 4.21: Response of PSB-1.5 to 5% of NO diluted in synthetic air at 250 °C.

In order to back up the assumption about the influences of oxidizing and reducing gases on the electrical resistance of an n-type MOS gas sensitive material such as PSB, and thus a resistance change has to be expected also under pure air, one of the specimens with PSB-1.5 thick film was analyzed in high vacuum (10^{-9} mbar) at 200 °C (Figure 4.24). It shows that for one and a half hours the resistance of the specimen is unchanged. Of course some small oscillations can be noted as well, but they are contributed by the temperature oscillations caused by the closed loop temperature regulation.

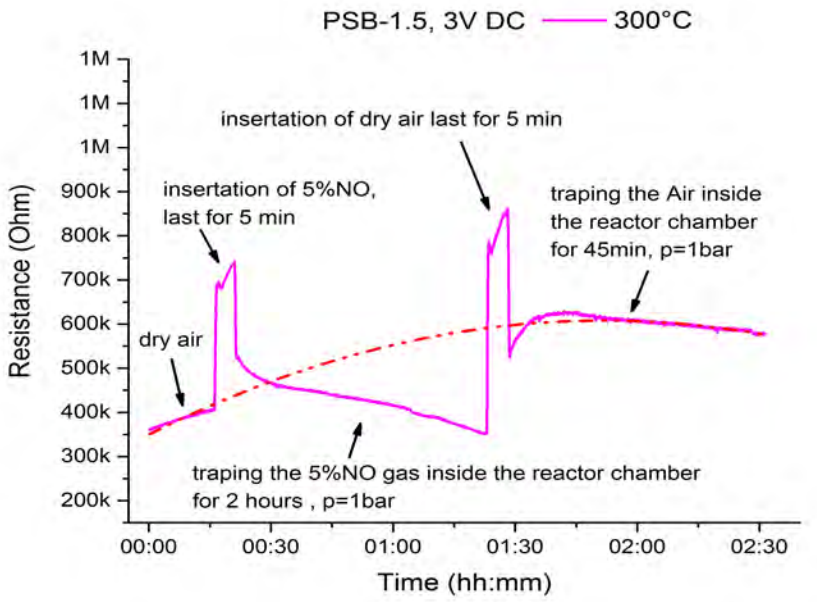

Figure 4.22: Resistance change of PSB-1.5 when exposed to 5% of NO diluted in synthetic air at 300 °C.

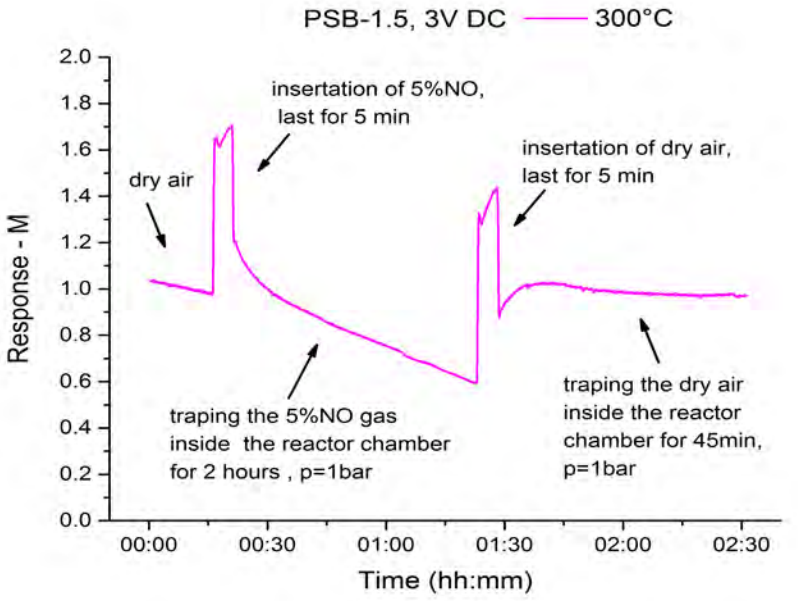

Figure 4.23: Response of PSB-1.5 to 5% of NO diluted in synthetic air at 300 °C.

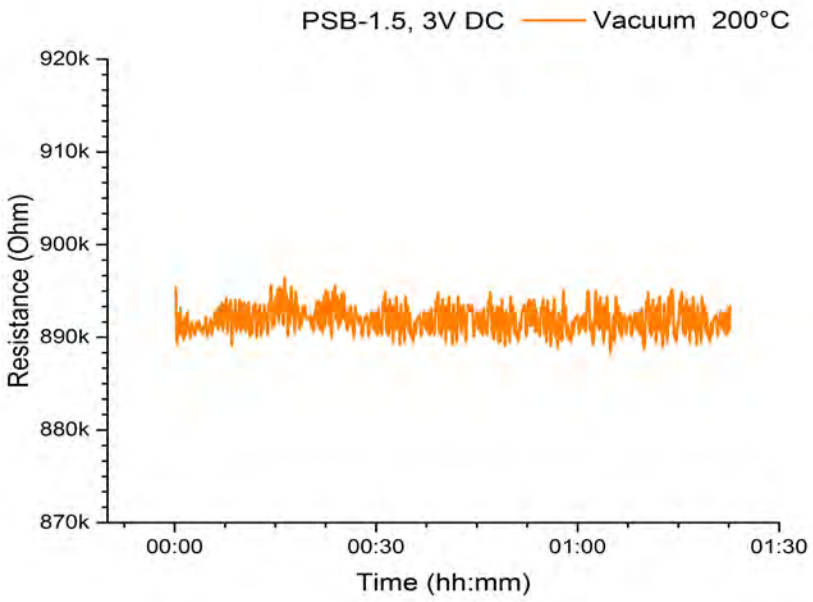

Figure 4.24: Resistance change of PSB-1.5 in vacuum at 200 °C.

4.2.2 PSB-1

PSB-1 was analyzed under the same testing circumstances as PSB-1.5. Similar to PSB-1.5, at 100 °C the measured electrical resistance was unstable and simply hard for reading out.

At 150 °C and 200 °C measured values were much better for reading out and the results are given in Figure 4.25 and 4.26. They show that a clear resistance decrease, when exposed to NO gas, cannot be seen, hence the sensitivity at those temperatures is below measuring accuracy. As it can be noted from the figures, influences of the inserting gaseous analyte (air and gas) are also visible in the case of specimens with PSB-1 thick film.

Specimens which have been exposed to 5% of NO diluted in synthetic air at 250 °C exhibited sensitivity (Figure 4.27). As it can be seen, there is a clearly visible attenuation of electrical resistance when the specimen is exposed to NO gas. On the other hand, when the specimen is exposed to dry air, the resistance has a tendency to increase in time. A different sensitivity to temperature could be observed: The PSB-1.5 started to become gas sensitive already at 150 °C, while the PSB-1 exhibited a detectable sensitivity only starting from 250 °C.

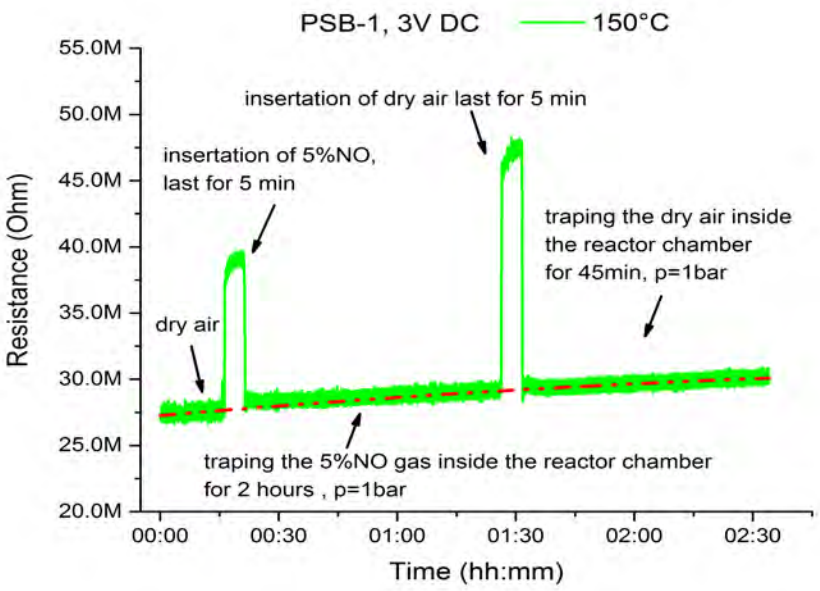

Figure 4.25: Resistance change of PSB-1 when exposed to 5% of NO diluted in synthetic air at 150 °C.

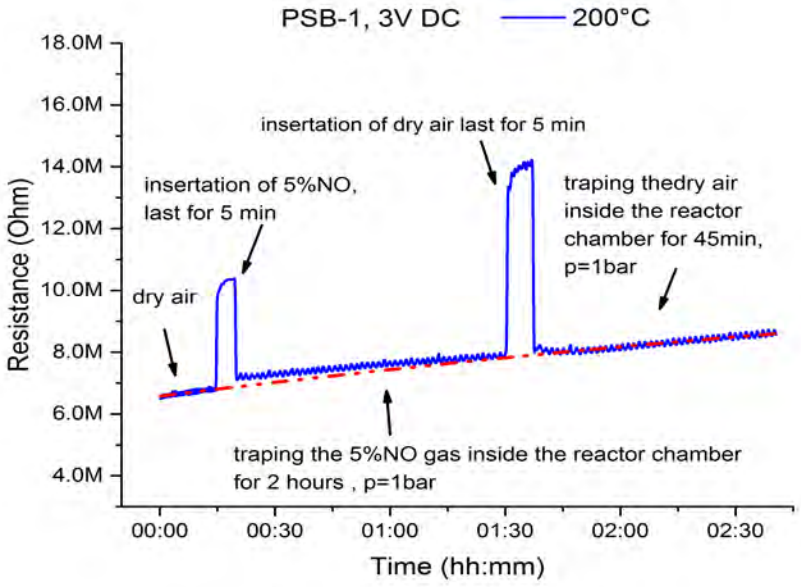

Figure 4.26: Resistance change of PSB-1 when exposed to 5% of NO diluted in synthetic air at 200 °C.

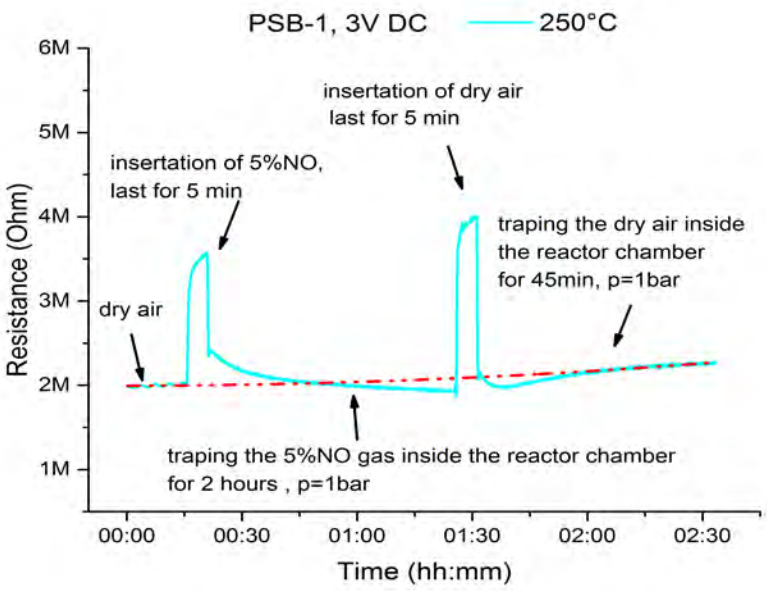

Figure 4.27: Resistance change of PSB-1 when exposed to 5% of NO diluted in synthetic air at 250 °C.

The response of the specimen exposed at 250 °C is given in Figure 4.28. If we compare resistance changes of PSB-1.5 and PSB-1 at 250 °C it can be seen that the resistance decrease is stronger for PSB-1.5 and therefore the response of PSB-1.5 (Figure 4.21) is more prominent than the response of PSB-1. By increasing the temperature to 300 °C, the resistance decrease is much more noticeable, compared to the previous exposures at lower temperatures, hence the response is improved (Figure 4.30). The phenomenon of resistance decreasing after reinsertion of dry air is visible in this case as well. Once more, the conclusion is that the higher the sensor's temperature, the better the response. If we compare the resistance changes of PSB-1.5 and PSB-1 at 300 °C, it can be seen that again PSB-1.5 has more noticeable resistance decrease and hence its response is better.

PSB-1.5 composition proved to be much more sensitive at lower temperatures and the reason for that could lie in the fact that PSB-1.5 is comprised from orthorhombic pseudobrookite, monoclinic pseudobrookite and rutile, while PSB-1 is comprised only from pure orthorhombic pseudobrookite. For both materials, increase in the temperature has a positive influence on the sensing performance hence the sensitivity is enhanced and more prompt at higher temperatures and at 300 °C the sensitivity is the highest.

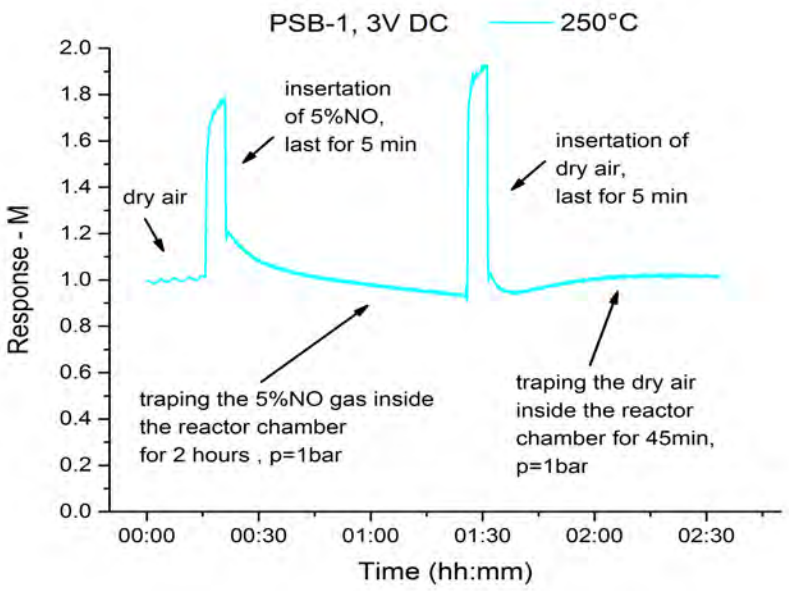

Figure 4.28: Response of PSB-1 to 5% of NO diluted in synthetic air at 250 °C.

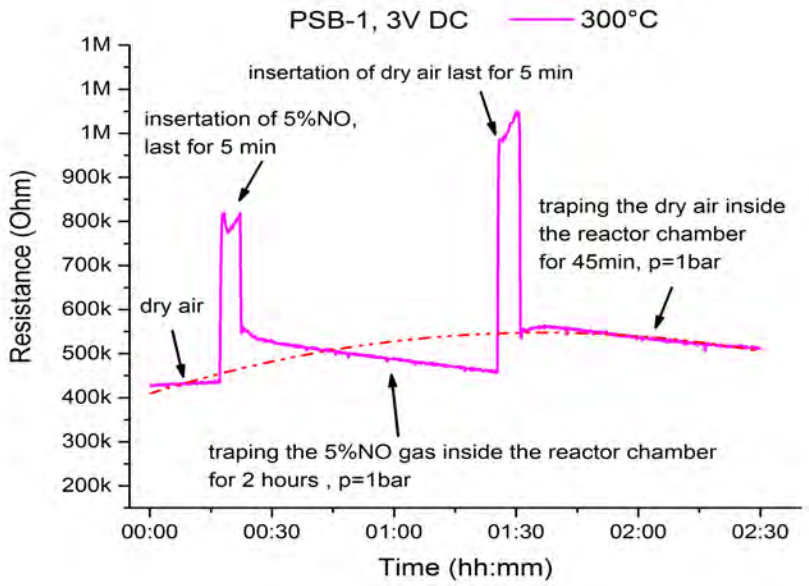

Figure 4.29: Resistance change of PSB-1 when exposed to 5% of NO diluted in synthetic air at 300 °C.

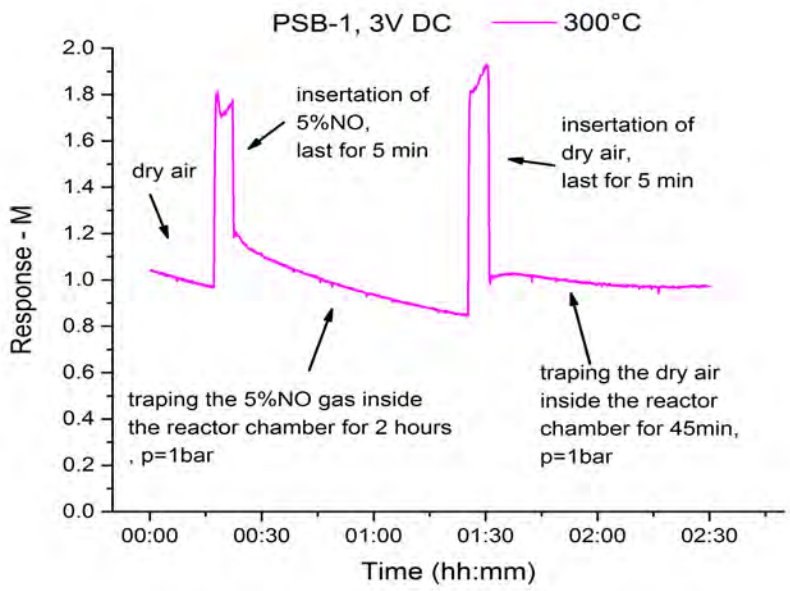

Figure 4.30: Response of PSB-1 to 5% of NO diluted in synthetic air at 300 °C.

Table 4.2: Comparison of relative response $\bar{r}_{NO}$ of PSB-1.5 and PSB-1 specimens for a gas mixture of 5% NO in synthetic air.

Temperature (°C)	$\bar{r}_{NO}$ of PSB-1.5	$\bar{r}_{NO}$ of PSB-1
150	-0.16	
200	-0.35	
250	-0.54	-0.37
300	-1.04	-0.84

To have better assessment of the sensor's response, we compared the slopes of the resistance changes with time. For that purpose we introduced the relative response ($\bar{r}_{NO}$), which can be expressed by the following relation:

$$\bar{r}_{NO} = \frac{\frac{dR_{gas}}{dt}}{\frac{dR_{air}}{dt}} \tag{4.9}$$

where $\frac{dR_{gas}}{dt}$ and $\frac{dR_{air}}{dt}$ are the resistance change with time when exposed to NO gas and to dry air, respectively.

The obtained values are given in Table 4.2. In the case of PSB-1.5 it can be noted that at 150 °C relative response is -0.16 while at 300 °C it is -1.04. As for the PSB-1, the response at 250 °C is -0.37, while at 300 °C is -0.84. In both cases,

increasement of the operating temperature has a positive effect on the relative response. If we compare the relative response at 250 °C and 300 °C, we can conclude that PSB-1.5 has a better response than the PSB-1.

Chapter 5

Conclusion

The main motivation for this research was to contribute to progresses in technology and measurement process for the exhaust gas monitoring with distributed gas sensors. For this purpose sensors with sufficient sensitivity at lowest possible energy consumption are required.

The goal of this thesis was to synthesize, analyze and characterize pseudobrookite (Fe_2TiO_5), a novel metal oxide based gas sensitive semiconducting material with the promising feature of having a sensitivity already at low operating temperatures, significantly below 300 °C. The attention in this thesis was given to nitrogen oxide NO, since it is the most present and the most widespread air pollutant in the 21^{st} century.

A comprehensive overview of the most prominent pollutants with a short description and regulations was given in the first chapter, while several different methods for gas sensing have been given and explained in the second chapter. The main accent here was put on the sensing mechanism of metal oxide semiconductor materials in a comprehensive analysis, including a study of influencing factors.

Main properties as well as a short analysis of bulk PSB are given in chapter three. A mixture of nanopowders in the molar ratio 1:1.5 (hematite: anatase) was made and is referred to as PSB-1.5. From the mixture, round shaped tablets were made and sintered in the temperature range 750 °C - 1250 °C for two hours. X-ray Powder Diffraction (XRD) analysis showed that the sintering temperature of 750 °C was too low for pseudobrookite formation and that at 750 °C the anatase to rutile phase transformation has started. Already at 850 °C orthorhombic pseudobrookite has formed and the anatase to rutile phase transformation was complete. The fastest change in sample density occurred between sintering temperatures of 850 °C and 950 °C, from 2.78 g/cm^3 to 3.63 g/cm^3. Sample density increased more slowly for sintering temperatures above 950 °C, reaching 4 g/cm^3 at 1250 °C. Scanning Electron Microscopy (SEM) and Energy-dispersive X-ray spectroscopy (EDS)

of the bulk material showed that with the increase of the sintering temperature the porosity is reduced while the grain size is increased due to advancement of the sintering process.

The obtained nanopowder mixture was used to form thick film paste by adding an organic vehicle (butyl cellulose) and a small amount of binding lead boron silicone oxide glass frit. It was screen printed on an alumina substrate and the specimens were sintered in a hybrid conveyor furnace in a temperature range between 800 °C and 950 °C, with a 50 °C step, for 10 minutes. XRD analysis showed that at 800 °C pseudobrookite was formed, but monoclinic pseudobrookite was the dominant phase rather than orthorhombic. At 900 °C all three phases are clearly visible and the transformation from monoclinic into orthorhombic pseudobrookite has continued. The estimated weight ratio between monoclinic and orthorhombic pseudobrookite is 2.36:1. At 950 °C, most of monoclinic pseudobrookite has transformed into orthorhombic and the estimated weight ratio is 1:23.3 (monoclinic:orthorhombic). Specimens sintered at 800 °C were flaking indicating that the sintering temperature was apparently too low, so they were not investigated further by SEM. Specimens sintered at 850 °C showed high porosity, small grain size and the most homogeneous structure compared to higher sintering temperatures. Of course, with the increase of the sintering temperature grain size increased, larger rod shaped grains characteristic for orthorhombic pseudobrookite started to appear and porosity decreased. The crystallite size for PSB-1.5 thick film specimens sintered in the region 850 °C - 950 °C showed to be in the region of 40-170 nm.

Compared to bulk specimens, where orthorhombic pseudobrookite was formed, in the case of thick film specimens monoclinic pseudobrookite is the dominant phase. Since the same starting nanopowder composition was used in both cases, the possible explanation for this phenomenon could be attributed to the presence of the binder in thick film paste. Moreover the fact that thick films are much more porous than bulk specimens could also contribute to the formation of the more defective monoclinic pseudobrookite structure.

For comparison, an ideal molar ratio 1:1 (hematite:anatase) was made. Starting from hematite (Fe_2O_3, Alfa Aesar, 99%, grain size 20-60 nm) and anatase (TiO_2, Alfa Aesar, 99.7%, grain size 15nm) in a form of nanopowders, this mixture is referred to as PSB-1. From the obtained mixture a thick film paste was prepared using the same preparation technique. It was screen printed on alumina substrate under the same conditions as the PSB-1.5 specimens and sintered in the same temperature range, 800 °C - 950 °C, for 10 minutes. XRD patterns showed that PSB-1 has a pure orthorhombic pseudobrookite morphology, while PSB-1.5 is a mixture of orthorhombic pseudobrookite, monoclinic pseudobrookite and a small amount of rutile. SEM micrographs showed that PSB-1 has a slightly larger

grain size than PSB-1.5. As for the electrical resistance, PSB-1.5 specimens exhibited higher resistance values than the PSB-1 specimens, most probably due to the small amount of rutile in PSB-1.5. For both types of PSB an exponential decrease in the resistance with increase in temperature was noted. The values determined from the Tauc plots were 2.05 eV direct band gap, 1.63 eV indirect for PSB-1 and 2.09 eV direct band gap, indirect 1.77 eV for PSB-1.5.

Impedance measurements of PSB-1.5 and PSB-1 thick film specimens are given in chapter four. It was concluded that for both materials the impedance values were high and the shape of the resistance-reactance curve at low frequencies at 50 °C and to some extent at 100 °C was almost linear. Starting from 150 °C this effect was less noticeable. In case of PSB-1.5, at 250 °C the resistance-reactance curve is almost semicircular, while at 300 °C the curve is semicircular. Compared to PSB-1.5, the values of resistance-reactance curve of PSB-1 are lower than the values of PSB-1 and the resistance-reactance curve of PSB-1 is semicircular already at 250 °C. Clearly, the resistance-reactance curve of PSB-1 is also semicircular at 300 °C. From the ratio $Rgb/T - T$ the activation energy of 0.764 eV for PSB-1.5 and 0.796 eV for PSB-1 was estimated, while from the ratio $\tau - T$, the activation energy of 0.732 eV for PSB-1.5 and 0.747 eV for PSB-1 was obtained. The small differences in the values of activation energies for conduction and relaxation may be due to the fact that the relaxation process involves only the hopping energy of carriers between localized states, while the conduction mechanism involves hopping energy and also disorder and binding energy of polarons [91]. The same type of charge carrier is responsible for both relaxation and conduction processes.

Analysis and characterization of the sensor structure is also given in chapter four. The electrical resistance of the specimens was measured as a function of the temperature in the temperature range of 100 °C - 300 °C, with different DC voltages in the range 1 V - 12 V. It was concluded that PSB-1.5 has a higher resistance values, compared to PSB-1. Both materials exhibited decrease of the electrical resistance with increasing temperature, showing their strong temperature dependence. Nonetheless, starting from 200 °C the resistances of PSB-1.5 and PSB-1 were in the same range, while at 300 °C the values were almost the same. Another conclusion is that with the increase of the DC voltage value, the resistance is decreasing, which makes them also a voltage dependent material. The resistance decrease is more prominent at lower temperatures.

Pseudobrookite thick films were tested for possible application for NO gas sensing at low temperatures. It was concluded that already at 150 °C PSB-1.5 exhibited a detectable response for the presence of 5% of NO diluted in synthetic air, while PSB-1 exhibited a response starting from 250 °C. Obviously the PSB-1.5 composition proved to be much more sensitive at lower temperatures and the reason for that could lie in the fact that PSB-1.5 is comprised from orthorhombic

pseudobrookite, monoclinic pseudobrookite and rutile, while PSB-1 is comprised only from pure orthorhombic pseudobrookite. For both materials, increase in the temperature has a positive influence on the sensing performance hence the sensitivity is enhanced and more prompt at higher temperatures and at 300 °C the sensitivity is the highest. Values for relative response also confirmed that the PSB-1.5 has higher sensitivity than the PSB-1. Moreover if those values are compared at the same temperatures (250 °C and 300 °C) it can be conceded that PSB-1.5 still exhibits better sensitivity.

Future work on this topic will include investigations on pseudobrookite sensitivity toward other pollutants, primarily to CO, CO_2 and NO_2. Implementation of the Low Temperature Co-Fired Ceramic (LTCC) technology will also be one of the future tasks. Using LTCC technology, further miniaturization of the specimens would be possible and moreover implementation of 3D structures with buried passive components (such as heater, appendix A) in to the LTCC substrate would be possible.

Appendix A

Gas sensor concept

A concept of a miniaturized low-power gas sensor with an integrated microheater was realized (Figure A.1) using Low Temperature Co-Fired (LTCC) technology. As seen from the figure, the well known star shaped design was used.

Issues such as equal temperature distribution at the sensing area and not allowing distribution of the temperature to the surroundings had to be overcome, so flux barriers were used. By using star shaped design with curved symmetrical suspensions the influence of thermo-mechanical buckling is diminished.

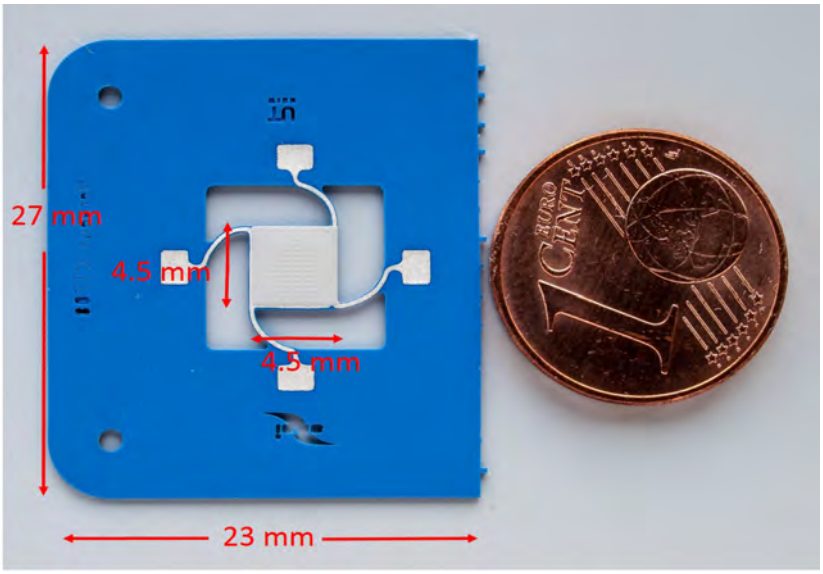

Figure A.1: Appearance of the conceptual gas sensor realized in LTCC technology, comparison with one euro cent.

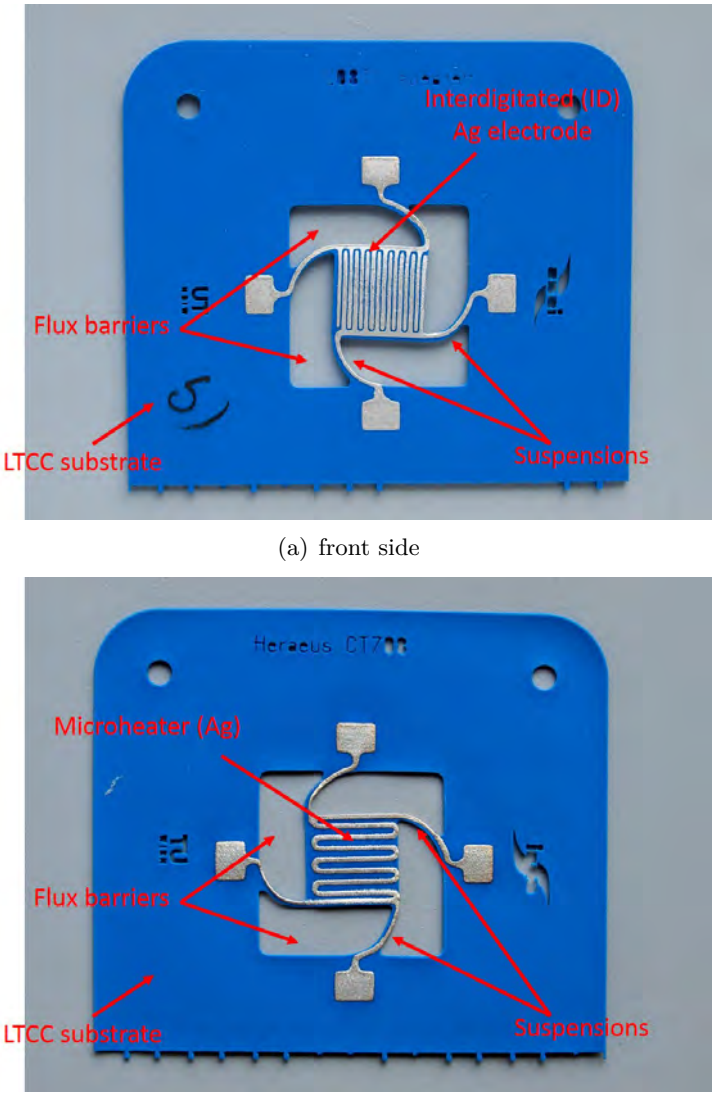

(a) front side

(b) bottom side

Figure A.2: Appearance of the fabricated conceptual gas sensor realized in LTCC technology,(a) top side and (b) bottom side

LTCC tapes have been shaped by laser (Nd:YAG, Rofin RSM 100 D II TEM00) in order to obtain high precision patterns ready for screen printing deposition. Using a DeHaart SPSA-10 semi-automatic screen printer, ID electrode and meander shaped microheater structure have been screen printed. Silver conductive paste Heraeus TC 7306-A was used for that purpose. On the top side of a single green LTCC tape ID electrode were printed (Figure A.2 (a)), while on the bottom side the microheater structure was printed (Figure A.2 (b)). Afterwards the ID elec-

trode and the heater structure were dried for 10 minutes at 125 °C. On top of the Ag electrodes a binary MOS mixture ZnO-La_2O_3 was deposited and again dried using the same procedure. Tapes have been stacked together in a press mold and then the multi-layered samples were laminated. Lamination was performed in a uniaxial press (Carver 3895CE Auto Four/30) under a pressure of 8.5 MPa for 3 minutes at a temperature of 75 °C. Specimens were afterwards placed between two Ceramtec A (Ceramtec GmbH) alumina tapes to reduce warping, and then unconstrained co-fired in a belt furnace (BTU Systems) at peak temperature of 850 °C in a total firing cycle of approximately two hours.

The specimen is comprised of 3 layers of Heraeus CT 708 tape. The interdigitated electrode (ID) has 4 connection pads as well as the microheater, that has been taken into account in both cases for 4-point measurements . The width of the electrode finger is 100 μm while spacing between them is 25-30 μm. The ID electrode is comprised of 16 fingers and the finger length of is approximately 4 mm. The width of the microheater line is 100 μm, while the distance between lines is 200 μm. Overall dimension of the sensing area is 4.5 mm times 4.5 mm, while the entire senor structure is 23 mm times 27 mm.

Appendix B

Gas Testing Set-Up

The in-house gas sensor testing set-up was designed as presented in Figure B.1. The set-up was designed so that if offers possibility to expose sensors to the toxic, corrosive and flammable gases. Currently the facility is capable to test sensitivity toward CO, CO_2, H_2, HCl, NO, NO_2, SO_2, NH_3 and hydrocarbon gases with a possibility to expand to other types of gases. Using computer controlled gas mixing units, pure or premixed gases can be diluted up to a ppb concentration range, afterwards diluted gases can be mixed in different proportions. As for the carrier gases gas mixing units are calibrated for bought types, synthetic air and nitrogen.

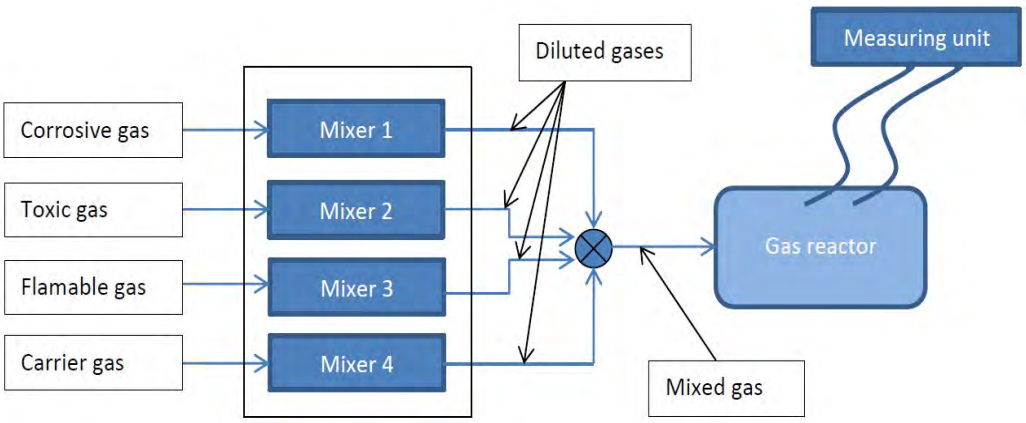

Figure B.1: Schematic representation of the gas sensor testing set-up.

A closer view of the design of the gas reactor is given in Figure B.2 where a 3D model of the chamber is presented. Major parts of the gas chamber are stainless steel plates, a borosilicate glass tube and alumina sticks for holding the specimen. Chamber has 18 BNC connections, and it is designed to meet the needs of the most demanding measurement configurations such as 4 points measurements,

measurement of ambient and sensor temperature, feeding the heating element and etc. The tightness of the reactor was tested by a helium leakage tester.

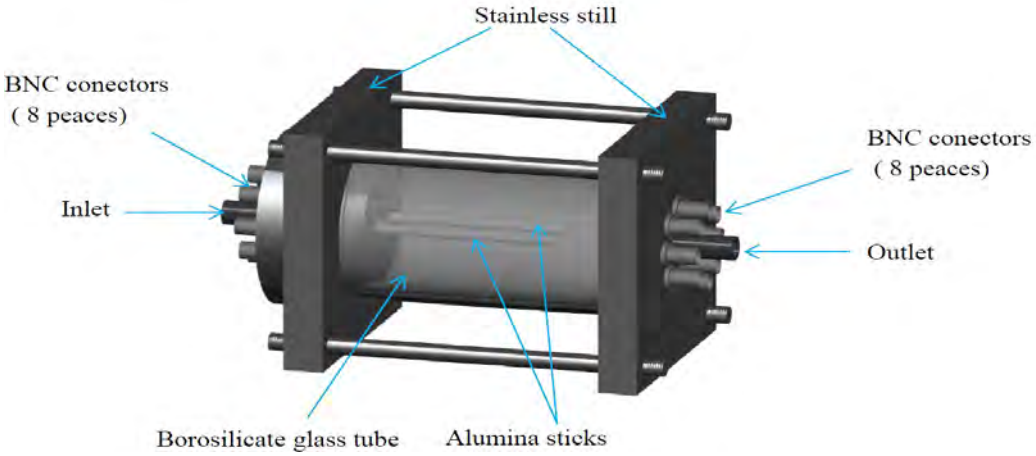

Figure B.2: 3D Model of the gas reactor.

The appearance of the assembled set-up is given in Figure B.3 where the mass flow controllers, measuring unit (Keithley picoammeter/voltage source (Model 6487)) and the gas reactor with integrated hot plate are indicated.

A hot plate was placed in the gas reactor and testing specimens were placed on top. The hot plate was used to achieve the elevated temperatures necessary for proper operation of the gas sensor. It is comprised of an aluminum block, in which two heating elements and a Pt100 element have been integrated, as indicated in Figure B.4. Pt100 was used for controlling and monitoring the on-site temperature. The entire heating process was controlled by a microcontroller unit, and simulation results are given in C.

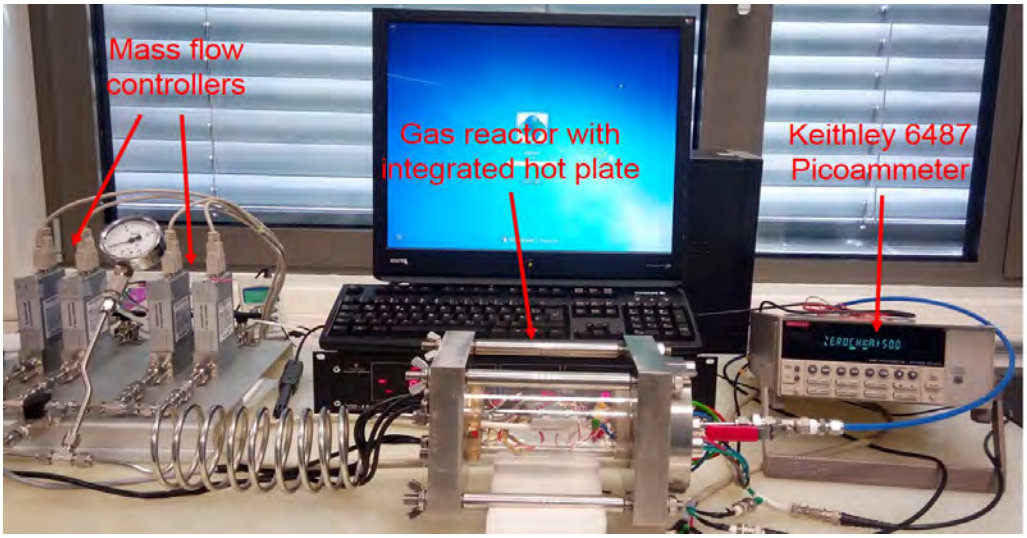

Figure B.3: Assembled sensor testing set-up.

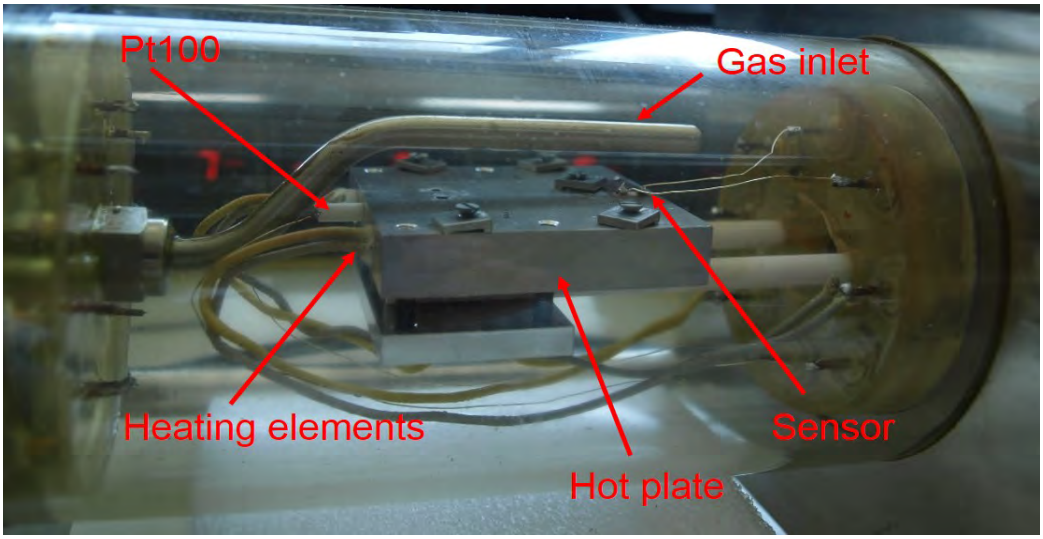

Figure B.4: Assembled sensor testing set-up.

Appendix C

Hot Plate

The hot plate was comprised of an aluminum bloc in which two heating elements and a Pt100 element were integrated. The overall dimension of the aluminum block was 5 cm in length and width, and 1 cm in height. The hot plate was simulated using the Comsol Multiphysics software and the appearance of the hot plate geometry is given in Figure C.1.

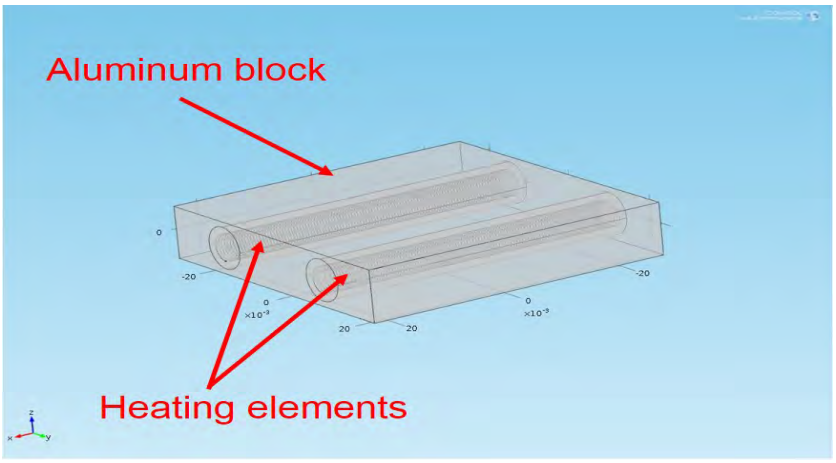

Figure C.1: 3D model of hot plate.

Simulation were made in the *Heat Transfer in Solids* package, where *Convective Cooling* was added. The external temperature was set to be 20 °C (293.15 K), representing room temperature. The heat transfer coefficient was set to 25 W/m^2K. The results of simulations for 150 °C and 300 °C are given in Figures C.2 - C.9, respectively.

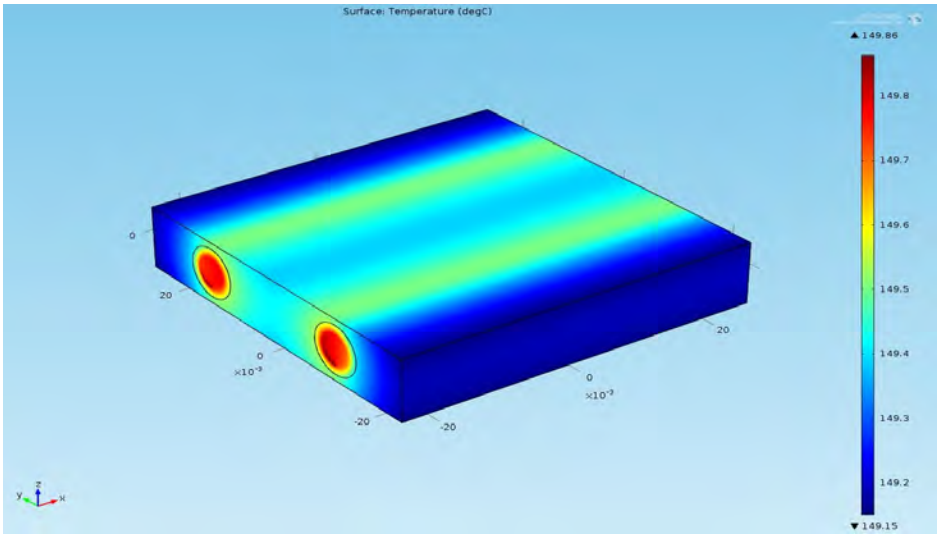

Figure C.2: Simulation results for the hot plate at 150 °C, surface 3D view.

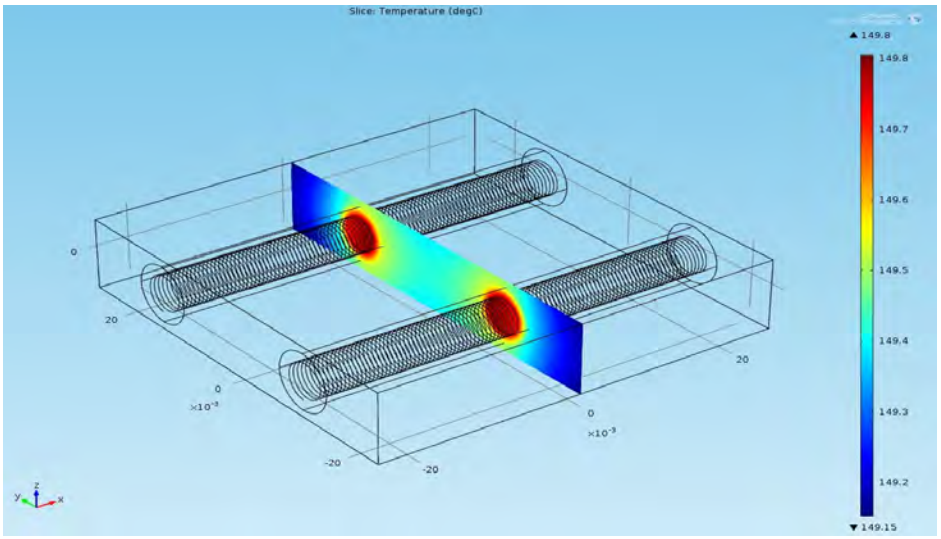

Figure C.3: Simulation results for the hot plate at 150 °C, 3D sliced view.

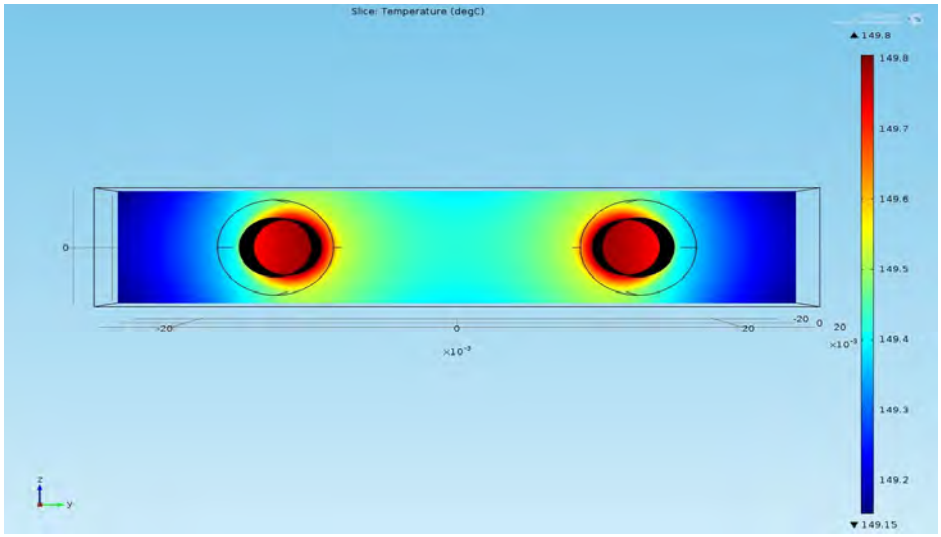

Figure C.4: Simulation results for the hot plate at 150 °C, front sliced view.

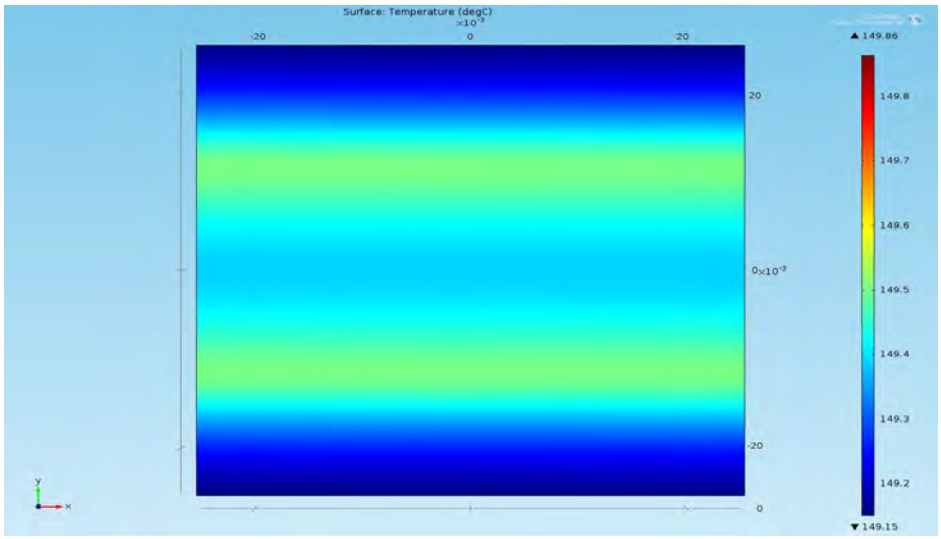

Figure C.5: Simulation results for the hot plate at 150 °C, top view.

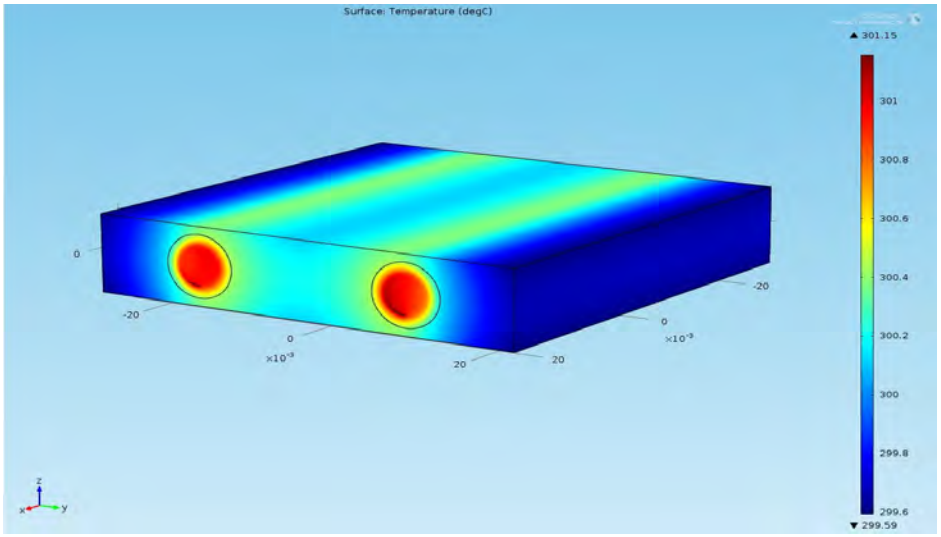

Figure C.6: Simulation results for the hot plate at 300 °C, surface 3D view.

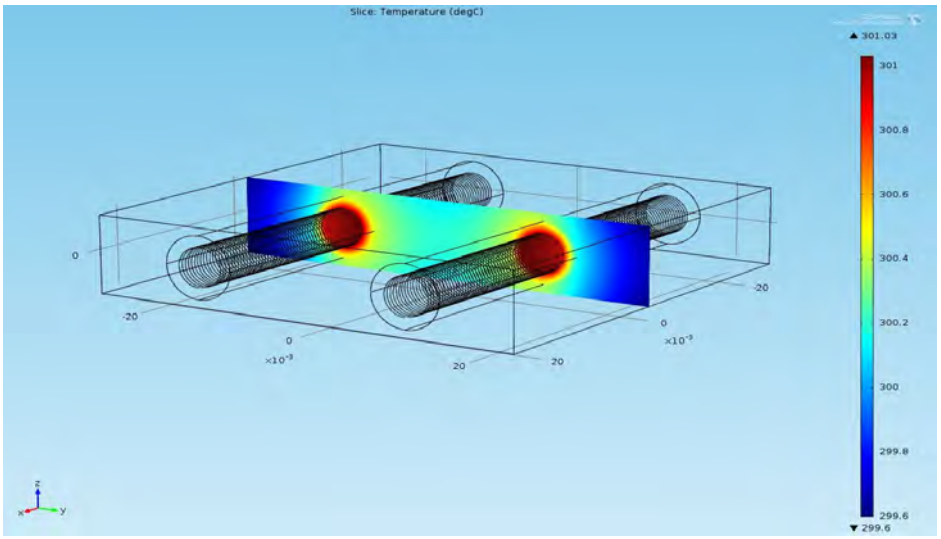

Figure C.7: Simulation results for the hot plate at 300 °C, 3D sliced view.

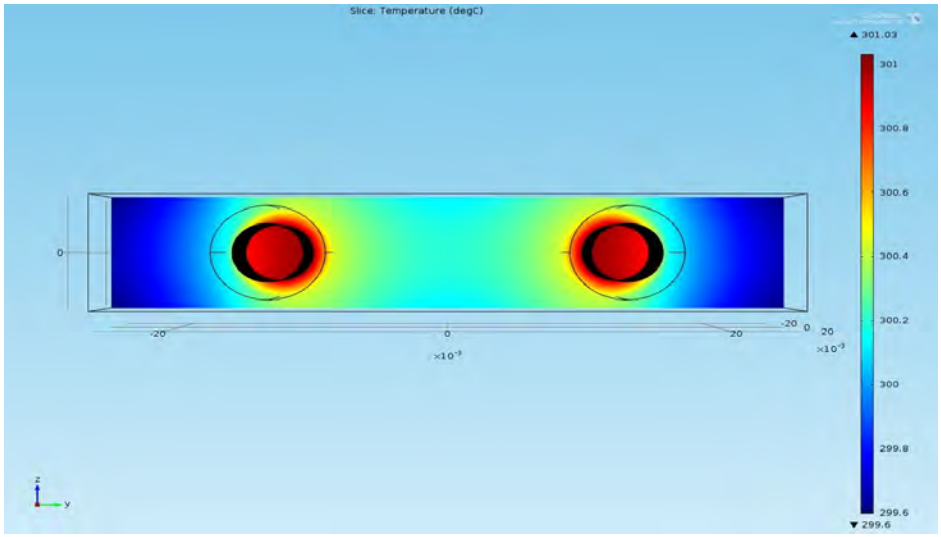

Figure C.8: Simulation results for the hot plate at 300 °C, front sliced view.

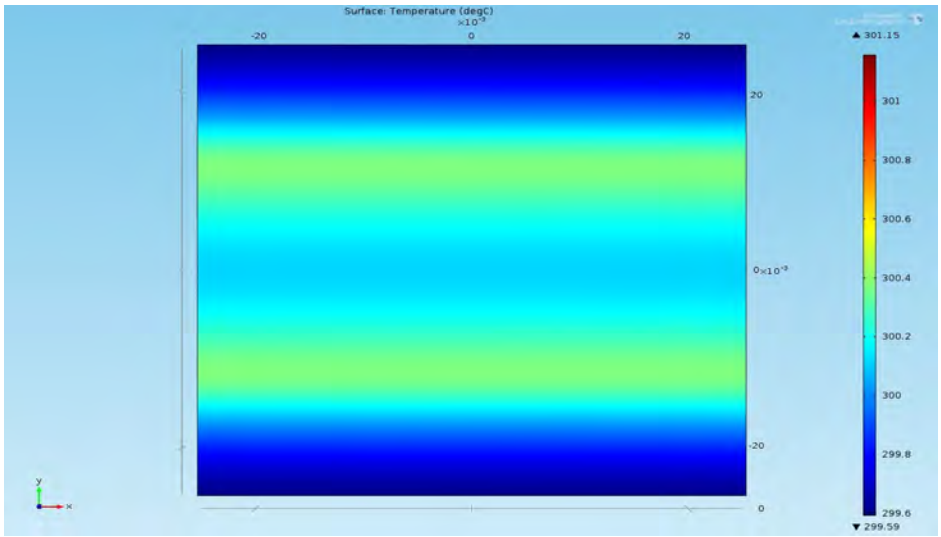

Figure C.9: Simulation results for the hot plate at 300 °C, top view.

Appendix D

List of Publications

D.1 Journals

1. Goran Miskovic, Saša Toškov, Andrea Marić, Nelu Blaž and Goran Radosavljević. Characterization of LTCC Tapes in Water Presence, *Advanced Materials Research*, 2013, vol. 685, pp. 307-311, ISBN 1022-6680.

2. S. Toskov, A. Maric, N. Blaz, G. Miskovic and G. Radosavljevic. *Properties of LTCC Dielectric Tape in High Temperature and Water Environment. International Journal of Materials, Mechanics and Manufacturing*, Vol. 1, No. 4, 2013, pp. 332-336, ISSN: 1793-8198.

3. Nelu Blaž , Goran Mišković , Andrea Marić, Mirjana Damnjanović, Goran Radosavljević and Ljiljana Živanov. *Various Designs of Meander Inductor and Their Influence on LC Resonant Displacement Sensor. Key Engineering Materials*, 2013, vol. 543, pp. 235-238, doi:10.4028/www.scientific.net/KEM.543.235.

4. Nelu Blaž, Goran Mišković, Andrea Marić, Mirjana Damnjanović, Goran Radosavljević and Ljiljana Živanov. *LC Resonant Displacement Sensor Realized with Various Designs of Meander Inductor.Sensor Letters*, 2013, vol. 11, pp. 1-6, doi:10.1166/sl.2013.2935.

5. Jochen Bardong, Alfred Binder, Sasa Toskov, Goran Miskovic, and Goran Radosavljevic. Investigation of low-temperature cofired ceramics packages for high-temperature SAW sensors. *Journal of Sensors and Sensor Systems*, 2015, pp. 85-93, DOI: 10.5194/jsss-5-85-2016.

6. Goran Miskovic, Obrad S Aleksic, Maria V Nikolic, Johann Nicolics, Goran Radosavljevic, Zorka Z Vasiljevic, Miloljub D Lukovic , Walter Smetana. Nanostructured SnO_2 thick films for gas sensor application: analysis of structural and electronic properties. *IOP Conference Series: Materials Sci-*

ence and Engineering, 2016, vol. 108, number 1, http://stacks.iop.org/1757-899X/108/i=1/a=012003.

7. Goran Miskovic and Goran Radosavljevic. Grain size dependence of tin oxide nano paste on sintering temperature. *International Journal of Nanotechnology*, 2015 (in press).

D.2 Conference papers

1. Nelu Blaž , Goran Mišković , Andrea Marić, Mirjana Damnjanović, Goran Radosavljević and Ljiljana Živanov. Modeling and Characterization of LC Displacement Sensor in PCB Technology. *35th International Spring Seminar on Electronics Technology*, 2012, pp. 394-398, ISSN 2161-2528, ISBN: 978-1-4673-2241-6.

2. Andrea Marić, Nelu Blaž, Saša Toškov, Goran Mišković, Ljiljana Živanov and Goran Radosavljević. Implementation of LTCC Interdigital Capacitor for Detection of Liquid Quantity and Type. *48th International Conference on Microelectronics, Devices and Materials – MIDEM*, 2012, pp. 279-284, ISBN 978-961-92933-2-4.

3. S. Toskov, G. Miskovic, A. Maric, N. Blaz and G. Radosavljevic. The Effect of Water Presence on Properties of LTCC Dielectric Tapes. *48th International Conference on Microelectronics, Devices and Materials – MIDEM*, 2012, pp.285-290, ISBN 978-961-92933-2-4.

4. Goran Mišković, Saša Toškov, Andrea Marić, Nelu Blaž and Goran Radosavljević. Behavior of Heraeus CT 703 Tape in Water Environment. *7th International Conference and Exposition on Electrical and Power Engineering*, 2012, pp. 137-140, ISBN: 978-1-4373-5001-3.

5. Goran Mišković, Saša Toškov, Andrea Marić, Nelu Blaž and Goran Radosavljević. Characterization of Dielectric LTCC Tapes. *36th International Spring Seminar on Electronics Technology*, 2013, pp. 189-194, ISBN 978-1-4799-0036-7.

6. Sasa Toskov, Ronald Glatz, Goran Miskovic, Goran Radosavljevic. Modeling and Fabrication of Pt Micro-Heaters Built on Alumina Substrate. *36th International Spring Seminar on Electronics Technology*, 2013, pp. 47-52, ISBN 978-1-4799-0036-7.

7. Goran Miskovic, Michael Unger, Heinz Homolka, Goran Radosavljevic. *Physical and mechanical characterization of LTCC dielectric tapes. 10th International Conference on the Science of Hard Materials*, 2014, pp. 199-200.

8. Goran Miskovic, Javier Fernandez, Heinz Homolka, Michael Unger, Luka Vuckovic, Goran Radosavljevic. Investigation on physical and electrical behaviour of LTCC dielectric tapes. *37th International Spring Seminar on Electronics Technology*, 2014, pp. 237-242, DOI: 10.1109/ISSE.2014.6887600.

9. Nelu Blaž, Andrea Marić, Saša Toškov, Goran Mišković, Goran Radosavljević and Ljiljana Živanov. Capacitive Sensor for Quantity Detection of Known Liquid Present in Distilled Water. *37th International Spring Seminar on Electronics Technology*, 2014, pp. 438-441, DOI: 10.1109/ISSE.2014.6887640.

10. Goran Miskovic, Marko Hrovat, Silvo Drnovsek, Maria Vesna Nikolic; Obrad S. Aleksic; Goran Radosavljevic. Grain size and porosity dependence of titanium dioxide nano-paste on sintering temperature for gas sensing application. *137th International Spring Seminar on Electronics Technology*, 2015, pp. 402-407, DOI:10.1109/ISSE.2015.7248030.

11. Goran Miskovic, Miloljub D Lukovic, Maria Vesna Nikolic, Zorka Z. Vasiljevic, Johann Nicolics and Obrad S. Aleksic. Analysis of electronic properties of pseudobrookite thick films with possible application for NO gas sensing. *39th International Spring Seminar on Electronics Technology*, 2016. (in printing)

Bibliography

[1] J.Y. Kim, S.W. Kang, T.Z. Shin, M.K. Yang, and K.S. Lee. Design of a smart gas sensor system for room air cleaner of automobile thick film metal oxide semiconductor gas sensor. pages 72–75, Oct 2006.

[2] Sofian M. Kanan, Oussama M. El-Kadri, Imad A. Abu-Yousef, and Marsha C. Kanan. Semiconducting metal oxide based sensors for selective gas pollutant detection. *Sensors*, 9(10):8158–8196, 2009.

[3] E. Courtin, G. Baldinozzi, M. T. Sougrati, L. Stievano, C. Sanchez, and C. Laberty-Robert. New Fe_2TiO_5 based nanoheterostructured mesoporous photoanodes with improved visible light photoresponses. *J. Mater. Chem. A*, 2:6567–6577, 2014.

[4] D. S. Ginley and M. A. Butler. The photoelectrolysis of water using iron titanate anodes. *Journal of Applied Physics*, 48(5):2019–2021, 1977.

[5] John H. Seinfeld and Spyros N. Pandis. Atmospheric chemistry and physics: From air pollution to climate change, 2006.

[6] Klea Katsouyanni. Ambient air pollution and health. *British Medical Bulletin*, 68(1):143–156, 2003.

[7] Marilena Kampa and Elias Castanas. Human health effects of air pollution. *Environmental Pollution*, 151(2):362 – 367, 2008.

[8] James A. Raub, Monique Mathieu-Nolf, Neil B. Hampson, and Stephen R. Thom. Carbon monoxide poisoning — a public health perspective. *Toxicology*, 145(1):1 – 14, 2000.

[9] Künzli N. and Tager IB. Air pollution: from lung to heart. *Swiss Medical Weekly*, pages 697–702, 2005.

[10] K Katsouyanni, G Touloumi, C Spix, J Schwartz, F Balducci, S Medina, G Rossi, B Wojtyniak, J Sunyer, L Bacharova, J P Schouten, A Ponka, and H R Anderson. Short term effects of ambient sulphur dioxide and particulate matter on mortality in 12 european cities: results from time series data from the aphea project. *BMJ*, 314(7095):1658, 1997.

[11] Bert Brunekreef and Stephen T Holgate. Air pollution and health. volume 360, pages 1233 – 1242, 2002.

[12] Jonathan A. Bernstein, Neil Alexis, Charles Barnes, I. Leonard Bernstein, Andre Nel, David Peden, David Diaz-Sanchez, Susan M. Tarlo, P. Brock Williams, and Jonathan A. Bernstein. Health effects of air pollution. *Journal of Allergy and Clinical Immunology*, 114(5):1116 – 1123, 2004.

[13] David G. Badman and Ernst R. Jaffe. Blood and air pollution: State of knowledge and research needs. *Otolaryngology - Head and Neck Surgery*, 114(2):205 – 208, 1996.

[14] Paul J. Villeneuve, Michael Jerrett, Darren Brenner, Jason Su, Hong Chen, and John R. McLaughlin. A case-control study of long-term exposure to ambient volatile organic compounds and lung cancer in Toronto, Ontario, Canada. *American Journal of Epidemiology*, 2013.

[15] H Guo, S.C Lee, L.Y Chan, and W.M Li. Risk assessment of exposure to volatile organic compounds in different indoor environments. *Environmental Research*, 94(1):57 – 66, 2004.

[16] Søren K. Kjærgaard, Lars Mølhave, and Ole F. Pedersen. Human reactions to a mixture of indoor air volatile organic compounds. *Atmospheric Environment. Part A. General Topics*, 25(8):1417 – 1426, 1991.

[17] George P. Pappas, Rhonda J. Herbert, William Henderson, Jane Koenig, Bert Stover, and Scott Barnhart. The respiratory effects of volatile organic compounds. *International Journal of Occupational and Environmental Health*, 6(1):1–8, 2000.

[18] Lars Mølhave. Volatile organic compounds, indoor air quality and health. *International Journal of Indoor Environment and Health*, 1(4):357–376, 1991.

[19] Ulrich Pöschl. Atmospheric aerosols: Composition, transformation, climate and health effects. *Angewandte Chemie International Edition*, 44(46):7520–7540, 2005.

[20] J. Vermylen, A. Nemmar, B. Nemery, and M. F. Hoylaerts. Ambient air pollution and acute myocardial infarction. *Journal of Thrombosis and Haemostasis*, 3(9):1955–1961, 2005.

[21] Robert D. Brook, Sanjay Rajagopalan, C. Arden Pope, Jeffrey R. Brook, Aruni Bhatnagar, Ana V. Diez-Roux, Fernando Holguin, Yuling Hong, Russell V. Luepker, Murray A. Mittleman, Annette Peters, David Siscovick, Sidney C. Smith, Laurie Whitsel, and Joel D. Kaufman. Particulate matter air pollution and cardiovascular disease: An update to the scientific statement from the american heart association. *Circulation*, 121(21):2331–2378, 2010.

[22] Mark Sutton, Stefan Reis, and Samantha Baker. *Atmospheric Ammonia: Detecting emission changes and environmental impacts.* Springer, 2009.

[23] Miklós Görgényi, Jo Dewulf, Herman Van Langenhove, and Zoltán Király. Solubility of volatile organic compounds in aqueous ammonia solution. *Chemosphere*, 59(8):1083 – 1090, 2005.

[24] V.R. Phillips, D.S. Lee, R. Scholtens, J.A. Garland, and R.W. Sneath. Se—structures and environment: A review of methods for measuring emission rates of ammonia from livestock buildings and slurry or manure stores, part 2: monitoring flux rates, concentrations and airflow rates. *Journal of Agricultural Engineering Research*, 78(1):1 – 14, 2001.

[25] William Battye, Viney P. Aneja, and Paul A. Roelle. Evaluation and improvement of ammonia emissions inventories. *Atmospheric Environment*, 37:3873–3883, 2003.

[26] John Pearson and George R. Stewart. The deposition of atmospheric ammonia and its effects on plants. *New Phytologist*, 125(2):283–305, 1993.

[27] Willem A. H. Asman, Mark A. Sutton, and Jan K. Schjørring. Ammonia: emission, atmospheric transport and deposition. *New Phytologist*, 139(1):27–48, 1998.

[28] R. E. Critoph. The use of thermosyphon heat pipes to improve the performance of a carbon-ammonia adsorption refrigerator. *International Journal of Environmentally Conscious Design & Manufacturing*, 9(3), 2000.

[29] Agency for Toxic Substances and Disease Registry (ATSDR). Public health statement ammonia. 2004.

[30] S.V Krupa. Effects of atmospheric ammonia NH_3 on terrestrial vegetation: a review. *Environmental Pollution*, 124(2):179 – 221, 2003.

[31] Ryer-Powdera and Jill E. Health effects of ammonia. *Plant/Operations Progress*, 10(4):228–232, 1991.

[32] Pyatt FB. Potential effects on human health of an ammonia rich atmospheric environment in an archaeologically important cave in southeast asia. *Occupational and Environmental Medicine*, pages 986–988, 2003.

[33] L.J.M. van der Eerden. Toxicity of ammonia to plants. *Agriculture and Environment*, 7(3–4):223 – 235, 1982.

[34] Søren O. Petersen, Sven G. Sommer, Ole Aaes, and Karen Søegaard. Ammonia losses from urine and dung of grazing cattle: effect of N intake. *Atmospheric Environment*, 32(3):295 – 300, 1998.

[35] Frank Wania and Donald MacKay. Peer reviewed: Tracking the distribution of persistent organic pollutants. *Environmental Science & Technology*, 30(9):390A–396A, 1996.

[36] K.C. Jones and P. de Voogt. Persistent organic pollutants POPs: state of the science. *Environmental Pollution*, 100(1–3):209 – 221, 1999.

[37] Suzanah Rabodonirina, Sopheak Net, Baghdad Ouddane, Dima Merhaby, David Dumoulin, Tudor Popescu, and Pierre Ravelonandro. Distribution of persistent organic pollutants (PAHs, Me-PAHs, PCBs) in dissolved, particulate and sedimentary phases in freshwater systems. *Environmental Pollution*, 206:38 – 48, 2015.

[38] SL. Ritter, K.R. Solomon, J. Forget, M. Stemeroff, and C.O'Leary. An assessment report on: DDT-aldrin-dieldrin-endrin-chlordane heptachlor-hexachlorobenzene mirex-toxaphene polychlorinated biphenyls dioxins and furans. 1995.

[39] Persistant organic pollutants POPs, children's health and the environment who training package for the health sector world health organization. 2008.

[40] Lavrent Khachatryan, Eric Vejerano, Slawo Lomnicki, and Barry Dellinger. Environmentally persistent free radicals EPFRs. 1. generation of reactive oxygen species in aqueous solutions. *Environmental Science & Technology*, 45(19):8559–8566, 2011. PMID: 21823585.

[41] Shrilatha Balakrishna, Slawo Lomnicki, Kevin M McAvey, Richard B Cole, Barry Dellinger, and Stephania A Cormier. Environmentally persistent free radicals amplify ultrafine particle mediated cellular oxidative stress and cytotoxicity. 2009.

[42] Hannu Komulainen Hyunok Choi, Roy Harrison and Juana M. Delgado Saborit. Who guidelines for indoor air quality: Selected pollutants. `http://www.ncbi.nlm.nih.gov/books/NBK138709/`.

[43] Torben Nielsen, Hans E. Jørgensen, John Chr. Larsen, and Morten Poulsen. City air pollution of polycyclic aromatic hydrocarbons and other mutagens: occurrence, sources and health effects. *Science of The Total Environment*, 189–190:41 – 49, 1996. Highway and Urban Pollution.

[44] World heath organisation. `http://www.who.int/topics/environmental_pollution/en/`.

[45] Directive 2008/50/ec of the european parliament and of the council of 21 may 2008 on ambient air quality and cleaner air for europe. `http://eur-lex.europa.eu/legal-content/EN/TXT/?uri=CELEX:32008L0050/`.

[46] Air quality standards. `http://ec.europa.eu/environment/air/quality/standards.htm`.

[47] National ambient air quality standards NAAQS. `http://www3.epa.gov/ttn/naaqs/`.

[48] National ambient air quality standards NAAQS. `http://www3.epa.gov/ttn/naaqs/criteria.html`.

[49] Ghenadii Korotcenkov. *Handbook of Gas Sensor Materials, Properties, Advantages and Shortcomings for Applications Volume 1: Conventional Approaches*.

[50] Chengxiang Wang, Longwei Yin, Luyuan Zhang, Dong Xiang, and Rui Gao. Metal oxide gas sensors: Sensitivity and influencing factors. *Sensors*, 10(3):2088, 2010.

[51] Hakim Baha and Zohir Dibi. A novel neural network-based technique for smart gas sensors operating in a dynamic environment. *Sensors*, 9(11):8944–8960, 2009.

[52] G. Korotcenkov. Metal oxides for solid-state gas sensors: What determines our choice? *Materials Science and Engineering: B*, 139(1):1 – 23, 2007.

[53] Xiao Liu, Sitian Cheng, Hong Liu, Sha Hu, Daqiang Zhang, and Huansheng Ning. A survey on gas sensing technology. *Sensors*, 12(7):9635–9665, 2012.

[54] V.E. Henrich and P.A. Cox. *The Surface Science of Metal Oxides*. Cambridge University Press, Cambridge, 1996.

[55] Antonio Tricoli, Marco Righettoni, and Alexandra Teleki. Semiconductor gas sensors: Dry synthesis and application. *Angewandte Chemie International Edition*, 49(42):7632–7659, 2010.

[56] Nicolae Barsan and Udo Weimar. Conduction model of metal oxide gas sensors. *Journal of Electroceramics*, 7:143–167, 2001.

[57] M.A. Ponce, M.A. Ramirez, F. Schipani, E. Joanni, J.P. Tomba, and M.S. Castro. Electrical behavior analysis of n-type $CaCu_3Ti_4O_{12}$ thick films exposed to different atmospheres. *Journal of the European Ceramic Society*, 35(1):153 – 161, 2015.

[58] Masaaki Kanamori, Kiyohiro Suzuki, Yutaka Ohya, and Yasutaka Takahashi. Analysis of the change in the carrier concentration of SnO_2 thin film gas sensor. *Japanese Journal of Applied Physics*, 33(12R):6680, 1994.

[59] A. Giberti, M. C. Carotta, C. Malagù, C. M. Aldao, M. S. Castro, M. A. Ponce, and R. Parra. Permittivity measurements in nanostructured TiO_2 gas sensors. *physica status solidi (a)*, 208(1):118–122, 2011.

[60] Hyo-Joong Kim and Jong-Heun Lee. Highly sensitive and selective gas sensors using p-type oxide semiconductors: Overview. *Sensors and Actuators B: Chemical*, 192:607 – 627, 2014.

[61] N. Barsan, D. Koziej, and U. Weimar. Metal oxide-based gas sensor research: How to? *Sensors and Actuators B: Chemical*, 121(1):18 – 35, 2007. Special Issue: 25th Anniversary of Sensors and Actuators B: Chemical.

[62] C. Hagleitner, D. Lange, A. Hierlemann, O. Brand, and H. Baltes. CMOS single-chip gas detection system comprising capacitive, calorimetric and mass-sensitive microsensors. *Solid-State Circuits, IEEE Journal of*, 37(12):1867–1878, Dec 2002.

[63] Hua Bai and Gaoquan Shi. Gas sensors based on conducting polymers. *Sensors*, 7:267–307, 2007.

[64] Sari Lakkis, Rafic Younes, Yasser Alayli, and Mohamad Sawan. Review of recent trends in gas sensing technologies and their miniaturization potential. *Sensor Review*, 34(1):24–35, 2014.

[65] Elisabetta Comini, Guido Faglia, and Giorgio Sberveglieri. Springer-Verlag New York.

[66] Jane Hodgkinson and Ralph P Tatam. Optical gas sensing: a review. *Measurement Science and Technology*, 24(1):012004, 2013.

[67] Ghenadii Korotcenkov. *Handbook of Gas Sensor Materials, Properties, Advantages and Shortcomings for Applications Volume 2: Shortcomings for Applications*.

[68] Ashish Modi, Nikhil Koratkar, Eric Lass, Bingqing Wei, and Pulickel M. Ajayan. Miniaturized gas ionization sensors using carbon nanotubes. *Nature*, 424:171–174, 2003.

[69] G. Dai. A study of the sensing properties of thin film sensor to trimethylamine. *Sensors and Actuators, B: Chemical*, 53(1-2):8–12, 1998.

[70] O.K. Tan, W. Cao, Y. Hu, and W. Zhu. Nano-structured oxide semiconductor materials for gas-sensing applications. *Ceramics International*, 30(7):1127–1133, 2004.

[71] M.R. Mohammadi and D.J. Fray. Low temperature nanocrystalline TiO_2–Fe_2O_3 mixed oxide by a particulate sol–gel route: Physical and sensing characteristics. *Physica E: Low-dimensional Systems and Nanostructures*, 46:43 – 51, 2012.

[72] W Q Guo, S Malus, D H Ryan, and Z Altounian. Crystal structure and cation distributions in the $FeTi_2O_5$-Fe_2TiO_5 solid solution series. *Journal of Physics: Condensed Matter*, 11(33):6337, 1999.

[73] Michele Dondi, Francesco Matteucci, Giuseppe Cruciani, Giorgio Gasparotto, and David M. Tobaldi. Pseudobrookite ceramic pigments: Crystal structural, optical and technological properties. *Solid State Sciences*, 9(5):362 – 369, 2007.

[74] Lei Jin and Chungen Zhou. Electronic structures and optic properties of Fe_2TiO_5 using LSDA+U approach. *Progress in Natural Science: Materials International*, 23(4):413 – 419, 2013.

[75] J.K. Srivastava, J. Hammann, K. Asai, and K. Katsumata. Magnetic hysteresis behaviour of anisotropic spin glass Fe_2TiO_5. *Physics Letters A*, 149(9):485 – 487, 1990.

[76] M. Drofenik, L. Golič, D. Hanžel, V. Kraševec, A. Prodan, M. Bakker, and D. Kolar. A new monoclinic phase in the Fe_2O_3-TiO_2 system. I. structure determination and mössbauer spectroscopy. *Journal of Solid State Chemistry*, 40(1):47 – 51, 1981.

[77] V. Kraševec, A. Prodan, M. Bakker, M. Drofenik, L. Golič, D. Hanžel, and D. Kolar. A new monoclinic phase in the Fe_2O_3-TiO_2 system. II. the defect structure. *Journal of Solid State Chemistry*, 40(1):52 – 58, 1981.

[78] D. Hanžel, M. Drofenik, V. Kraševec, A. Prodan, and F. Sevšek. Mössbauer effect study of monoclinic Fe_2TiO_5. *Solid State Communications*, 40(10):899 – 901, 1981.

[79] D. Hanžel and F. Sevšek. Characterization of monoclinic Fe_2TiO_5 by mössbauer spectroscopy and magnetic susceptibility. *Materials Research Bulletin*, 19(1):35 – 39, 1984.

[80] F. C. Gennari, J. J. Andrade Gamboa, and D. M. Pasquevich. Formation of pseudobrookite through gaseous chlorides and by solid-state reaction. *Journal of Materials Science*, 33(6):1563–1569, 1998.

[81] Dorian A. H. Hanaor and Charles C. Sorrell. Review of the anatase to rutile phase transformation. *Journal of Materials Science*, 46(4):855–874, 2011.

[82] F. C. Gennari and D. M. Pasquevich. Kinetics of the anatase–rutile transformation in TiO_2 in the presence of Fe_2O_3. *Journal of Materials Science*, 33(6):1571–1578, 1998.

[83] A.C. Larson and R.B.Von Dreele. General structure analysis system GSAS (los alamos national laboratory report LAUR86-748), 2004.

[84] Brian H. Toby. *EXPGUI*, a graphical user interface for *gsas*. *Journal of Applied Crystallography*, 34(2):210–213, Apr 2001.

[85] P. Tiedemann and Hk. Müller-Buschbaum. Zum problem der metallverteilung in pseudobrookiten: $FeAlTiO_5$ und Fe_2TiO_5. *Zeitschrift für anorganische und allgemeine Chemie*, 494(1):98–102, 1982.

[86] Hiromitsu Kozuka and Masahiro Kajimura. Sol-gel preparation and photoelectrochemical properties of Fe_2TiO_5 thin films. *Journal of Sol-Gel Science and Technology*, 22(1):125–132, 2001.

[87] K Madhusudan Reddy, Sunkara V Manorama, and A Ramachandra Reddy. Bandgap studies on anatase titanium dioxide nanoparticles. *Materials Chemistry and Physics*, 78(1):239 – 245, 2003.

[88] Dorota Flak, Artur Braun, Antje Vollmer, and Mieczyslaw Rekas. Effect of the titania substitution on the electronic structure and transport properties of FSS-made Fe_2O_3 nanoparticles for hydrogen sensing. *Sensors and Actuators B: Chemical*, 187:347 – 355, 2013.

[89] Z. Zhang. *Optical Properties And Spectroscopy of Nanomaterials*. World Scientific PublishingCo.Pte.Ltd.,Singapore, 2008.

[90] M. A. Ponce, C. Malagu, M. C. Carotta, G. Martinelli, and C. M. Aldao. Gas indiffusion contribution to impedance in tin oxide thick films. *Journal of Applied Physics*, 104(5), 2008.

[91] M Nadeem M Idrees and M M Hassan. Investigation of conduction and relaxation phenomena in $LaFe_{0.9}Ni_{0.1}O_3$ by impedance spectroscopy. *Journal of Physics D: Applied Physics*, 43(15):155401, 2010.

[92] M.V Nikolic, M.P. Slankamenac, N. Nikolic, D.L. Sekulic, O.S. Aleksic, M. Mitric, T. Ivetic, V.B. Pavlovic, and P.M. Nikolic. Study of dielectric behavior and electrical properties of hematite -Fe_2O_3 doped with Zn. *Science of Sintering*, 44(3):307–321, 2012.

[93] R Martínez, A Kumar, R Palai, J F Scott, and R S Katiyar. Impedance spectroscopy analysis of $Ba_{0.7}Sr_{03}TiO_3/La_{0.7}Sr_{0.3}MnO_3$ heterostructure. *Journal of Physics D: Applied Physics*, 44(10):105302, 2011.

[94] A. S. Bondarenko and G. Ragoisha. Eis spectrum analyser (analysis and simulation of impedance spectra).